TECHNISCHE UNIVERSITÄT MÜNCHEN

TUM School of Natural Sciences, Physics Department

On-Surface Synthesis of Novel Macrocyclic Nanostructures via C–C Coupling Assisted by Coordination Pocket Templates

Doctoral Dissertation

Hongxiang Xu

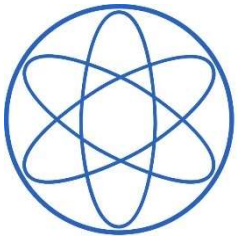

TECHNISCHE UNIVERSITÄT MÜNCHEN

TUM School of Natural Sciences

On-Surface Synthesis of Novel Macrocyclic Nanostructures via C–C Coupling Assisted by Coordination Pocket Templates

Hongxiang Xu

Vollständiger Abdruck der von der TUM School of Natural Sciences der Technischen Universität München zur Erlangung des akademischen Grades eines Doktors der Naturwissenschaften (Dr. rer. nat.) genehmigten Dissertation.

Vorsitz: Prof. Dr. David Egger

Prüfende der Dissertation:

1. Prof. Dr. Johannes Barth
2. Prof. Dr. Mathias Senge

Die Dissertation wurde am 12.03.2024 bei der Technischen Universität München eingereicht und durch die TUM School of Natural Sciences am 15.04.2024 angenommen.

Abstract

On-surface synthesis is emerging as an exceptionally promising research field with the goal of creating atomically well-defined low-dimensional structures and materials. This approach often involves scanning probe microscopy to achieve atomic-level resolution characterization of the fabricated nanostructures. Intermolecular dehydrogenative C–C coupling reaction is an attractive synthetic method, whether in solution or on-surface synthesis, due to its more straightforward and atom-economical nature. However, it presents significant challenges due to the high dissociation energy of C–H bonds and the existence of multiple activation sites. In this thesis, various macrocyclic nanostructures are successfully synthesized through intermolecular dehydrogenation and deoxygenative C–C coupling facilitated by special coordination pocket templates on atomically flat metal surfaces. These synthesized macrocyclic nanostructures are characterized using scanning tunneling microscopy, non-contact atomic force microscopy and X-ray photoelectron spectroscopy.

Specifically, we employ natural dyes (indigo and the related Tyrian purple) as molecular building blocks to fabricate coordination polymers. Both building blocks yield identical, well-defined coordination polymers composed of (1 dehydroindigo : 1 Fe) repeat units on two different silver single crystal surfaces. On Ag(100) and on Ag(111), the *trans* configuration of dehydroindigo results in N,O-chelation in the polymer chains. On the more inert Ag(111) surface, the molecules undergo thermally induced isomerization from the *trans* to the *cis* configuration and afford N,N- plus O,O-chelation.

In a second part, we co-deposit indigo molecule and Fe on Au(111) to obtain a novel Fe-pophryrinoid (**Fe-Por**) species and its extension in fused Fe-porphyrinoid nanotapes (**Fe-Por NTs**). The novel metallated indigo-based **Por** was synthesized with a high yield through a series of thermally activated reaction steps, including isomerization and selective C–H activation assisted by a coordination pocket template. Subsequent deoxygenative and dehydrogenative C–C coupling reactions were employed to fuse these **Fe-Pors**, resulting in the formation of **Fe-Por NTs** (**(Fe-Por)$_2$ NT and (Fe-Por)$_3$ NT**) in which **Por** segments are connected by unprecedented **NT** quadruple linkages to form two fused six- and one eight-membered rings.

Finally, based on the results of the second part, which demonstrated intermolecular high selectivity dehydrogenation C–C coupling facilitated by the coordination pocket template, we have applied this method to additional systems. Specifically, we have employed 1H,1'H-2,2'-Bibenzo[d]imidazole (H_2bbim), a molecule closely resembling indigo but featuring nitrogen atoms in place of carbonyl groups, to successfully synthesize planar π-extended [n]cycloparaphenylenes (n= 24, 26, 27, 28 and 31) and other type cyclic polymers on Au(111) through intermolecular dehydrogenative C–C coupling again facilitated by the coordination pocket template.

Zusammenfassung

Syntheseprotokolle auf katalytisch aktiven Oberflächen mit dem Ziel, atomar wohldefinierte organische Materialien herzustellen haben sich in den letzten Jahren zu einem äußerst vielversprechenden Forschungsgebiet entwickelt. Dieser Ansatz wird häufig mittels Rastersondenmikroskopie verfolgt, um eine Charakterisierung der synthetisierten Nanostrukturen mit atomarer Auflösung zu erreichen. Die intermolekulare dehydrierende C–C-Kupplungsreaktion ist eine äußerst attraktive Synthesemethode sowohl in Lösung als auch auf der Oberfläche, da sie im Vergleich zu anderen klassischen organischen Synthesemethoden einfacher und atomökonomischer ist. Aufgrund der hohen Dissoziationsenergie der C-H-Bindungen und der Existenz mehrerer Aktivierungsstellen stellt dies jedoch erhebliche Herausforderungen dar. In dieser Dissertation wurden verschiedene makrozyklische Nanostrukturen erfolgreich durch intermolekulare Dehydrierung und desoxygenierende C–C-Kopplung synthetisiert, die durch spezielle Metall-Koordinationstaschentemplate auf atomar flachen Metalloberflächen unterstützt werden. Diese synthetisierten makrozyklischen Nanostrukturen wurden mittels Rastertunnelmikroskopie, Rasterkraftmikroskopie und Röntgenphotoelektronenspektroskopie charakterisiert.

Insbesondere wurden natürliche Farbstoffe (Indigo und das verwandte Tyrianpurpur) als molekulare Bausteine zur Herstellung von Koordinationspolymeren verwendet. Beide Bausteine ergeben identische, wohldefinierte Koordinationspolymere, die aus (1 Dehydroindigo : 1 Fe) Wiederholungseinheiten auf zwei unterschiedlichen Silbereinkristalloberflächen bestehen. Auf Ag(100) und auf Ag(111) führt die trans-Konfiguration von Dehydroindigo zu einer N,O-Chelatbildung in den Polymerketten. Auf der inerteren Ag(111)-Oberfläche durchlaufen die Moleküle eine thermisch induzierte Isomerisierung von der trans- zur cis-Konfiguration und führen zu einer N,N- plus O,O-Chelatbildung.

Im zweiten Teil wurden Indigomoleküle und Fe-Atome gemeinsam auf der Au(111)-Oberfläche aufgebracht und wir erhielten ein neuartiges Fe-Pophryrinoid (**Fe-Por**) in Koordinationspolymeren und seine Erweiterung in kondensierten Fe-Porphyrinoid-Nanobändern (**Fe-Por NTs**). Das neuartige metallierte Indigo-basierte **Por** wurde mit hoher Ausbeute durch eine Reihe thermisch aktivierter Reaktionsschritte synthetisiert, einschließlich Isomerisierung und selektiver C–H-Aktivierung, unterstützt durch ein Koordinationstaschentemplat. Nachfolgende desoxygenierende und dehydrierende C–C-Kupplungsreaktionen wurden eingesetzt, um diese Fe-Pors zu verschmelzen. Dies führte zur Bildung von **Fe-Por NTs** (**(Fe-Por)$_2$ NT** und **(Fe-Por)$_3$ NT**), in denen **Por**-Segmente durch **NT**-Vierfachverknüpfungen verbunden sind. Diese Segmente enthalten zwei verschmolzene Sechs- und einen Achtfachring.

Basierend auf den Ergebnissen des zweiten Teils, haben wir diese Methode schließlich auf weitere Systeme angewendet. Konkret haben wir 1H,1'H-2,2'-Bibenzo[d]imidazol (H_2bbim) eingesetzt, ein Molekül, welches Indigo stark ähnelt, aber Stickstoffatome anstelle von Carbonylgruppen aufweist, um erfolgreich planare [n] mit erweitertem π- Electronensystem zu synthetisieren. Mittels Koordinationstaschentemplate konnten Cycloparaphenylene (n= 24, 26, 27, 28 und 31) und andere zyklische Polymere auf Au(111) durch intermolekulare dehydrierende C–C-Kupplung synthetisiert werden.

Contents

Acronyms

UHV	ultrahigh vacuum
GNRs	graphene nanoribbons
VT/LT-STM	variable/ low-temperature scanning tunneling microscopy
JT-STM	Joule-Thomson scanning tunneling microscopy
nc-AFM	non-contact atomic force microscopy
NEXAFS	near-edge X-ray absorption fine structure
ARPES	angle-resolved photoemission spectroscopy
XPS	X-ray photon spectroscopy
DFT	density functional theory
1D	one dimensional
Fe-Pors	Fe-porphyrinoids
Fe-Por NTs	Fe-porphyrinoid nanotapes
H_2bbim	1H,1'H-2,2'-bibenzo[d]imidazole
OMBE	organic molecular beam epitaxy
LN_2	liquid nitrogen
LHe	liquid helium
CPs	coordination polymers
r.t.	room temperature
HOMO	highest occupied molecular orbital
LUMO	lowest unoccupied molecular orbital
dI/dV	differential conductance
[n]CPPs	[n]cycloparaphenylenes

1. Introduction

Controllable construction of nanoarchitectures with atomic precision is an intriguing concept in modern nanotechnology. Nowadays, zero-, one-, or two-dimensional materials, such as quantum dots, nanoribbons or polymers, and nanosheets, respectively, are routinely synthesized in solution or using appropriate top-down methods. However, fabricating molecular electronic or spintronic devices requires a controllable arrangement of interactions between the molecular counterparts in a clean environment, which poses a significant challenge for materials synthesized in solution. Furthermore, top-down methods such as photolithography or plasma treatment face difficulties in constructing atomic-scale structural features. On-surface synthesis,[1-5] one of the most powerful bottom-up methods, presents a promising approach towards overcoming these challenges. It is an emerging research field with great potential for fabricating well-defined covalent nanostructures with atomic precision. In this synthetic approach, pre-designed organic precursor molecules containing functional groups like alkynyl, alkenyl, halogen, etc., are first deposited on a clean and flat surface through sublimation in ultrahigh vacuum (UHV). Subsequently, these molecules undergo chemical reactions and form covalent nanostructures through thermal annealing,[6] single electron reduction,[7-9] or photo-irradiation.[10, 11] Finally, the synthesized nanostructures are usually characterized and analyzed using scanning tunneling microscopy (STM) and non-contact atomic force microscopy (nc-AFM), which provide atomic resolution in real space. Additionally, other advanced surface science techniques, including X-ray photon spectroscopy (XPS) that can identify the chemical state of chemical elements, near-edge X-ray absorption fine structure (NEXAFS) that provides formal valence, coordination environment, and subtle geometrical distortions, and angle-resolved photoemission spectroscopy (ARPES) that provides electronic band structure are employed to study the synthesized nanostructures alongside with STM and nc-AFM.

Numerous classic organic reactions that are traditionally carried out in solution have been successfully adapted in on-surface synthesis, such as Ullmann coupling[12-15], boronic acid condensation,[16-18] Schiff-base reaction,[19-21] Bergman reaction,[22, 23] Glaser coupling,[24-26] intermolecular[27-29] or intramolecular[30-32] dehydrogenation C–C coupling, etc. Notably, Ullmann coupling and intramolecular dehydrogenation C–C coupling (cyclodehydrogenation) are frequently employed for fabricating atomically precise graphene nanoribbons (GNRs).[15, 33, 34] For instance, in 2010, Cai and co-workers first reported the thermal polymerization (Ullmann coupling) and planarization (intramolecular C–C coupling) of a precursor molecule, 10,10′-dibromo-9,9′-bianthryl, leading to the formation of 7-armchair GNRs on the Au(111) surface.[15] Moreover, bond formation by selective C–H activation is an extremely attractive synthetic method, whether in solution[35-37] or on-surface synthesis[27, 38] because this method offers a more straightforward and atom-economical approach compared to other classical organic synthesis strategies, such as aryl-aryl bond formation by transition-metal-catalyzed direct arylation.[39] However, it presents significant challenges due to the high dissociation energy of C–H bonds and the presence of multiple activation sites. To trigger the activation of originally inert C–H bonds, various strategies have been adopted, including transition-metal catalysis,[40-43] photocatalysis,[44-46] harsh conditions,[47] and metal surfaces.[27, 29, 48] Furthermore, addressing the multisite issue, directing groups,[38, 49] and metal templates[50-52] have been employed.

Template synthesis[53-55] is a method that utilizes noncovalent binding motifs, known as template bonds, to guide the formation of covalently linked products that are challenging to obtain in the absence of a template. This approach traces back to the 1960s when Busch first

demonstrated template effects in the synthesis of new compounds.[56] Template bonds encompass various interactions, including metal-ligand binding, hydrogen bonding, and π-π interactions. Among these, metal-directed assembly can provide a template effect to pre-organize the reactants and to control the reaction. An excellent example of such a template was showcased by Anderson and his colleagues, who synthesized belt-like nanorings comprising of 6, 8, 12, or more porphyrin units using radial oligo-pyridine templates.[57] Similar templates also facilitate intermolecular selectivity dehydrogenation C–C coupling. For example, Gill and co-workers successfully synthesized bidipyrrin in solution through a coupling of two α-carbons assisted by bisdipyrrinato Ni(II) complexes template.[50] Furthermore, Liu and co-workers presented an on-surface synthesis of linear heteroaromatic polymers by directly selective C–H activation for dehydrogenative C–C couplings of hexaazatriphenylene molecules under the guidance of a coordination pocket as a directed template.[52]

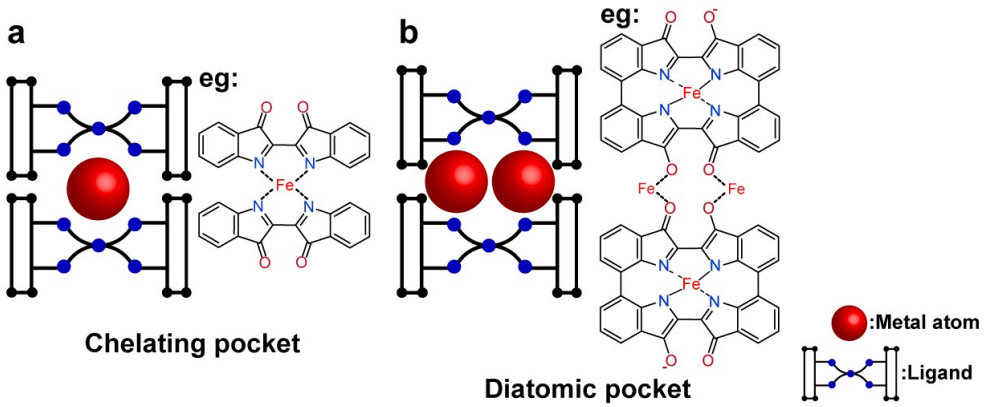

Figure 1.1: A simplified schematic of the coordination pocket template with two examples. (a) One example of coordination pocket: chelating pocket. (b) Another one: diatomic pocket. The blue ball in the ligand means chemical groups that can coordinate with metal atoms. Red ball means metal atom.

In this thesis, we present the introduction of a special coordination pocket template to synthesize novel macrocyclic nanostructures (e.g., porphyrinoids, quadruply fused porphyrinoid nanotapes, and cyclic polymers including planar π-extended cycloparaphenylenes) on surface via intermolecular selective dehydrogenation C–C coupling. We define two types of coordination motifs: chelating pockets (Figure 1.1a) and diatomic pockets (Figure 1.1b). The distinction between these two lies in the presence of multiple metal atoms in the diatomic pocket, as opposed to only one central metal atom in the chelating pocket. The core idea of the method involves synthesizing a polymer with a coordination pocket first. Subsequently, intermolecular dehydrogenative C–C coupling assisted by the pocket template occurs within the pocket region (C–H activation in the *meta* or *ortho*-positions relative to the coordination groups). The pocket template not only provides a suitable spatial orientation for intermolecular dehydrogenation C–C coupling but also likely lowers the energy barrier for C–H activation due to the catalytic effect of the metal center. Ultimately, covalent dimers (where C–H activation occurs on both sides of the ligand, resulting in a ring-closing reaction) or covalent polymers (where C–H activation takes place on only one side of the ligand) are formed (Figure 1.2). Further details regarding the synthesis processes and related motivations will be given in the respective dedicated Chapter. The outline of each Chapter in this thesis is as follows.

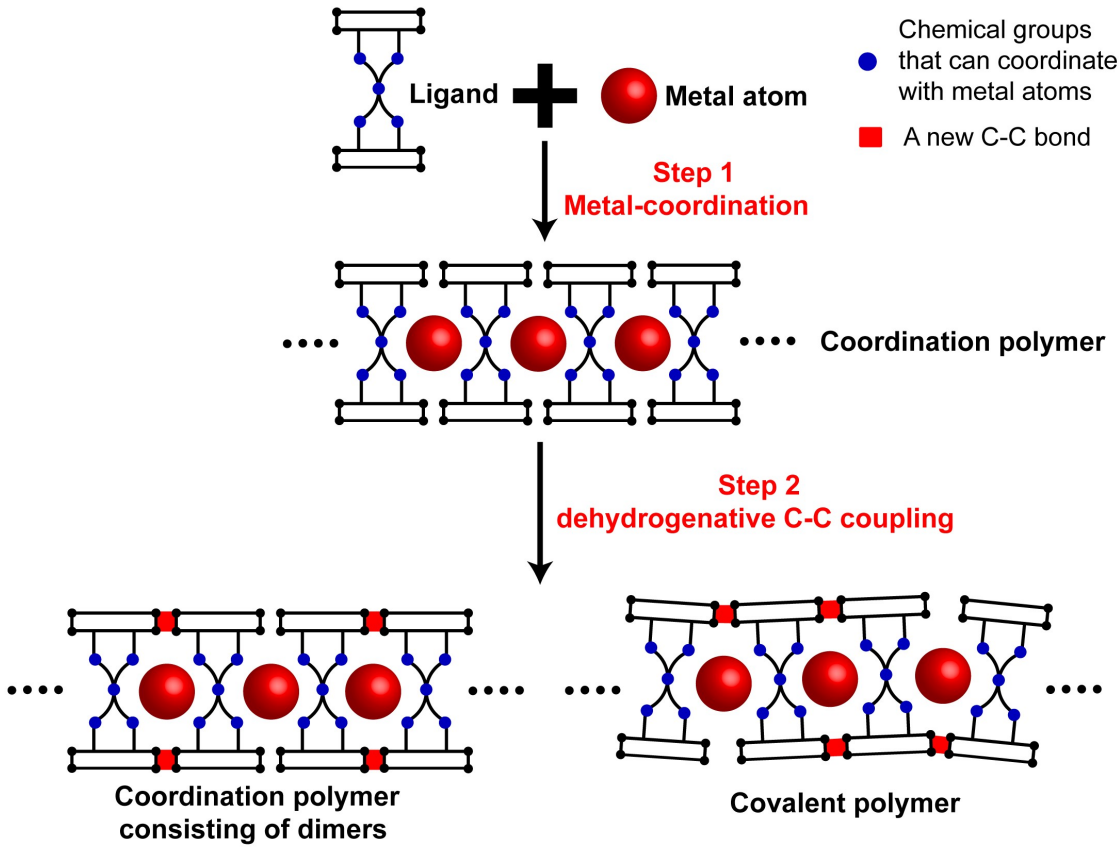

Figure 1.2: A simplified schematic of the process of intermolecular dehydrogenation C–C coupling assisted by coordination pocket templating. The blue ball in the ligand means chemical groups that can coordinate with metal atoms. The orange line represents a new C–C bond formed by dehydrogenative C–C coupling.

Chapter 2 provides an overview of the fundamental principles of the experimental techniques and the methods utilized in this thesis. The surface imaging techniques used in this study include STM and nc-AFM. Additionally, XPS was employed to analyze the chemical state of the elements involved in molecules or nanostructures on surfaces. Furthermore, density functional theory (DFT) was utilized to develop and investigate theoretical models that explain the experimental observations (DFT calculations are performed by our collaborator: Dr. Abhishek, Chakraborty and Prof. Narasimhan). The combination of experimental techniques and theoretical calculations enhances our understanding of the synthesized nanostructures and their properties.

In Chapter 3, we present surface-confined metallosupramolecular engineering of coordination polymers using natural dyes as molecular building blocks: indigo and the related Tyrian purple (6,6′-dibromoindigo). Both building blocks yield identical, well-defined coordination polymers composed of (1 dehydroindigo : 1 Fe) monomers on two different silver single crystal surfaces, Ag(111) and Ag(100). On the Ag(111) surface, two distinct isomeric polymers are identified, resulting from the *trans* and *cis* configurations of dehydroindigo and affording N,O- and N,N- plus O,O-chelation. However, the substrate packing proves to be important in this process: no isomerization was found in the CPs for indigo (or 6,6′-dibromoindigo) with Fe adsorbed on the Ag(100) surface. Our results demonstrate tunable interfacial metal-organic nanosystems through post-synthetic linker isomerization and provide

insights into the experimental results obtained from the same system on Au(111) (presented in Chapter 4).

In Chapter 4, we present the on-surface synthesis of quadruply fused Fe-porphyrinoid nanotapes (**Fe-Por NTs**) made up of novel Fe-porphyrinoids (**Fe-Pors**) using indigo molecules with Fe atoms on Au(111). First, the novel metallated **Pors** (one kind of porphycene derivative) were synthesized with high yield by a series of thermally activated reaction steps including isomerization and selective C–H activation assisted by coordination pocket templating. Then, by further deoxygenative and dehydrogenative C–C coupling, **Fe-Pors** can fuse into **Fe-Por NTs** (**(Fe-Por)$_2$ NT** and **(Fe-Por)$_3$ NT**) in which **Por** segments are connected by quadruple linkages to form two fused six- and one eight-membered ring. Our studies enrich the available chemistry for on-surface and solution synthesis of macrocyclic tetrapyrroles and quadruply fused **Por NTs** and may provide new way for fabrication of novel low-dimensional nanostructures.

In Chapter 5, inspired by intermolecular high selectivity dehydrogenation C–C coupling assisted by the coordination pocket template, we extend this method to more systems. We used 1H,1'H-2,2'-Bibenzo[d]imidazole (H_2bbim): a molecule similar to indigo and which features N atoms in place of the carbonyl groups. From H_2bbim with Fe atoms we obtained cyclic polymers including planar π-extended cycloparaphenylenes on Au(111) as well as another **Fe-Pors**. The **Pors** were synthesized by dehydrogenative C–C coupling of both sides of H_2bbim (illustrated in the bottom left of Figure 1.2). The cyclic polymers were synthesized by dehydrogenative C–C coupling of a single side and/or both sides of H_2bbim (illustrated in the bottom right of Figure 1.2). These results prove that coordination pocket templating is a versatile strategy for the on-surface synthesis of nanostructures.

2. Experimental methods and techniques

This chapter introduces the fundamental principles of the experimental methods and techniques utilized during the presented studies. Scanning tunneling microscopy and non-contact atomic force microscopy were used to characterize the surface-adsorbed molecules and on-surface synthesized nanostructures in real space. X-ray photoelectron spectroscopy was employed to investigate the chemical states of chemical elements in the molecules or nanostructures adsorbed on surfaces.

2.1. Scanning tunneling microscopy

Scanning tunneling microscopy (STM) is a powerful and useful technique that allows people to image surfaces and atoms (or nanostructures) adsorbed on surfaces with high spatial resolution. It was invented by Gerd Binnig and Heinrich Rohrer in 1981 at the IBM Zurich Research Laboratories,[58] for which they shared the Nobel Prize in Physics in 1986. STM images are obtained by scanning the surface with an atomically sharp metallic tip at a very small distance while applying a bias voltage (Figure 2.1). A tunneling current flows between the tip and the sample owing to the effect of quantum tunneling, allowing to obtain the surface's topography and related electronic properties. The tip can be driven by the piezoelectric tube and move in the sub-nanometer regime in lateral directions. In the following section, the fundamentals of STM are described.

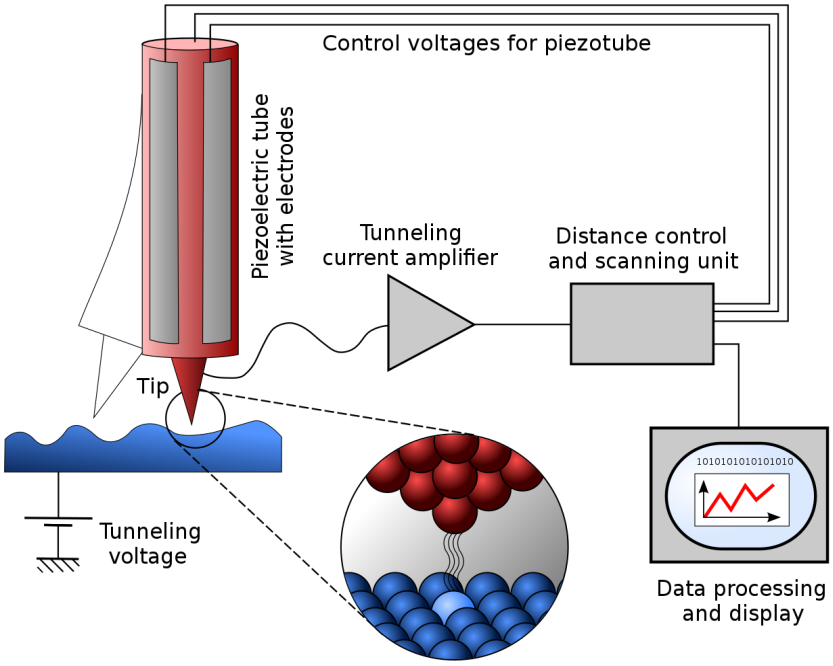

Figure 2.1: A simplified working scheme of an STM. The piezo tube drives a metallic tip to scan above the sample's surface. When the tip is close to the sample, and a bias voltage is applied, a tunneling current flows between the tip and the sample (see inset). (The picture is taken from Wikipedia)

2.1.1. Basic principle of STM

STM is based on the quantum mechanical phenomenon known as tunneling. In classical physics, particles cannot penetrate through a potential barrier with the height V if their energy E is smaller than V. Quantum mechanics, however, allows particles (electrons in the case of the

STM experiment) to penetrate through barriers of finite height with a certain probability, even though the energy of the particles is lower than the potential barrier. Particles such as electrons can behave as waves with a wave function Ψ that can be described by the Schrödinger equation (one-dimensional and time-independent, for simplicity here):

$$-\frac{\hbar^2}{2m}\frac{d^2\Psi}{dz^2} + V(z)\Psi = E\Psi \tag{2.1}$$

where $\hbar$ is the reduced Planck constant and m is the electron mass. Considering a rectangular potential barrier of height V_0 and of width d (Figure 2.2a, region 2), the incoming electron wave propagating in the positive z-direction (Figure 2.2a, region 1), and its energy $E < V_0$, we obtain wave function solutions in different regions:

$$\Psi_{1,3}(z) = \Psi^0_{1,3} e^{\pm ikz}, k = \frac{\sqrt{2mE}}{\hbar} \tag{2.2}$$

$$\Psi_2(z) = \Psi^0_2 e^{-\kappa z}, \kappa = \frac{\sqrt{2m(V_0 - E)}}{\hbar} \tag{2.3}$$

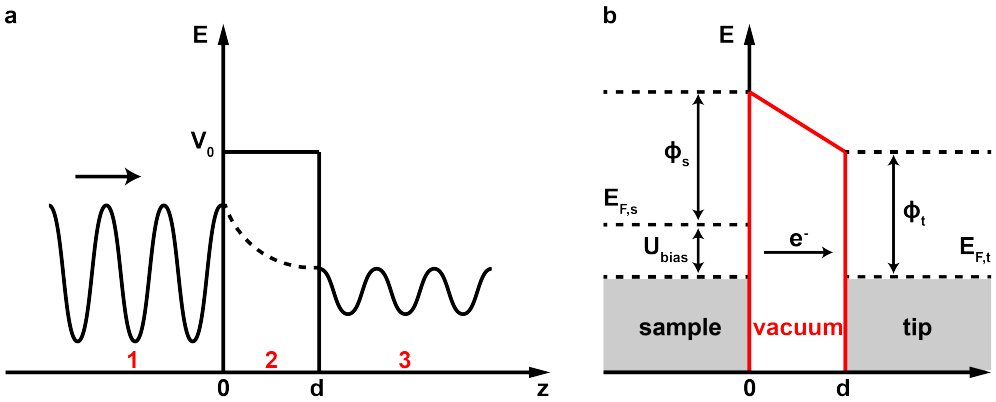

Figure 2.2: Schematic illustration for the quantum tunneling effect and STM tip-sample tunneling. (a) The electron wave function tunnels through a potential barrier V_0 from regions 1 to 3 with exponential decay. (b) The applied bias between tip and sample changes the position of the Fermi-level of the tip or the sample, resulting in a tunneling current.

Based on these equations, the transmission probability of the electron wave through the barrier T can be obtained:

$$T = |\Psi_2(d)|^2 = |\Psi^0_2|^2 \exp\left[\frac{-2d\sqrt{2m(V_0 - E)}}{\hbar}\right] \tag{2.4}$$

It can be seen that T exponentially depends on the barrier width and the energy difference between the potential and the electrons energy. This sensitivity of electron tunneling on the barrier width enables STM to achieve high-resolution imaging.

In the case of STM, electron tunneling happens between the STM tip and the sample, so the potential barrier translates to the vacuum space between them. Furthermore, the distance between the tip and the sample determines the width of the potential barrier. Without an applied bias voltage between the tip and the sample, the Fermi level of the tip and the sample are aligned, resulting in electrons tunneling equally in both directions, leading to a zero net current. However, when a bias voltage U is applied, the Fermi level of the tip and sample will be shifted, resulting in a net flow of tunneling current (Figure 2.2b). In order to describe the tunneling current, Bardeen proposed an approach that expresses the tunneling current produced in a metal-oxide-metal junction using the first-order time-dependent perturbation theory.[59] Later, Hamann

and Tersoff put forward a more elaborated model of the tunneling current in 1985,[60] extending Bardeen's approach. Here, the tunneling current I can be described as:

$$I = \frac{2\pi}{\hbar}\sum_{\mu,\nu} f(E_\mu)[1 - f(E_\nu + e\,U)]\left|M_{\mu\nu}\right|^2 \delta(E_\mu - E_\nu) \tag{2.5}$$

with the Fermi function $f(E)$, the applied bias voltage U, the tunneling matrix element $M_{\mu\nu}$ between state Ψ_μ of the tip and Ψ_ν of the sample, and the energy E_μ, E_ν of state Ψ_μ, Ψ_ν respectively. δ is here a δ-function and ensures that only elastic tunneling processes are taken into account. Considering small voltages and low temperatures, this equation can be further simplified to

$$I = \frac{2\pi}{\hbar} e^2 U \sum_{\mu,\nu}\left|M_{\mu\nu}\right|^2 \delta(E_\mu - E_F)\delta(E_\nu - E_F) \tag{2.6}$$

where E_F is the Fermi level. The matrix element can be given by an integral over the surface states that lie within the energy window between the tip and the sample:

$$M_{\mu\nu} = \frac{\hbar^2}{2m}\int d\vec{S}(\Psi_\mu^*\vec{\nabla}\Psi_\nu - \Psi_\nu\vec{\nabla}\Psi_\mu^*) \tag{2.7}$$

As it is hard to determine the exact shape of the tip, Tersoff and Hamann supposed the tip to be spherical, with a radius of R and the center position of $\vec{r_0}$ (the position of the center of the spherical tip-apex in respect to the surface) (Figure 2.3). By this and assuming the identical work function ϕ of tip and sample, the expression for the tunneling current can be written as:

$$I = \frac{32\pi^3 e^2 U \phi^2 R^2 e^{2\kappa R}}{\hbar\kappa^4} D_t(E_F)\sum_\nu |\Psi_\nu(\vec{r_0})|^2 \delta(E_\nu - E_F) \tag{2.8}$$

with the density of states per unit volume of the tip D_t. At the tip position of $\vec{r_0}$, the local density of state (LDOS) of the surface at E_F is:

$$\rho_\nu(\vec{r_0}, E_F) = \sum_\nu |\Psi_\nu(\vec{r_0})|^2 \delta(E_\nu - E_F) \tag{2.9}$$

The surface wave function in the direction perpendicular to the sample surface is given by:

$$\Psi_\nu(\vec{r_0}) \propto e^{-\kappa z}, z = d + R \tag{2.10}$$

where d is the distance between the tip and the sample. Therefore, the tunneling current exhibits an exponential dependence on the tip-sample distance, as shown in equations 2.8 and 2.10. Additionally, the tunneling current is also proportional to the LDOS (equation 2.9). These show that an STM image cannot be seen as a topography of the sample surface alone but as a convolution of topographic and electronic information, which is also influenced by the shape of the tip.

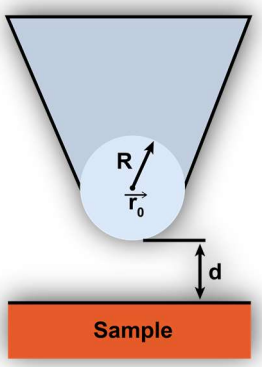

Figure 2.3: Scheme based on the Tersoff-Hamann model. The tip apex is formed by a single atom at position $\overrightarrow{r_0}$ with a spherical potential well of radius *R*. The nearest distance to the sample is *d*.

2.1.2. Scanning tunneling spectroscopy

Scanning tunneling spectroscopy (STS), proposed by Selloni in 1985, is an extension of the imaging capability of STM.[61] STS allows the measurement of local electronic properties of samples (surfaces or nanostructures). A mathematical description of STS was provided, for example, by Hamers. Based on his work (Wentzel-Kramers-Brillouin (WKB) approximation)[62] and assuming that the transition matrix is approximated by an average transmission probability ($M_{\mu\nu} = T(\overrightarrow{r_0}, E, eV)$), the tunneling current in Eq. (2.6) can be rewritten as:

$$I \propto \int_0^{eV} \rho_s(\overrightarrow{r_0}, E)\rho_t(\overrightarrow{r_0}, E - eV)T(\overrightarrow{r_0}, E, eV)dE \tag{2.11}$$

where ρ_t and ρ_s are the LDOS of the tip and the sample, respectively. The differentiation d*I*/d*V* can be given as:

$$\frac{dI}{dV} \propto \rho_s(\overrightarrow{r_0}, eV)\rho_t(\overrightarrow{r_0}, 0)T(\overrightarrow{r_0}, eV) + \int_0^{eV} \rho_s(\overrightarrow{r_0}, E)\rho_t(\overrightarrow{r_0}, E - eV)\frac{dT(\overrightarrow{r_0},E,eV)}{dU}dE \tag{2.12}$$

Assuming that the transmission probability is voltage-independent according to WKB approximation and the tip LDOS is constant, Eq. (2.12) can be further simplified to

$$\frac{dI}{dV} \propto \rho_s(\overrightarrow{r_0}, eV) \tag{2.13}$$

This equation indicates that STS indeed probes the LDOS of the surface, so the local electronic structure of the sample can be acquired by measuring the differential conductance *dI/dV*.

One method to get the differential conductance or *dI/dV* signal is to derive the *I(V)* curve numerically. However, this is not the preferred method since the measured signal includes noise, which would be amplified by taking the derivative. A better method is the lock-in technique. This technique is based on superimposing a small and high frequency modulation voltage onto the applied sample bias, while this bias is varied in the desired range. The modulation frequency used in STS must be higher than the frequency of the STM feedback system because otherwise, the feedback loop may try to compensate for the bias modulation, resulting in distorted STS measurements. The STM feedback loop can monitor the tunneling current and coordinate the current and the positioning of the tip. The alternating component of the current signal is recorded via a lock-in amplifier, and the component with the right frequency and the correct phase directly gives the *dI/dV* signal and, therewith the LDOS of the sample.

2.1.3. Operational modes of an STM

There are two different operation models to scan samples: the constant height and constant current mode, as shown in Figure 2.4. In constant height mode, the tip does not change its height during scanning the surface laterally while the tunnel current is recorded. Thus, the obtained image gives information about the topography of the sample and the local density of electronic states. However, this mode is rarely used for large-scale and rough surface imaging due to the risk of crashing the tip into the sample. In constant current mode, the more frequently used mode, a feedback loop controls the tip-sample distance in order to keep the tunneling current constant while the z-displacement is recorded. Therefore, the corresponding obtained STM images show the surface topography.

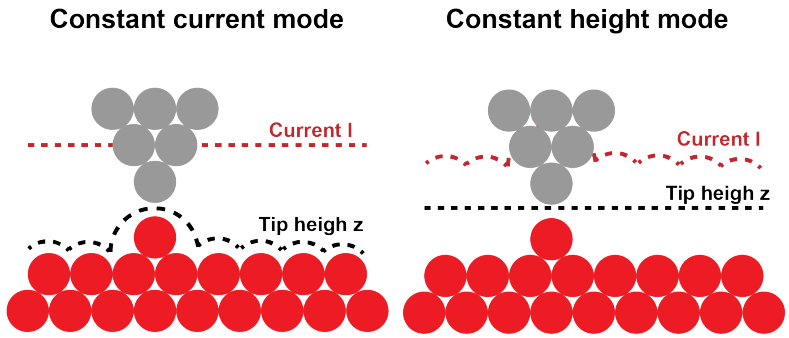

Figure 2.4: Schematic illustration of the operational modes of an STM.

2.2. Atomic force microscopy

Atomic force microscopy (AFM) was invented by Binnig and his colleagues in 1986.[63] Unlike the STM, it measures the forces between the probe tip and the sample instead of the tunnel current, so it enables atomic-precision real-space resolution for insulating samples on which STM cannot be operated. The following introduces the fundamental working principles of the AFM and of the so-called qPlus sensor.

2.2.1. Tip-sample forces

AFM extracts information on the arrangement of atoms of sample surfaces via probing interaction forces between the tip and the sample. Due to the environment (ultra-high vacuum) and the use of non-magnetic tips in this thesis, friction and magnetic forces can be neglected. Therefore, three tip-sample forces have to be considered here.

Van der Waals force. The van der Waals (vdW) force[64] is caused by fluctuations in the electric dipole moment of atoms. The mutual polarization between such dipole-fluctuations cause a long-range attractive interaction and exists between all atoms or molecules. The vdW force between a spherical tip with radius R and a flat sample surface in distance z can be given as by the Hamaker approach:[65]

$$F_{vdW} = -\frac{A_H R}{6z^2} \tag{2.14}$$

where A_H represents the material-dependent Hamaker constant, depending on the type of materials of the tip and sample. This equation demonstrates that a sharp tip is desirable in AFM experiments as it reduces the vdW forces.

Chemical force. Chemical forces arise when two particles come close to each other, and their wave functions begin to overlap. Depending on the distance between particles, it can be either an attractive or a repulsive force.

Assuming that the distance between the outer-most tip atom and the closest surface atom is z, the total chemical and van der Waals interactions in AFM are usually described by the empirical Lennard-Jones (LJ) potential:[66]

$$E_{L-J}(z) = \varepsilon\left[\left(\frac{z_0}{z}\right)^{12} - 2\left(\frac{z_0}{z}\right)^{6}\right] \tag{2.15}$$

where ϵ represents the binding energy at the equilibrium position z_0, among $(1/z)^{12}$ represents the repulsive force at a close distance owing to Pauli repulsion originating from the overlap of the electron wave functions of the atoms between the tip and the sample. The other term $(1/z)^6$

represents the attractive forces caused by the vdW force described above. Therefore, the Lennard-Jones force (L-J Force) can be derived from this equation:

$$F_{L-J}(z) = -\frac{\partial E_{L-J}(z)}{\partial z} = 12\frac{\varepsilon}{z_0}\left[\left(\frac{z_0}{z}\right)^{13} - \left(\frac{z_0}{z}\right)^{7}\right] \tag{2.16}$$

Electrostatic force. The electrostatic force is from different electrostatic potentials (work functions) between the tip and the sample. The electrostatic potential difference between the tip and the sample leads to a capacitor with a capacity *C(z),* so the long-range and always attractive electrostatic force is given by:

$$F_{el}(z) = \frac{1}{2}\frac{\partial C}{\partial z}(V - V_{CPD})^2 \tag{2.17}$$

where V is the applied bias, V_{CPD} is the contact potential difference between the tip and sample. Because the AFM measurement is usually done at a constant bias of zero, the electrostatic force does not play a dominant role. However, when AFM images charged molecules on the surface, the electrostatic forces produced from the molecules can lead to distortions in bond-resolved AFM images.

Total force. Generally, the total force between the tip and sample is the competition between the long-range vdW and the short-range repulsive forces. Figure 2.5 displays the total force between tip and sample. It can be clearly seen that the vdW forces play a dominant role in the total force when the distance between the tip and sample is large, whereas the chemical forces become more significant when the tip-sample distance is small.

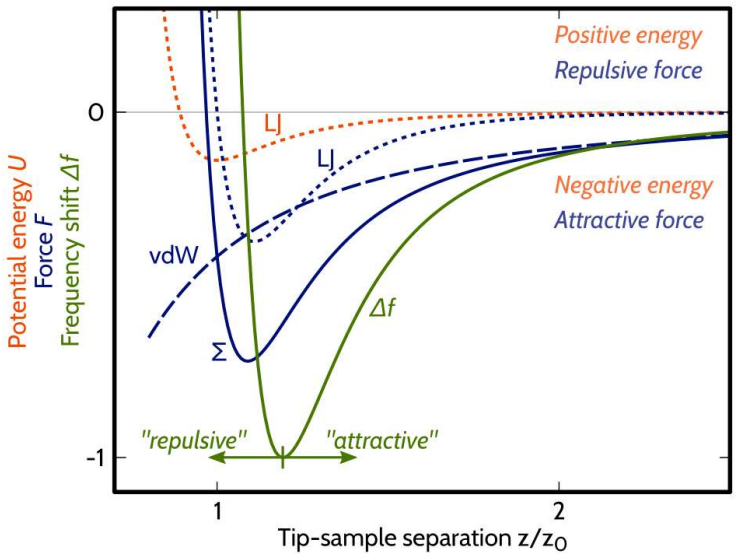

Figure 2.5: Typical interaction between tip and sample. The total potential and force arise from the interplay between van der Waals forces and Pauli repulsive forces. The accompanying frequency change is also depicted. This picture is taken from the ref. [67, 68].

2.2.2. Operational modes of an AFM

AFM can operate in the contact mode (or static mode) and in the non-contact mode (dynamic mode). In the contact mode, the tip on the cantilever and the sample can be damaged because the tip is always in contact with the sample's surface when scanning the sample. However, the non-contact mode is non-destructive, as the tip on the cantilever does not touch the surface. This mode is now widely employed in surface science for high-resolution imaging. It can

resolve bonds between atoms through tip functionalization and qPlus sensor technique (see section 2.2.4).

In non-contact mode, there are two modulation methods: amplitude modulation (AM)[69] and frequency modulation (FM).[70] In AM-AFM, the cantilever is driven by an external excitation to vibrate at a constant frequency that is slightly lower than its resonant frequency f_0, and with an initial amplitude A_0. When the tip on the cantilever interacts with the sample surface, the amplitude A changes with the variation of the tip-sample force. According to this change, a feedback loop will modulate the tip-sample distance to that keep the amplitude at A_0. In contrast to AM-AFM, in FM-AFM, the external excitation drives the cantilever to oscillate at its resonant frequency f_0 and a constant amplitude A. When the tip gets close to the sample's surface, the frequency f shifts with the variation of the tip-sample force. The frequency shifts ($\Delta f = f - f_0$) are recorded and used as the input signal for the feedback loop. In this thesis, all the AFM measurements were performed with FM-AFM mode based on the qPlus sensor.

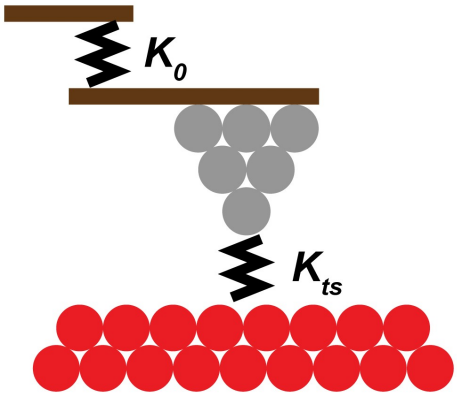

Figure 2.6: A schematic illustration of a simplified model of the tip and the sample. The cantilever is considered here as a rigid plate connected to a fixed base through a spring with spring constant k_0, only movable in vertical direction. The interaction between the tip and sample is characterized by the spring constant k_{ts}.

2.2.3. Frequency Modulation AFM

In FM-AFM, the cantilever oscillates at a constant amplitude and resonant frequency f_0 without external force. The tip-sample force is measured by the frequency shift Δf of the cantilever with respect to its unperturbed resonant frequency f_0. Considering the tip mounted on the cantilever as an effective mass m connected to a spring with a spring constant of k_0 (Figure 2.6), its resonant frequency f_0 is:

$$f_0 = \frac{1}{2\pi}\sqrt{\frac{k_0}{m}} \tag{2.18}$$

Due to the small amplitude of the cantilever oscillation, the tip can be assumed perpendicular to the surface. Therefore, the vertical force between the tip and sample is:

$$F_{ts} = -\frac{\partial U_{ts}}{\partial z} \tag{2.19}$$

where U_{ts} is the potential energy between the tip and the sample. The tip-sample force F_{ts} can be modeled as another spring connected between the mass m of the cantilever and the surface, with a spring constant k_{ts} (Figure 2.6). If k_{ts} keeps constant during all the oscillation cycles, the new oscillation frequency of the cantilever is:

$$f = \frac{1}{2\pi}\sqrt{\frac{k_0+k_{ts}}{m}} \tag{2.20}$$

where $k_0 + k_{ts}$ is the effective spring constant. The square root can be expanded in Taylor series ($\sqrt{1+x} = 1 + \frac{1}{2}x + \cdots$), so the new oscillation frequency can be written as:

$$f = f_0 + f_0\frac{k_{ts}}{2k_0} + \cdots \tag{2.21}$$

Assuming only the first-order approximation is considered. According to the definition of the spring constant $\delta F_{ts} = -k_{ts}\,\delta_z$, the relation between the frequency shift and the differential of the tip-sample force is:

$$\Delta f = -\frac{f_0}{2k_0}\frac{\partial F_{ts}}{\partial z} \tag{2.22}$$

This equation shows that the frequency shift is proportional to the force gradient of the tip-sample force. If k_{ts} cannot be considered constant during the oscillation cycle, please refer to the ref. [71].

2.2.4. High-resolution imaging

qPlus sensor. The choice of the cantilever is crucial in ensuring high-quality AFM measurements. Since the early 1990s, silicon has been the most commonly used material for AFM cantilevers. However, for high-resolution frequency-modulated AFMs, the qPlus sensor invented by Giessibl in 1996,[72, 73] shown in Figure 2.7, has been found to exhibit superior properties. The qPlus sensor consists of a quartz tuning fork, where one prong is glued to a heavy base plate, and a conducting tip is attached to one end of the other prong. The qPlus sensor affords the following advantages compared to the silicon cantilever: (1) High quality (Q) value: the energy loss to drive the oscillation of the cantilever is extremely small. (2) High stiffness:[74] the high stiffness can ensure the stability of FM operation and prevent jump-to-contact instabilities. (3) High thermal stability:[75, 76] the temperature of the system has a relatively low influence on Q-factor and resonance frequency. (4) Piezoelectric effect of quartz:[76, 77] the deflection signal of the qPlus sensor can be easily sensed through the piezoelectric voltages induced by the movement of the cantilever. In contrast to a piezoresistive cantilever, the qPlus sensor is suitable for low-temperature operations as it exhibits only negligible dissipation.

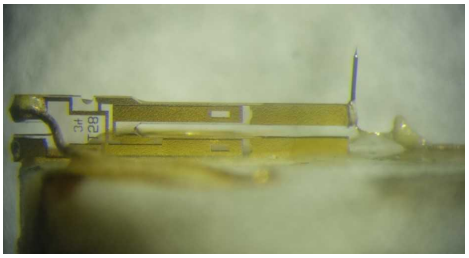

Figure 2.7: A picture of a qPlus sensor. The quartz tuning fork is glued on a heavy base plate and conducted by a gold wire. The conductive tip (here, tungsten) is glued at the end of the upper prong and conducted by an additional gold wire.

Tip functionalization. Modifying an apex of the tip with a single molecule or atom has been shown to enhance the imaging contrast for both STM and AFM greatly. Several molecules and atoms have been reported for the tip functionalization, including carbon monoxide (CO)[78, 79]

xenon (Xe),[80] bromine (Br),[81] and chlorine (Cl).[78] Among them, CO is the most commonly used species.

Functionalization of an AFM tip is achieved through vertical manipulation, such as placing the tip over a molecule or an atom (e.g., CO) and applying a constant voltage in the tip's direction, causing the molecule or atom to jump onto the tip (Figure 2.8a).[82] The CO molecules adsorbed on bare metal surfaces appear as depressions in the constant-current STM image obtained with a metal tip, as shown in Figure 2.8b. However, CO molecules show a bright spot in the center of the dark depression in the STM image (Figure 2.8c), after the tip picks up one CO molecule indicated by a white arrow. In contrast, a single oxygen atom in the upper left corner of the images is always imaged as a depression.[75, 82]

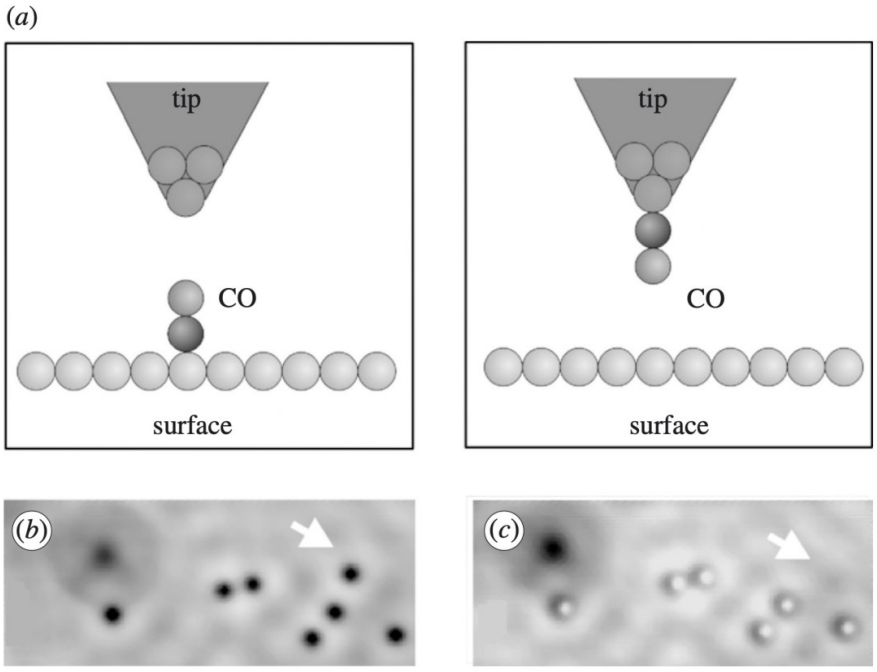

Figure 2.8: (a) Schematic of STM tip picking up a CO molecule via vertical manipulation from the surface to the tip apex. (b)-(c) STM images obtained with the tip before and after modification with a CO molecule. This picture is taken from the ref. [75].

2.3. X-ray photoelectron spectroscopy

X-ray photoelectron spectroscopy (XPS) is a surface analysis technique that can identify a sample's elemental and chemical composition. It is based on the photoelectric effect, which was first discovered by Heinrich Hertz in 1887[83] and later explained theoretically by Albert Einstein in 1905.[84] When a sample is irradiated with a beam of X-rays that have a specific energy, the absorption of individual photons excites core-level electrons of the sample's atoms (Figure 2.9). Some of these electrons will then be ejected from the sample, carrying a kinetic energy that is determined by the energy of the incoming photons $h\nu$, the binding energy of the corresponding core level relative to the Fermi level E_b, and the work function Φ:

$$E_{kin} = h\nu - E_b - \Phi \tag{2.23}$$

Using a hemispherical electron energy analyzer, the kinetic energy of the ejected electrons E_{kin} can be measured, allowing for the determination of the binding energy of the core level from which the electron was ejected. The typical range of X-ray energies used for accessing the core level electrons in this technique is between 100eV and 2000eV. Within this energy range, the

mean free path for inelastic electron scattering in solids is typically between 0.5-3 nm,[85] so that only electrons from the top layers contribute to the detected photoemission, making XPS a surface-sensitive technique. The binding energies of core levels are specific for each element and sensitive to the chemical environment. For example, chemical bonds that involve the sharing of valence electrons can alter the screening of the positive nuclear charge, thus affecting the binding energy of the core levels. From the peak intensities, the relative abundance of each contribution can be extracted, allowing determining quantitatively the chemical composition of the sample.[86] XPS requires a sample that is (semi)conductive in order to allow for the replacement of the removed electrons. For non-conductive samples, an electron flood gun is required to be added to the setup to avoid surface charging, which can result in a shift of the measured core level energies.

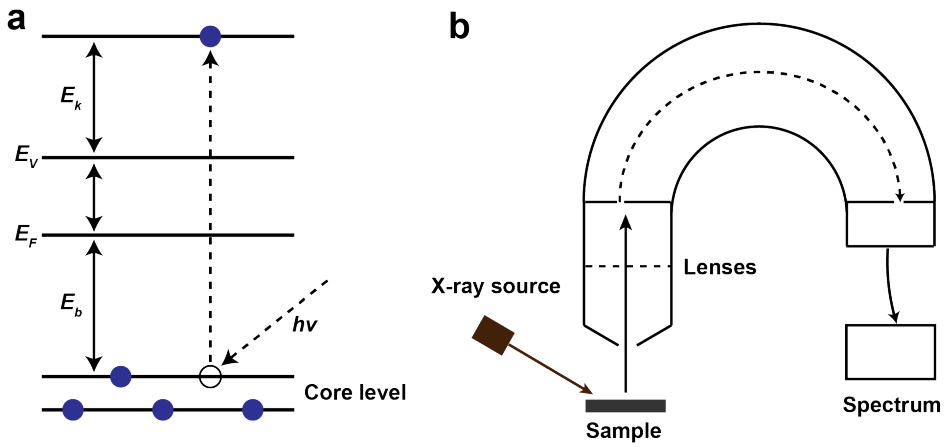

Figure 2.9: Schematic illustration of the photoemission process and the XPS energy analyzer setup. (a) A core-level electron is excited by an incident photon with energy *hv*. (b) The emitted photoelectron first goes through the lenses before it is collected by an energy analyzer and finally arrives at the detector.

2.4. Instrumentation

The experimental instruments used in this thesis are located in the TUM physics department E20 labs and WSI institute in Garching. The following sections will introduce the instrumental techniques, sample preparation procedures, and data analysis methods employed in the experiments. All experiments have been performed under UHV conditions, with base pressures of 3×10^{-10} mbar or lower.

2.4.1. Variable-temperature STM (VT-STM)

The Aarhus-type VT-STM (SPECS) is set up in a UHV system (Figure 2.10), comprising a preparation chamber (3) and an analysis chamber (2), which are separated by a vertical gate valve (8). The preparation chamber is utilized for the sample preparation, for example, surface cleaning using an Ar^+ sputter gun (5), depositing molecules onto the surface using a four-cell organic molecular beam epitaxy (OMBE, 4) (Figure 2.11a-b), and physical vapor deposition (PVD) of metals on the surface through home-built iron (Fe) metal evaporators (9) (Figure 2.11c). The molecules are filled in quartz crucibles with a diameter of 5 mm in the OMBE and sublimated into the vacuum by heating. The parking stage (11), which includes a heating stage, is designed to accommodate up to four samples. It allows for electron beam heating of the samples, with temperatures reaching up to 1200 K. After the preparation process, the sample can be transferred to the analysis chamber using a combination of various manipulators. The

load-lock chamber (7) is used to transfer samples from air into the UHV condition without breaking the vacuum.

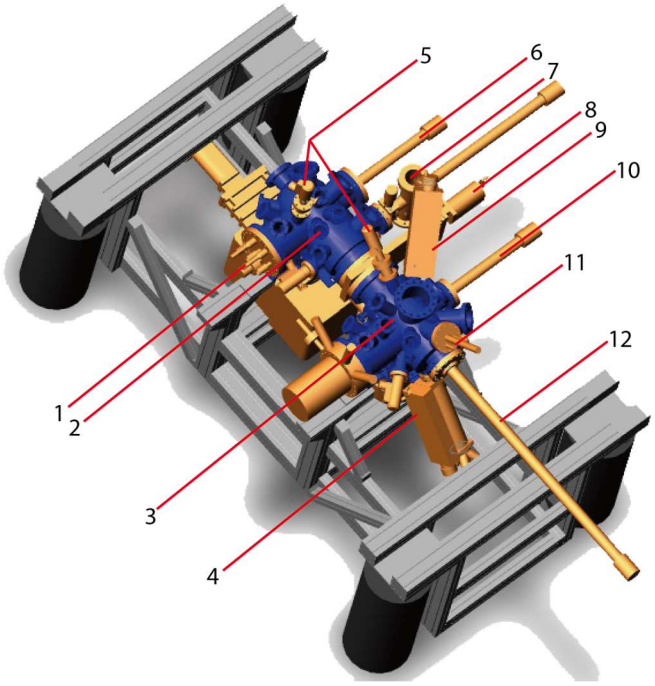

Figure 2.10: Setup of the UHV chamber. (1) The variable-temperature Aarhus STM head, (2) STM chamber, (3) preparation chamber, (4) OMBE, (5) argon sputter guns in both chambers to sputter the sample and the STM tip, (6, 10, 12) manipulators, (7) load-lock chamber, (8) gate valve, (9) metal evaporator, (11) sample parking stage. This picture is taken from the ref. [87].

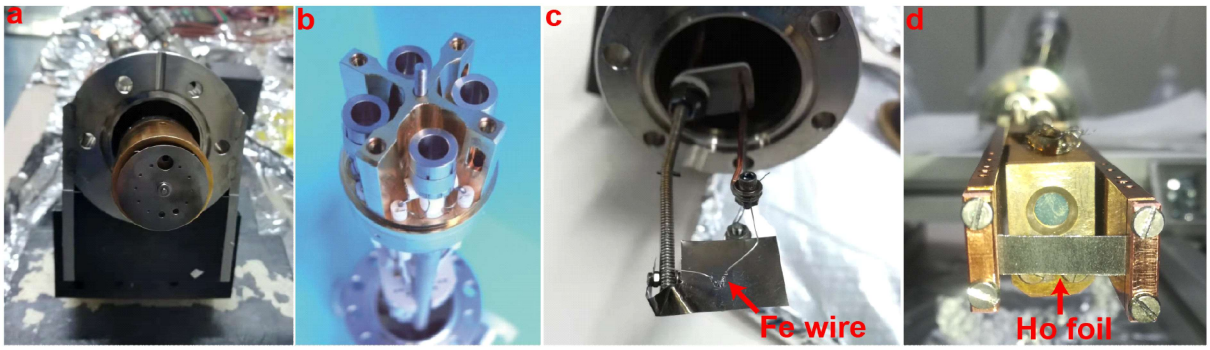

Figure 2.11: (a-b) Image of OMBE with four independent crucibles. (c) Image of the home-built Fe and (d) holmium (Ho) metal evaporator.

The cross-section side view of the Aarhus STM head is presented in Figure 2.12. The pre-mounted sample is inserted into the scanning stage and securely fixed with two clamps (3). The STM scanner is positioned on top of an inchworm motor (9), which serves the purpose of a coarse tip-to-surface approach. This motor allows for controlled movement of the tip in order to bring it closer to the surface for scanning. The piezo motor (7) can further move the tungsten tip (6) that is sharpened by electrochemical etching. The scanner is mounted inside the base plate (4) and fixed with ceramic balls (10). A Zener diode (12) is used to heat the STM scanner and keep it at room temperature while cooling the sample. The sample and scanner platform can be cooled down by liquid nitrogen (LN_2) via a cooling piston (11). To ensure isolation from external vibrations, the entire STM setup is suspended using springs (13).

The ultra-high vacuum system is equipped with a three-stage pumping system connected in series to maintain the required vacuum conditions. The initial pumping stage of the system utilizes a rotary pump, which is capable of reducing the pressure to approximately 10^{-3} mbar. A compact turbo molecular pump is used as the second pumping stage to further decrease the pressure to approximately ~10^{-7} mbar. The main pump, situated at the bottom of the preparation chamber, is a large turbo molecular pump capable of evacuating the entire system to a base pressure of up to 2×10^{-10} mbar after a thorough bake-out process. Additionally, there is an ion-getter pump located in the STM chamber, which contributes to the overall performance of the pumping system. It is suitable for STM measurements by not introducing additional sources of noise.

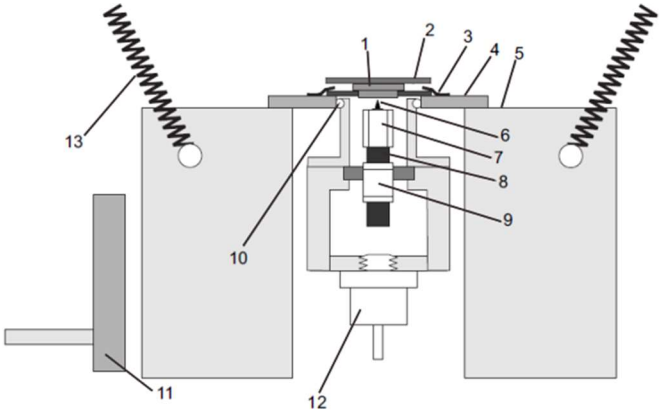

Figure 2.12: Cross-section side view of the Aarhus STM head. (1) crystal, (2) sample holder, (3) clamps, (4) base plate, (5) aluminum block, (6) tungsten tip, (7) scanner piezo motor, (8) SiC rod, (9) inchworm piezo motor, (10) ceramic balls, (11) cooling finger, (12) Zener diode, (13) suspension springs. This picture is taken from the ref. [87].

2.4.2. Low temperature STM/AFM (LT-STM/AFM)

In order to obtain chemical bond resolution, a commercial LT-STM/AFM instrument (CreaTec) was used. Figure 2.13 depicts a schematic diagram of the instrument, which consists of two chambers (a preparation chamber and a SPM chamber) with a load-lock chamber. These chambers are separated by gate valves.

Cooling and damping system. Chemical bond resolution imaging is conducted at low temperatures to achieve high resolution and minimize thermal drift. To achieve the low temperatures, a cryostat is employed, as Figure 2.13 and 2.14 show. The core components of the cryostat are the inner liquid helium (LHe) dewar and the outer LN_2 dewar. These two dewars are separated by high vacuum insulation to prevent heat convection between them. The scanner is positioned directly beneath the LHe Dewar and is connected to a thermal conductor, enabling efficient cooling of the scanner. In addition, the scanner is enclosed by a two-layer shielding system consisting of LHe and LN_2 shields. These shields are connected to their respective dewars and effectively block external thermal radiation. With the cooling setups described above, the LT-STM/AFM operates at a low temperature of approximately 5 K.

To mitigate the influence of external vibrations on imaging quality, the instrument is mounted on four damping legs. This setup effectively minimizes noise and ensures a stable operating environment for precise imaging. The entire instrument will be floating on these damping legs during the measurements. Similarly, vibrations can also be induced by the cryostat. The gasification process of LHe and LN_2 can generate noise in the frequency range of 500 to 800 Hz due to the outlet of the Dewars directly connected to the atmosphere. In order to

reduce this noise, the scanner is suspended using springs and incorporates eddy current damping. Additionally, the entire instrument is grounded to isolate and minimize electrical noise.

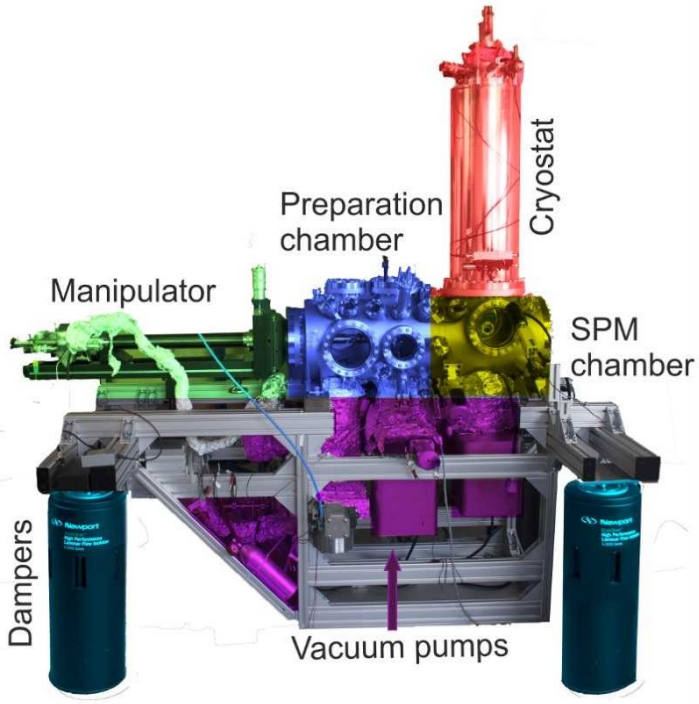

Figure 2.13: Picture of the LT-STM/AFM instrument. Different components of the instrument are highlighted with different colors. The load-lock chamber, although not depicted in this illustration, is a movable component that can be affixed to the preparation chamber. This picture is taken from the ref. [68].

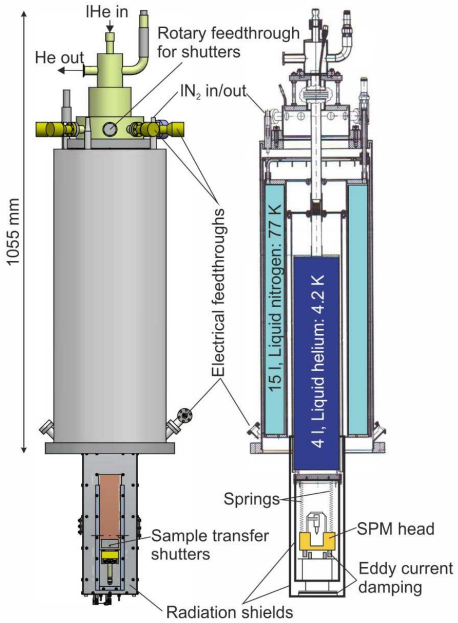

Figure 2.14: Schematic of the cryostat. The dark blue region, representing the inner Dewar, is filled with LHe, while the light blue area, representing the outer Dewar, is filled with LN_2. The picture is adapted from the ref. [88].

Scanning system. The essential components of the scanning system consist of a scanner (Figure 2.15), a qPlus sensor (CreaTec) (Figure 2.7), and Nanonis controllers (SPECS). The

qPlus sensor, invented by Giessibl in 1996,[72, 89] is considered the crucial component for nc-AFM measurements. As depicted in Figure 2.15, one side of the tuning fork is attached to the ceramic base using an adhesive. Additionally, a tip, typically made of tungsten, is fixed to the free prong of the tuning fork. The deflection signal is produced through the piezoelectric effect and can be detected by reading the output from the two electrodes of the tuning fork.

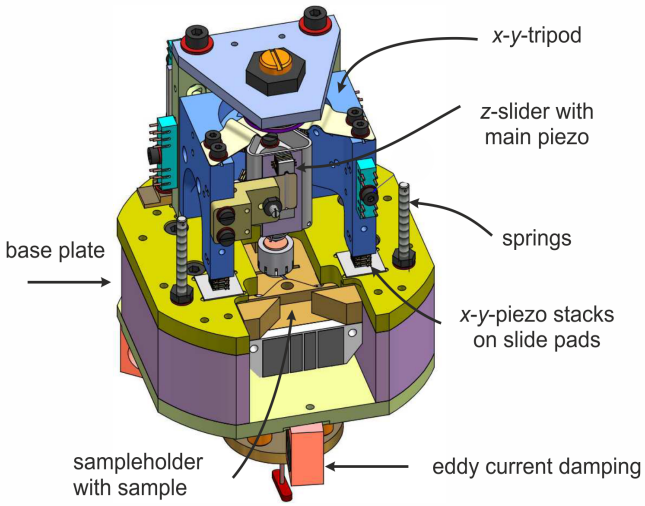

Figure 2.15: Schematic drawing of SPM scanner (Adopted from ref. [68]).

2.4.3. Joule-Thomson STM (JT-STM)

Some of the STM data and STS spectroscopy in this thesis were obtained from a commercial JT-STM instrument from SPECS company (Figure 2.16). The pumping, cooling, and damping equipment used in the JT-STM are similar to the LT-STM/AFM. The primary distinctions lie in the STM scanner (Figure 2.16b-c) and sample holder (Figure 2.18b-c). In addition, the notable feature of this system is the JT-cooler, which is capable of reducing the temperature of the sample to approximately 1.2 K via the Joule-Thomson effect. In this thesis, no STM measurements were carried out at 1.2 K, so we do not give more detail on the Joule-Thomson effect and the related process of cooling. A more detailed description of this instrument can be found in the thesis of R. Hellwig ref. [90].

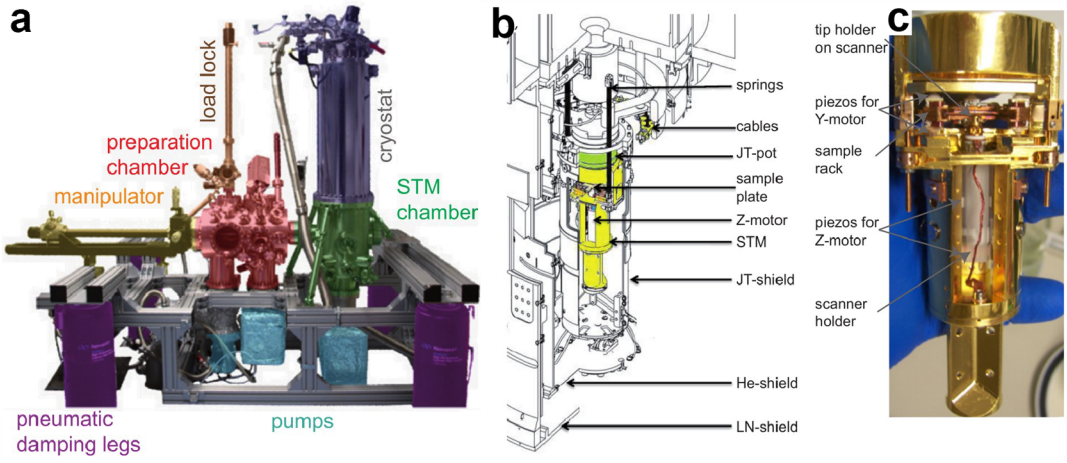

Figure 2.16: (a) Picture of the JT-STM setup. (b) Schematic drawing of the STM head. (c) Picture of the STM head. All pictures are taken from the ref. [90].

2.4.4. SPECS – XPS

Figure 2.17 shows the commercial SPECS GmbH XPS setup employed in this work. It consists of two chambers (a preparation chamber and an analysis chamber) and a load-lock chamber. The analysis chamber includes a PHOIBOS 150 hemispherical analyzer, an XR 50 X-ray source providing monochromatic Al Kα / Mg Kα radiation, and a FR 50 X-ray source supplying non-monochromatic Mg Kα / Al Kα radiation. Before XPS measurements, the sample must be transferred to the analysis chamber using a manipulator. The sample (Figure 2.18d) on the manipulator is usually held at 300 K when the measurements are carried out but can be cooled down by LN_2 and heated up by a combined filament/electron-impact heating.

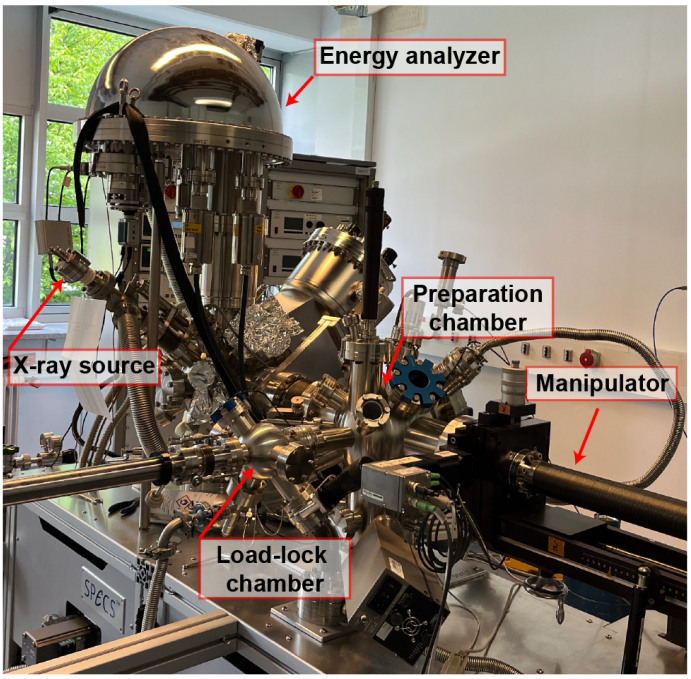

Figure 2.17: Picture of the SPECS-XPS setup.

2.4.5. Sample preparation

All sample preparations adhere to a similar procedure. Initially, the substrate surfaces are cleaned within a preparation chamber. Following that, organic precursor molecules and metal atoms are thermally deposited onto the substrate using an OMBE technique and home-built metal evaporators, respectively. The details are elucidated in the following.

The substrates utilized in this thesis are single crystals of Au(111), Ag(111), and Ag(100), and they are mounted on the sample holder (Figure 2.18). The preparation of a clean and atomically flat crystal was achieved by several cycles of Ar^+ sputtering and subsequent annealing to a temperature in the range of 700-720 K. After completing the aforementioned cleaning procedures, the surface is suitable for OMBE.

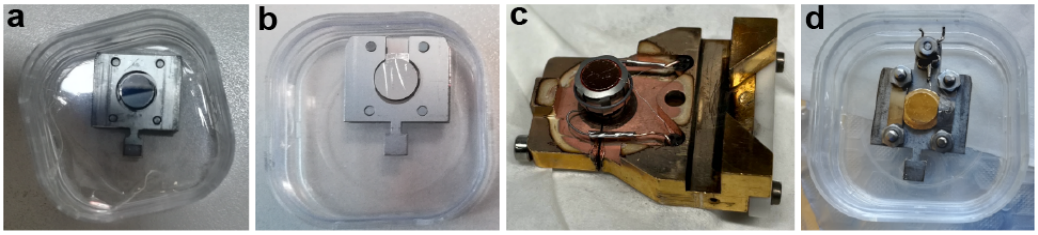

Figure 2.18: Sample holder and crystal used in VT-STM (a), JT-STM (b), LT-STM/AFM (c), XPS (d) respectively.

Organic molecules are deposited from a quartz crucible at temperatures that allow for their sublimation. Figure 2.19 presents the chemical structures of all used precursors in this thesis. Indigo (TCI, exceeding 97% dye content), 6,6'-dibromoindigo (Tyrian purple, Sigma-Aldrich, exceeding 95% dye content), and 1H,1'H-2,2'-Bibenzo[d]imidazole (H_2bbim, TCI, exceeding 97% purity) were deposited by heating the respective crucibles at 493-523 K, 533-553 K, and 473 K respectively. All substrates were held at room temperature during deposition. The deposition time was appropriately controlled to attain the desired molecular coverage.

Transition metal atoms were sublimated from a thin wire (Alfa Aesar, 99.995% purity for Fe), which was wound around a tungsten wire, resistively heated by direct current (Figure 2.11c). Lanthanide atoms were sublimated from a foil (Alfa Aesar, 99.9% purity for Ho), which was clamped by copper rods carrying an alternating current (Figure 2.11d). The deposition flux and adsorbate concentration could be calibrated through STM imaging and were adjusted by controlling the filament heating current and deposition time. All substrates also were held at room temperature during deposition. After the evaporation of molecules and metals, the sample can be annealed to promote the assembly between molecules and metals or activate molecular on-surface reactions.

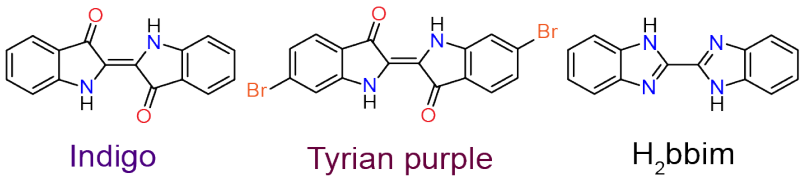

Figure 2.19: Chemical structures of the precursor molecules studied in this thesis.

2.4.6. Data acquisition and analysis

STM and AFM data. STM images were taken using the constant current mode (unless mentioned otherwise) and the bias voltage was applied to the sample. All AFM images were acquired at constant heights with V_s = 0 V using a qPlus tuning fork sensor[91] (resonance frequency ~ 31 KHz, oscillation amplitude 60-80 pm, Q value > 100000, stiffness ~ 1800 Nm^{-1}) operated in frequency modulation mode. The data was analyzed using three software tools: WSXM,[92] IGOR Pro 6.3 (a special package for STM analysis), and SpmImage Tycoon.[93]

XPS data. All XPS data were obtained from the SPECS-XPS setup described above and were acquired with a monochromatic Al Kα source ($h\nu$ = 1486.71 eV) and a SPECS Phoibos 150 hemispherical analyzer in normal emission geometry. All XPS data were analyzed and fitted via CasaXPS software.[94] The binding energy of all spectra was calibrated with the Ag $3d_{5/2}$ (or Au $4f_{7/2}$) core level of the silver at 368.46 eV (84.19 eV).

DFT Calculations. In chapter 3, calculations were performed using the spin-polarized DFT+U method, as implemented in the Quantum ESPRESSO package. Exchange-correlation interactions were treated using the vdW-DF2-B86R functional. The pseudization of core electrons was described using projector augmented wave (PAW) pseudopotentials. Surface unit cells corresponding to supercell matrices of $\begin{pmatrix} 7 & 1 \\ 4 & 5 \end{pmatrix}$ and $\begin{pmatrix} 5 & -4 \\ 1 & 2 \end{pmatrix}$ were used for the coordination polymers on Ag(111) and Ag(100) respectively. The metal substrates were modelled using 3 atomic layers. The values presented here are for a value of the Hubbard onsite

parameter U = 1 eV; however it has been verified that the results are robust for a range of U values.

3. On-surface isomerization of indigo within 1D coordination polymers

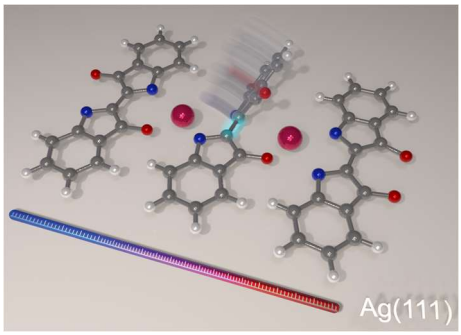

Introduction

Indigo (molecular reactant in top row of Figure 3.1) is a common, ancient pigment with a distinctive blue color. More recently, its molecular properties have attracted the interest of both fundamental and applied research.[95] Among them, the various metal complexes of indigo[96-99] and its derivatives[100, 101] have been explored and found application in redox-[102] and electro-[103] chemistry as redox-switchable ionophores[104, 105] and organic-based battery materials.[103] Notably, indigo can chelate metal ions with its N and O atoms. Thus individual metal complexes sandwiched between two indigo derivatives have been created and studied on surfaces.[106] Extension of this coordination offers the possibility of forming natural compound coordination polymers (CPs), such as the Ni-CPs of the related natural dye, Tyrian purple (6,6′-dibromoindigo, molecular reactant in bottom scheme 1).[107] CPs exhibit desirable properties for gas adsorption and packing,[108] catalysis,[109] photoluminescence,[110] magnetic information storage and spintronics.[111] More recently, surface-confined metallosupramolecular engineering has emerged as a route towards unique CPs[112-118] with unconventional electronic[119, 120] and magnetic properties,[121-123] making them suitable for multiple applications including magnetic information storage and spintronics.

The neutral indigo has an intriguingly high photostability[124] and its *trans-cis* photoisomerization has been the subject of scrutiny for mechanistic insights.[125-129] The factors inhibiting photoisomerization in indigo include intramolecular NH···O=C hydrogen bonds in the *trans* isomer, efficient excited-state proton transfer, and efficient nonradiative internal conversion.[125, 130-133] Interestingly, in the absence of the intramolecular H-bonds, *N,N′*-disubstituted indigos[134, 135] (such as *N,N′*-diacyl,[136, 137] *N,N′*-dimethyl,[126, 138] and *N,N′*-di(tert-butyloxycarbonyl)[139] indigos) undergo photoisomerization, expanding their application in photoswitches.[140, 141] In addition, isomerization of indigo can be induced by heating,[142] protonation[143] and catalysts such as transition metal ions.[96, 99] In particular, *cis*-indigo is posited as a promising material for optoelectronic devices, based on calculated electronic properties by density functional theory (DFT).[144]

Here we explore nanostructuring under surface confinement, providing access to otherwise unattainable compounds. This approach is conveniently coupled with direct visualization and molecular identification using scanning probe microscopy techniques such as scanning tunneling microscopy (STM) and noncontact atomic force microscopy (nc-AFM) with CO-functionalized tips.[1-3, 78, 145, 146] In particular one dimensional (1D) CPs[119, 121, 147, 148] have been fabricated and isolated through careful development of interfacial metallosupramolecular engineering protocols,[149-152] relying on metal-ligand interactions operative between metal

adatoms and suitable linker groups. Specifically, we observe metal-directed assembly of distinct 1D CPs incorporating dehydroindigo molecules and iron (Fe) adatoms on the Ag(111) and Ag(100) surface. Combining analysis of STM, AFM and X-ray photoelectron spectroscopy (XPS) measurements with DFT calculations, we identified the *trans* and *cis* configurations as well as the ligand chemical modification, affording N,O- and N,N- plus O,O-chelation within the CPs. The substrate packing proves important in this process: no isomerization was found in the CPs for indigo (or 6,6′-dibromoindigo) with Fe adsorbed on the Ag(100) surface. DFT calculations further shed light on the molecular adsorption, coordination motifs and isomerization process. This investigation points to a fascinating playground for the realization of interfacial metal-organic nanosystems, in which tuning the linker isomerization affords different types of coordination polymers.

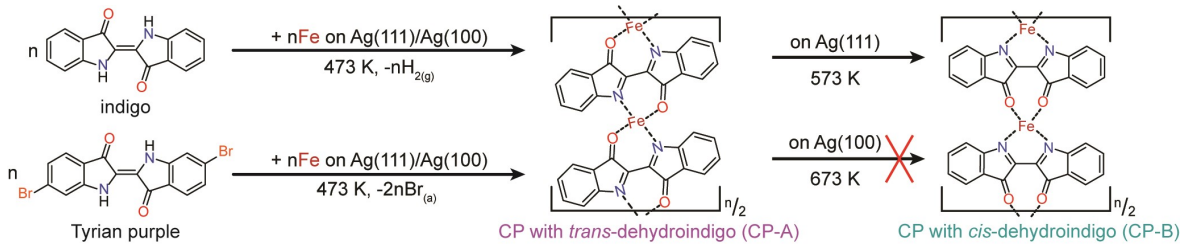

Figure 3.1: Chemical schemes of the on-surface formation of CPs presented in this work. Trans and cis molecular monomers of dehydroindigo afford N,O- and N,N- plus O,O-chelation within the CPs.

Results and Discussion

Deposition of a submonolayer of indigo molecules and Fe atoms on a Ag(111) surface held at room temperature (r.t., 300 K) and subsequent annealing at 573 K leads to the formation of isolated CPs, as shown in Figure 3.2a. Within these CPs, one can distinguish two kinds of molecular arrangements considering the angle between the molecular axis and the CP direction. While an acute angle of approximately 73° is measured in CP-A segments (rendered in a magenta color scale), a right angle is obvious in CP-B segments (rendered in a cyan color scale). The monomer of CP-A is imaged in the STM images as an S-shaped protrusion, attributed to the organic ligand (marked by a S-line on Figure 3.2a) and a bright round protrusion, attributed to the metal center (marked by a dot on Figure 3.2a). Notably, the S-shaped protrusion is consistent with the STM imaging of indigo on Cu(111).[153, 154] CP-B is comprised of a clearly distinguishable monomer: a U-shaped and a round protrusion, indicated on Figure 3.2a by a U-line and a dot, respectively. Interestingly, further annealing of the sample at 623 K, leads to CPs comprised predominantly of extended CP-B, which aggregate into self-assembled islands (see Figure 3.3).

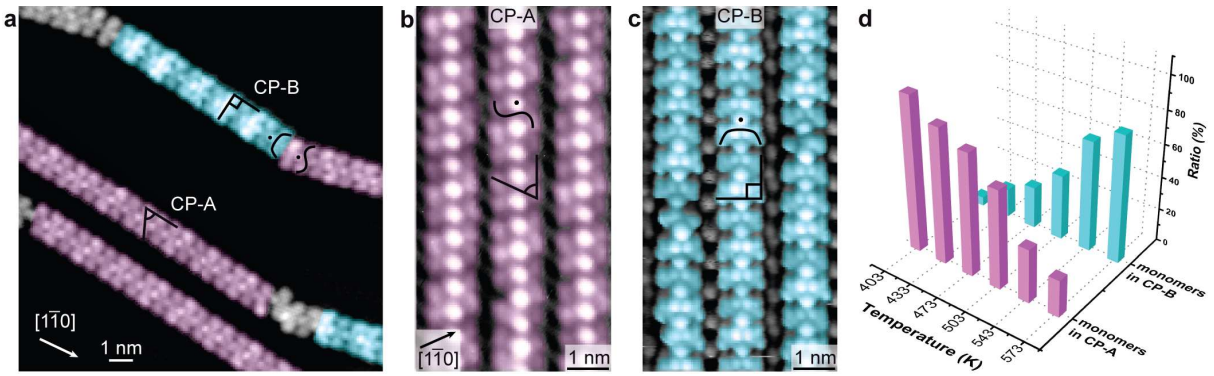

Figure 3.2: STM analysis of CPs constituted with indigo or Tyrian purple molecules and Fe atoms on Ag(111). a) Representative overview STM image (0.1 V, 100 pA, 4.6 K) of the CPs on Ag(111) after annealing a submonolayer coverage of indigo with Fe atoms at 573 K. Two types of polymers are

observed, differing in the monomer shape and the orientation of the monomer backbone with respect to the chain direction: CP-A and CP-B, colored cyan and magenta, respectively. b-c) High-resolution STM images of CP-A (1.5 V, 70 pA, r.t.) and CP-B (1.0 V, 100 pA, r.t.) evolving on Ag(111) upon annealing a submonolayer of Tyrian purple with Fe atoms. A high symmetry direction of the Ag(111) surface as well as the angles between the molecular backbone and the chain direction are indicated. d) Distribution of monomers in CP-A and CP-B as a function of annealing temperature of Tyrian purple and Fe on Ag(111).

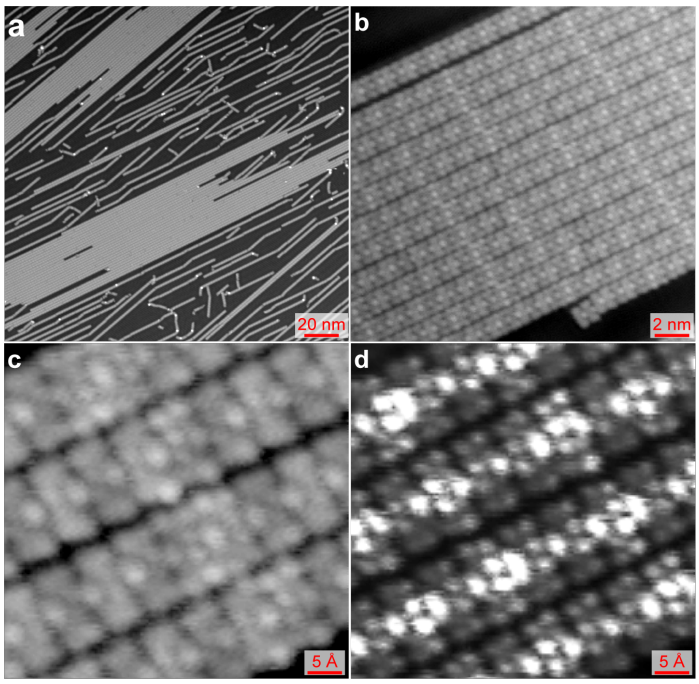

Figure 3.3: STM images of CP-B formed by annealing indigo and Fe on Ag(111) at 623 K. (a-c). Constant current images. (d) Constant height image. Imaging parameters: (a) -500 mV, -100 pA; (b) -100 mV, -100 pA; (c) -10 mV, -100 pA; (d) 10 mV. All STM images were acquired at 4.6 K.

Similar results are obtained by employing the same fabrication protocol after replacement of indigo with Tyrian purple: both CP-A and CP-B segments can be found as shown in the high-resolution images of Figure 3.2b-c. These are identified by the distinctive monomer features, allowing us to conclude that the same CPs are formed by both natural compounds of indigo and Tyrian purple on Ag(111). The overview STM images shown in Figure 3.4 reveal that CP-B is predominantly expressed following annealing at 573 K. Figure 3.2d presents the relationship between annealing temperature and the portions of the monomers within CP-A and CP-B (raw data in Figure 3.5). Similar to the case of indigo, CP-B is clearly preferred with increasing annealing temperature.

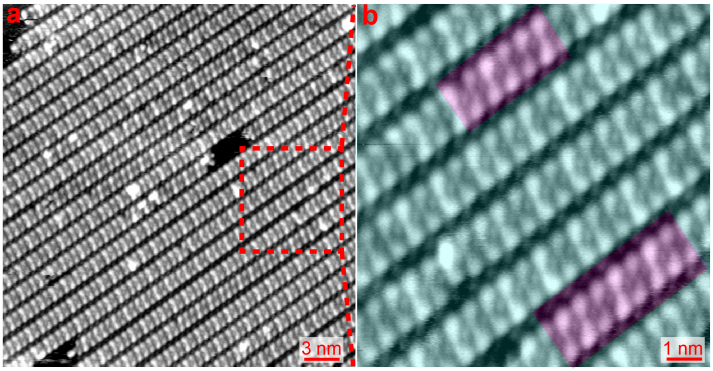

Figure 3.4: STM images of Tyrian purple and Fe on Ag(111) after annealing at 573 K. (a) Overview and (b) zoom in the area indicated by a dotted in (a). In (b), CP-A and CP-B segments are rendered in magenta and cyan, respectively. Imaging parameters: (a) -2 V, -90 pA; (b) -1.2 V, -60 pA. All STM images were acquired at r.t..

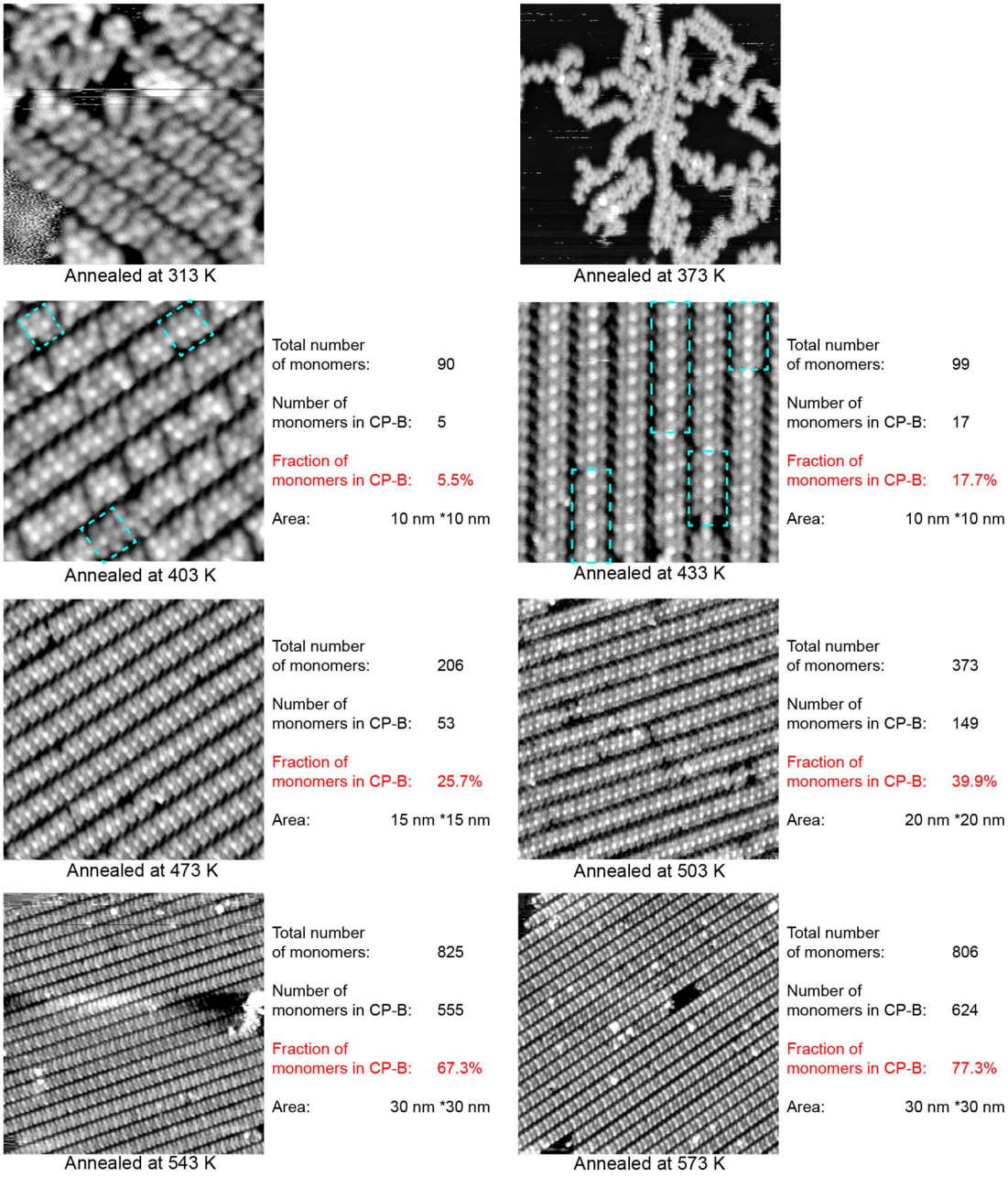

Figure 3.5: STM images of CPs formed by annealing Tyrian purple and Fe on Ag(111) at various temperatures. These images were used to count the CP-B monomers with changing temperature. Imaging parameters: (a) -1 V, -70 pA; (b) -2.1 V, -100pA; (c) -0.7 V, -60 pA; (d) -1.2 V, -60 pA; (e) -2 V, -100 pA; (f) -1.7 V, -80 pA; (g) 1 V, 70 pA; (h) 1.9 V, 120 pA. All images were acquired at r.t..

To obtain a chemical identification of the monomers within CP-A and CP-B, a series of XPS measurements was carried out. In particular, relevant core levels were probed to investigate the chemical alterations to the monomer deposited at r.t. on Ag(111) before and after the addition of the second component (Fe) and heat treatment. The complete set of data can be found in Figure 3.6, whereas Figure 3.7 shows the most informative spectra corresponding to the O 1s and N 1s regions after initial deposition of Tyrian purple on the Ag(111) surface at r.t. (bottom),

and following the addition of Fe atoms and annealing at 473 K (top). Without Fe deposition, the O 1s spectrum shows a prominent peak with a binding energy (BE) centered at 530.2 eV, which is assigned to the *keto* group in the indigo backbone hybridizing strongly with the substrate metal states.[155] A small shoulder can be noticed at 531.2 eV, which might originate

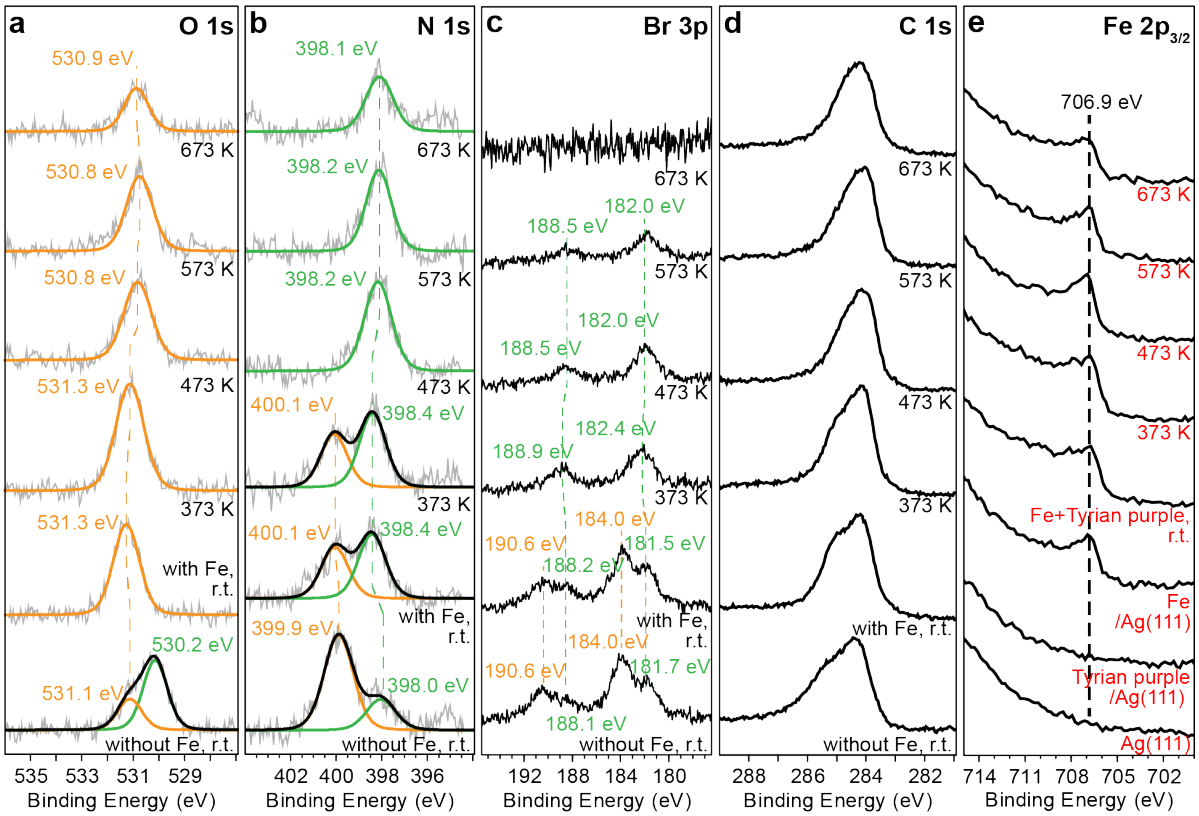

Figure 3.6: XP spectra of the (a) O 1s, (b) N 1s, (c) C1s, (d) Br 3p and (e) Fe 2p 3/2 regions of Tyrian purple (in absence and presence of Fe adatoms) on Ag(111). Proof of the presence of Br atoms on the Ag surface visualised by STM (grey features in Figure 3.2b-c between CPs) is found in the Br 3p XP spectra (c): only two peaks, located at 182.4 eV and 188.9 eV representing the Br 3p doublet, are observed after annealing at 373 K, consistent with Br adsorbed on Ag. Therefore, all Tyrian purple molecules on the surface are debrominated following annealing at 373 K. The debromination sites are likely to be hydrogen-passivated as in our STM images (e.g. Figure 3.2b-c, Figure 3.5) no dimers, oligomers nor metal intermediates indicative of Ullman-coupling are visible. Isolated CPs in samples of Tyrian purple with Fe on Ag(111) can be observed at low temperatures, e.g., see the CP-B depicted in Figure 3.8.

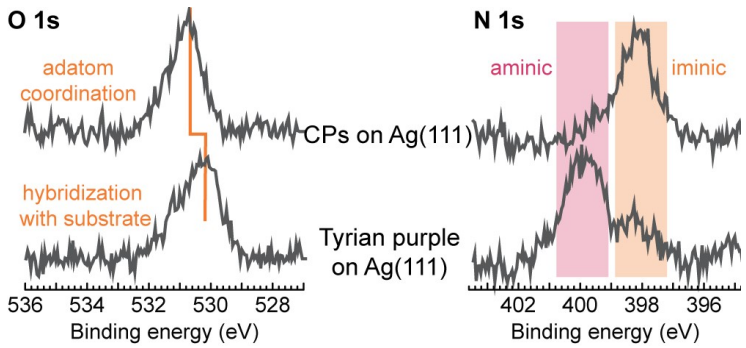

Figure 3.7: O 1s and N 1s spectra of pure Tyrian purple on the Ag(111) surface (bottom) and with the addition of Fe adatoms and annealing to 473 K, corresponding to the formation of CPs (top).

from *keto* groups without strong substrate hybridization[155] presumably due to local supramolecular self-assembly. Correspondingly, the N 1s spectrum shows two peaks with a BE of 399.9. eV and 398.0 eV, in good accord with aminic and iminic N atoms on metal surfaces, respectively.[156, 157] We thus infer that a small portion of N–H scission occurs already at r.t. on the Ag(111). Concomitantly, we observe the scission of C–Br (cf. Br 3p spectra in Figure 3.6d).[158] As there is no evidence in the imaging of the molecular products of reactive C atoms resulting from the C–Br bond cleavage (as e.g. dimers, oligomers or metal intermediates indicative of Ullman-coupling), it is proposed that this C site is passivated with H originating from the on-surface N–H scission and/or from residual H_2 in the UHV environment.[159] Surface Br atoms are evident both in the XPS spectra (Figure 3.6d) and in the STM data as bright protrusions[160] between the CPs (see Figure 3.2b-c), where they mediate the CP self-assembly into islands by hydrogen bonding.[161] After addition of Fe atoms and annealing to 473 K triggering CP formation, the O 1s and N 1s spectra show sole peaks centered at 530.8 eV and 398.1 eV, respectively. The O 1s shift to higher binding energy is consistent with observations of on-surface coordination between carboxylate moieties and Fe atoms.[162] Also the N 1s BE is consistent with Fe coordination.[163] Upon annealing to 673 K, these regions remain unaffected, indicating that the O and N atoms have the same chemical state in CP-A and CB-B (Figure 3.6a-b). We thus conclude that all N and O atoms are coordinated by Fe atoms in both CP-A and CP-B polymers.

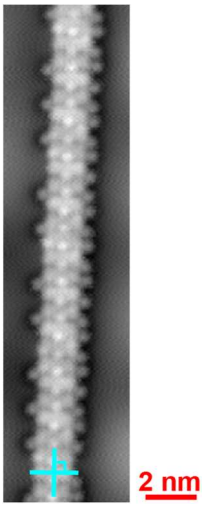

Figure 3.8: High resolution STM image (-5 mV, -100 pA, 4.6 K) of isolated CP-B formed by Tyrian purple and Fe on Ag(111). The orthogonal orientation of the monomer with respect to the polymer direction is indicated in blue.

Having the chemical identification of the monomers, we turn our attention to the high resolution STM and nc-AFM imaging, in order to identify the monomers isomeric forms in CP-A and CP-B. Upon close inspection, we attribute CP-A to molecular monomers of *trans*-dehydroindigo stabilized by two kinds of coordination bonds (C=O···Fe and =N···Fe), affording N,O chelation. A structural model was optimized by DFT calculations (Figure 3.9). The model clearly demonstrates the *trans*-N,O-N,O coordination of Fe by two dehydroindigo molecules. The distance *d* between two adjacent Fe atoms is 6.33 Å, in good agreement with the measured value of 6.3 ± 0.2 Å. The assigned structure is further supported by the simulated STM appearance (Figure 3.9c), which nicely reproduces the experimental STM image, manifesting that the two small dots close to the center of every single *trans*-dehydroindigo can be associated to the two carbonyl groups. To indisputably confirm the coordination structure,

the bond-resolved nc-AFM technique with CO tip functionalization[78] was also utilized to inspect CP-A (Figure 3.9a, right). The confirmation of the *trans*-dehyroindigo configuration is achieved *via* the clear visualization of the indole 6-membered ring orientation and the adatom in the coordination node, in good agreement with the STM-simulation of the model. In addition, images show that bright features associated with the carbonyl groups are on opposite sides of the molecule (see also the AFM simulation[164, 165] in Figure 3.10).

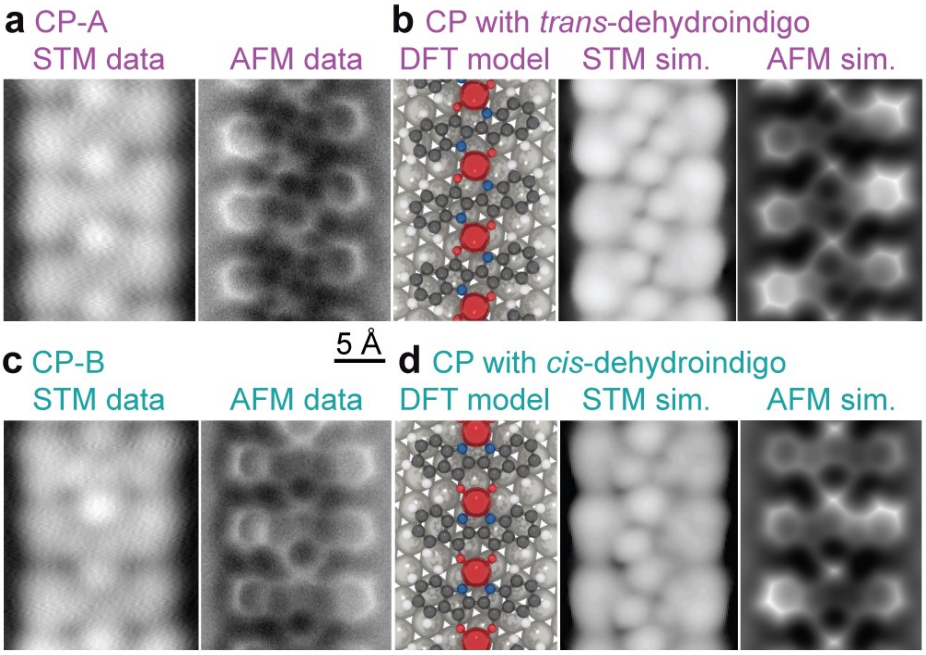

Figure 3.9: CP-A and CP-B structural identification. (a) High resolution STM image (left, -0.1 V, 100 pA, 4.6 K) and AFM image (right) of a representative CP-A chain formed by indigo and Fe on Ag(111). (b) DFT optimized model of a CP chain with three *trans*-dehydroindigo monomers next to the corresponding simulated STM image[60] (center) and AFM image[164, 165] (right). (c) High resolution STM image (left, 0.1 V, 100 pA, 4.6 K) and AFM image (right) of a representative CP-B chain formed by indigo and Fe on Ag(111). (d) DFT optimized model with three *trans*-dehydroindigo monomers next to the corresponding simulated STM image[60] (center) and AFM image[164, 165] (right). All images are on the same scale. C, O, N, H, Fe and Ag atoms are depicted in black, red, blue, white, rust and silver, respectively.

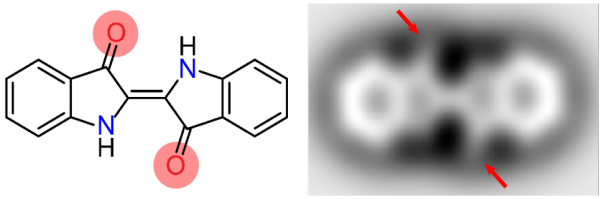

Figure 3.10: Simulated nc-AFM image of an isolated indigo molecule (structural formula on the left). The red arrows mark the positions of the O atoms.

Likewise, we studied the CP-B that features monomers perpendicular to the chain direction, separated by the same distance *d*. To account for the symmetry of the molecular monomer, we ascribe CP-B (Figure 3.9c) to a CP composed of *cis*-dehydroindigo and obtained the DFT-optimized structural model shown in Figure 3.9d, left. Conceivably, an indole of the *trans*-dehydroindigo flips around the center C–C bond, affording N,N-O,O coordination. The excellent match of the simulated STM (Figure 3.9d, center) and bond-resolved AFM (Figure 3.9d, right) verifies unambiguously the proposed molecular model.

Indigo features a central C=C double bond (see inset outlined in pink, Figure 3.11a). The isomerization observed would require a rotation around this bond, which would be indicative of the nature of a single C–C bond. By means of DFT we investigated the central C–C bond lengths of *trans*-indigo and *trans*-dehydroindigo (see inset outlined in orange in Figure 3.11a) as a measure of the single vs. double bond character. Indeed, for isolated species the bond distance increases significantly from the indigo molecule (1.368 Å) to dehydroindigo (1.438 Å). An increase in the bond length is also found for the corresponding adsorbed species, indicating that a rotation around this bond is likely feasible due to the N-H bond scission caused by the Fe coordination.

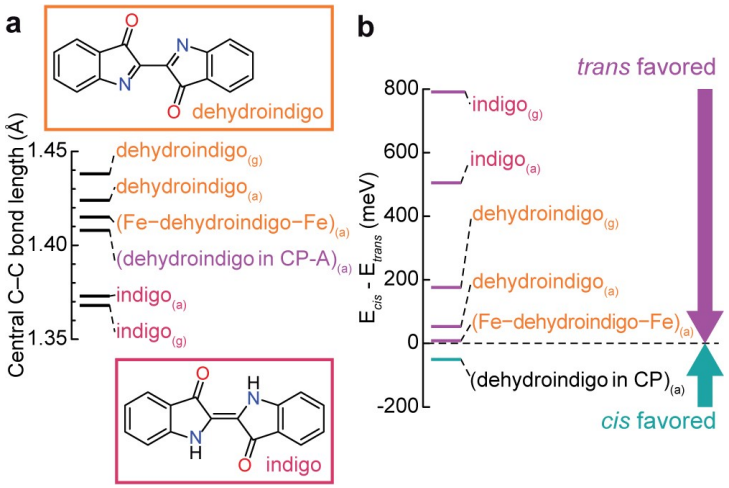

Figure 3.11: DFT analysis of geometry and energy of the isomerization. a) Comparison of the central C–C bond lengths of *trans* indigo and dehydroindigo in different environments, as indicated. b) Energetics of the indigo and dehydroindigo isomerization. Gas phase and Ag(111) adsorbed states are indicated by the subscripts (g) and (a), respectively.

Next, the propensity of the indigo type dyes towards isomerization is addressed. To unravel the related thermodynamics, extensive DFT calculations were carried out comparing the energy difference between *cis* and *trans* configuration of the molecule in different environments (Figure 3.11b). As expected, in the gas phase and on the surface, *trans*-indigo is favored over *cis*-indigo for both molecules. This energy difference between the isomers decreases significantly for dehydroindigo due to the conversion of the center C=C double bond into a single bond. Moreover, for both, indigo and dehydroindigo, the surface environment decreases the energy difference between *cis* and *trans*. However, in all these cases the *trans* isomer is favored. It is only within the coordination polymers that the *cis*-dehydroindigo is clearly favored over *trans*-dehydroindigo, which indicates that for this chemistry both the Fe coordination and the surface environment are key elements.

Finally, to gain insights into the influence of the epitaxy on the isomerization, the substrate was changed to Ag(100). Unexpectedly, only CP-A arrangements were detected in the STM investigation, even if the sample of Tyrian purple and Fe is annealed up to 673 K (Figure 3.12a-e). The corresponding DFT model in Figure S6f shows that all Fe atoms are located on hollow sites and the CP periodicity matches very well the Ag(100) lattice. In comparison, for CP-A on Ag(111), every third Fe atom is on a hollow site. A CP with *trans*-monomers is energetically favored over *cis*-monomers on Ag(100) by 96 meV/monomer. Detailed analysis shows that the key factor favoring the isomerization in the CP on Ag(111) is the strain imposed by the substrate; another key factor is the stronger binding between the CP with *cis*-dehydroindigo to the substrate than the CP with *trans*-dehydroindigo on Ag(111) (see Figure 3.13). This is not true

on Ag(100). The stronger overall adsorption energy of dehydroindigo on Ag(100) is presumably also hindering the rotation required for the isomerization into the *cis* form. As a result, the isomerization is absent on this surface.

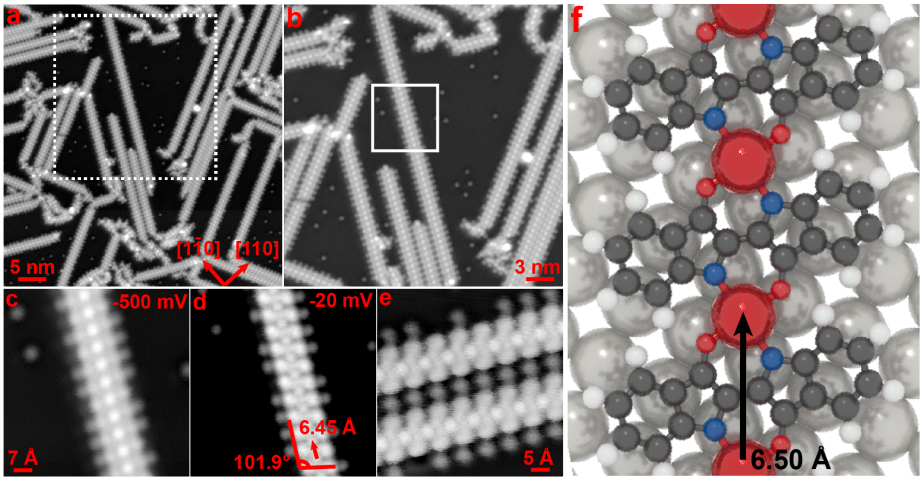

Figure 3.12: CP-A formation by Tyrian purple and Fe on Ag(100): (a)Overview STM image. (b)Zoom in of the area indicated by the dotted square in (a). (c,d) Further zoom in a single CP-A marked by the square in (b) and imaged at different sample bias. In (d), the monomer separation of 6.45 Å is marked and the angle of 101.9 ◦ indicates the orientation of the monomer with respect to the direction of the CP. f) Respective DFT optimized structural model. Annealing up to 673 K affords solely CP-A. Imaging parameters: (a-c) -500 mV, -100 pA; (d) -20 mV, -100 pA; (e) 100 mV, 1 nA. All image are acquired at 4.6 K.

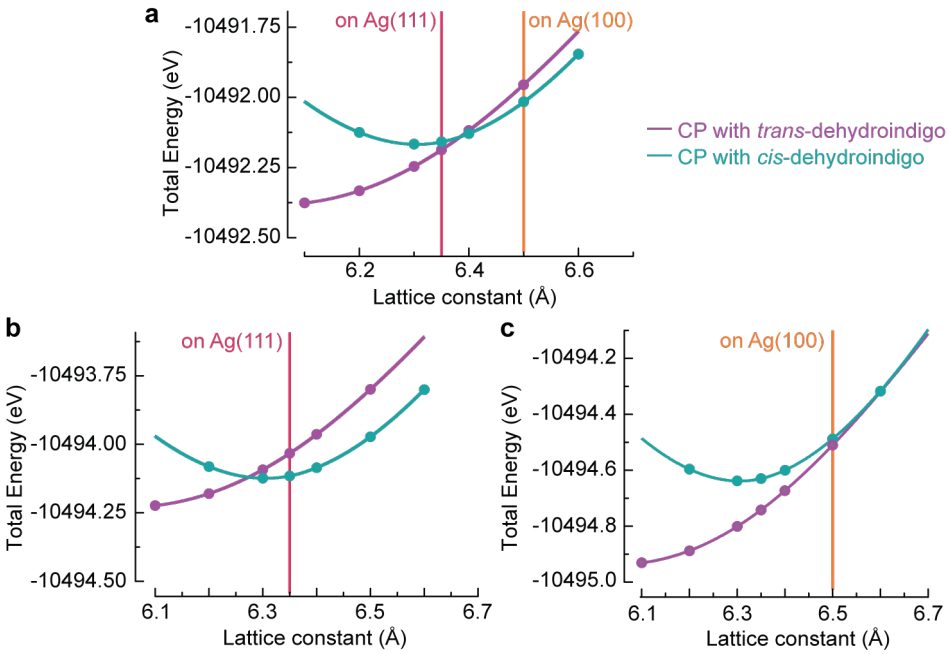

Figure 3.13: (a) The energy of a dehydroindigo-Fe monomer in a gas phase CP vs. the monomer length (lattice constant). The pink and the orange lines mark the CP monomer lengths on Ag(111) and Ag(100) respectively. This shows that given the strain of the substrate, the CP with cis-dehydroindigo (cyan data) is favored on Ag(100) (in disagreement with experiment) and the CP with trans-dehydroindigo (magenta data) is favored on Ag(111) (also in disagreement with experiment). (b-c) The energy of a dehydroindigo-Fe monomer in a gas phase CP plus the corresponding adsorption energy to the surface vs. the lattice constant can additionally take into account the effect of binding to the surface. (b) Data shifted by the adsorption energy of the monomer on Ag(111) show that CP with cis-dehydroindigo (cyan

data) is favored on Ag(111) (now in agreement with experiment). (c) Data shifted by the adsorption energy of the monomer on Ag(100) show that CP with trans-dehydroindigo (magenta data) is favored on Ag(100) (also now in agreement with experiment).

Based on DFT modeling and analysis, it is expected that the obtained CPs on Ag(111) are conductive, whereby the density of states in the vicinity of the Fermi level is quite similar for both isomers. Intriguingly, the DFT calculations indicate that on both Ag(111) and Ag(100) the CPs are spin-crossover systems, with spin-crossover energy barriers of ~100 meV. Intriguingly, the ligand field that determines the splitting between Fe d states is different in the CPs with cis-dehydroindigo and CPs with trans-dehydroindigo, which aspects and their implications will be explored further in a future publication.

Conclusion

We have demonstrated that two natural dyes (indigo and Tyrian purple) are suitable to generate high-quality, extended CPs obtained in a metal-directed assembly scenario on planar silver surfaces (see pathways described in Figure 3.1). CPs incorporating *trans*-dehydroindigo molecules and Fe adatoms are realized on Ag(111) and Ag(100). The dehydrogenation caused by the Fe-coordination, transforms the center double bond of the molecule into a single bond, enabling a rotation of the indole moieties on both surfaces. On Ag(111), the difference in the binding of *cis* and *trans* dehydroindigo isomers to the surface mediates an isomerization of the molecular linker within the CP. For this isomerization, both the Fe coordination and the presence of the Ag substrate are crucial: their combination results in an energy gain when the molecular monomer transforms from *trans* to *cis*. These results reveal the realization of interfacial metal-organic nanosystems, where different types of CPs are accessible by the linker isomerization, offering a new pathway to alter the physicochemical properties of the respective CPs. Last but not least, with the presented strategy of employing such natural dyes, biocompatibility and biodegradability may be imparted in such advanced composites.

4. From indigo to on-surface synthesis, coordination and fusion of metalated porphyrinoids on a planar gold surface

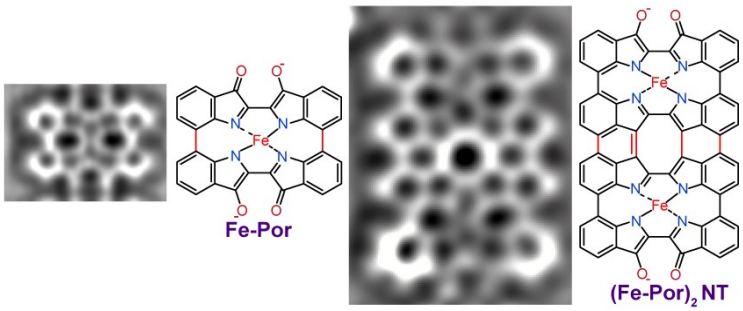

Introduction

Porphyrins,[166] consisting of four pyrrole subunits connected through a methine bridge, are highly significant functional molecules in both biological processes and material science, as they possess outstanding photophysical properties,[167] redox activity,[168] and the ability to coordinate with metal atoms.[169] In recent decades, significant efforts have been devoted to synthesizing various porphyrinoids (**Pors**)[170-173] due to their diverse conformations, cavity shapes, and π-electrons. These structural variations offer the potential for **Pors** to possess unique physical and chemical properties compared to traditional porphyrins. Among these, porphycene, which is the first constitutional isomer of porphyrin and synthesized from bipyrrole dialdehyde through McMurry coupling (Figure 4.1a)[174] is one of the most-studied **Pors** owing to its synthetic accessibility, chemical stability, and remarkable optical properties.[175]

Porphyrin nanotapes,[176] such as *β*-*β*, *meso*-*meso*, *β*-*β* triply-linked porphyrin arrays, have garnered significant attention in light of their high degree of π-conjugation. The highly π-conjugated nature of the porphyrin nanotapes gives rise to various notable characteristics, such as highly red-shifted absorption bands,[177] extraordinarily narrow HOMO-LUMO gaps,[176] near-IR reverse saturable absorption,[178] and high single-molecule conductance.[179] In addition to porphyrin nanotapes, **Pors**[180] (e.g., corrole[181-185] and subporphyrin[186]) nanotapes (**Pors NT**), porphyrin-**Pors** (e.g., porphyrin-hexaphyrin)[187-189] hybrid and porphyrin-graphene hybrid nanotapes[189-191] have been successfully explored and synthesized. However, it is worth noting that almost all synthesized porphyrin-related nanotapes to date are limited to triple connections due to the presence of only a maximum of three fused sites (*β*, *meso*, *β*) on one side of the porphyrin or **Pors** used. This indicates the absence of quadruply (or further) fused porphyrin-related nanotapes, which are highly intriguing materials because they potentially have a higher π-conjugation network and novel electronic properties. Thus, to obtain quadruply or more than quadruply fused nanotapes, it is necessary to explore novel **Pors** containing more fused sites and develop new fusion reaction methods.

In the past decade, on-surface synthesis has been proven a versatile bottom-up strategy to construct atomically defined nanostructures using rationally designed molecular precursors.[5] For example, this method has successfully synthesized various **Pors** (e.g., regular[51, 192-196] and expanded phthalocyanines),[51] triply fused porphyrin nanotapes,[197] and porphyrin-graphene hybrids nanotapes.[189, 190] Thus, on-surface synthesis holds great promise for creating novel **Pors** and quadruply (or more than quadruply) fused nanotapes. In this article, we present the on-surface synthesis of quadruply fused **Fe-Por NTs** made up of novel **Fe-Pors** using a common natural pigment (indigo) with Fe atoms on Au(111). The novel metallated **Pors**, which can be

described as porphycene derivatives, were synthesized with high yield by a series of thermally activated reaction steps, including isomerization, selective C–H activation assisted by coordination pocket template, and so on. Subsequently, deoxygenative and dehydrogenative C–C coupling were employed to fuse **Fe-Pors** into **Fe-Por NTs** (**(Fe-Por)$_2$ NT** and **(Fe-Por)$_3$ NT**), where **Por** segments are connected by quadruple linkages, forming two fused six-membered rings and one eight-membered ring. The reaction products are identified by a combination of STM, nc-STM, and density functional theory (DFT) investigations.

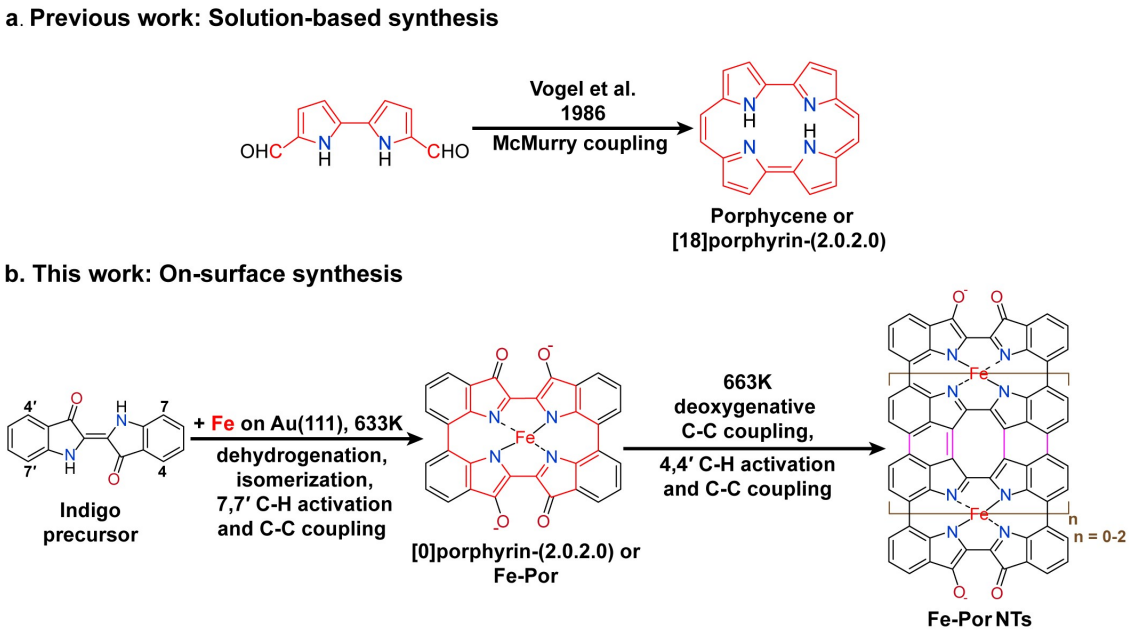

Figure 4.1: Schemes of (a) solution-based synthesis of porphycene, **Fe-Pors**, and (b) on-surface synthesis of **Fe-Por** and **Fe-Por NTs** on Au(111).

Results and Discussion

On-surface synthesis of porphyrinoids and their nanotapes

The deposition of a sub-monolayer of indigo molecules on Au(111) kept at r.t. results in linear chain-shape structures stabilized by intermolecular hydrogen bonds (NH···O=C, imino and carbonyl group: NH and C=O) (Figure 4.2a-c). Subsequent annealing to 473 K leads to the complete desorption of the molecules (evidenced by C 1s XPS in Figure 4.2d). However, a different scenario is observed once some Fe atoms are co-deposited together with the indigo molecules. In this case, even upon subsequent annealing to 573 K, indigo molecules remain adsorbed on the surface and formed chain-shape structures (Figure 4.3). Our work described in the previous chapter established that indigo molecules with Fe atoms on Ag(111) can give rise to coordination polymers (CPs) comprising of homochiral *trans*-dehydroindigo molecules (Figure 4.4a) that are generated by the deprotonation of NH group at 473 K annealing temperature. Further annealing of the sample to 573 K leads to formation of *cis*-CPs that consist of *cis*-dehydroindigo molecules (Figure 4.4b) generated by the isomerization of *trans*-dehydroindigo. Therefore, we attribute the above chain-shape structures to Fe-coordination polymers consisting of dehydroindigo molecules. The related XPS data provides further evidence for our conclusion (see Figure 4.5). The O 1s spectra show that the main peak located at E_B=530.6 eV will shift to higher E_B=531.1 eV following annealing at 573 K consistent with C=O···Fe coordination bond formation.[162] The N 1s spectra show that once Fe atoms are introduced into the indigo/Au(111) system, the main peak centered at E_B=399.5 eV will be split

off into an additional peak with weak intensity located at E_B=398.0 eV. It indicates that a part of the NH groups deprotonate and form =N···Fe coordination bonds, in good accord with the findings on Ag(111) described in the previous chapter. However, after annealing at 573 K, the weaker peak becomes the main and dominant peak (E_B=398.3 eV), implying that all NH groups have been deprotonated and form =N···Fe coordination bonds. The Fe 2p spectrum (at the bottom of Figure 4.5c) displays two peaks at E_B=707.0 and 720.0 eV, corresponding to Fe $2p_{3/2}$ and Fe $2p_{1/2}$ of metallic Fe, respectively.[198] In the Fe 2p spectrum (on top of Figure 4.5c), the Fe $2p_{3/2}$ and Fe $2p_{1/2}$ peaks are shifted to E_B=710.5 and 724.0 eV, respectively, corresponding to the positively charged Fe(II) species[199] in coordination bonds. The Fe 2p spectra are in good agreement with the evolutions of N 1s and O 1s, demonstrating the formation of Fe···O coordinative bonds.

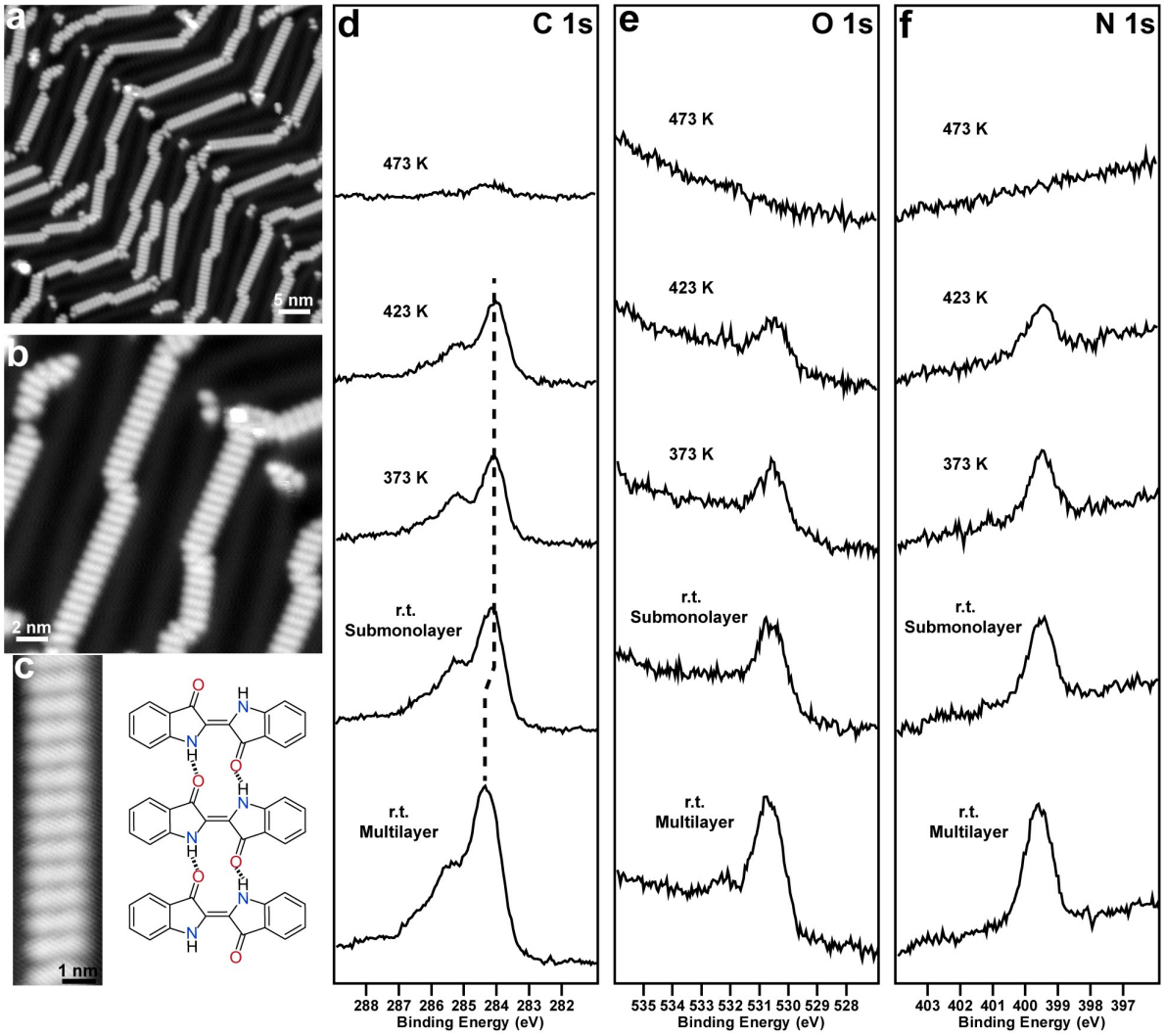

Figure 4.2: Indigo on Au(111) without Fe atoms. (a) An overview STM image of chain-like self-assemblies of indigo. (b) Zoom-in STM image of the chain-like self-assemblies. (c) High-resolution STM image of a chain-like self-assembly and its chemical structure model. The straight chain-like structure is stabilized by intermolecular hydrogen bonded. (d-f) Core level spectra of C 1s, O 1s, and N 1s for the indigo adsorbed on Au(111) at r.t. followed by subsequent annealing to 373 K, 423 K, and 473 K, respectively. Scan parameters: (a-b) V_s = -1 V, I_t = 100 pA; (c) V_s = 100 mV, I_t = 100 pA. All STM images were acquired at 4.6 K.

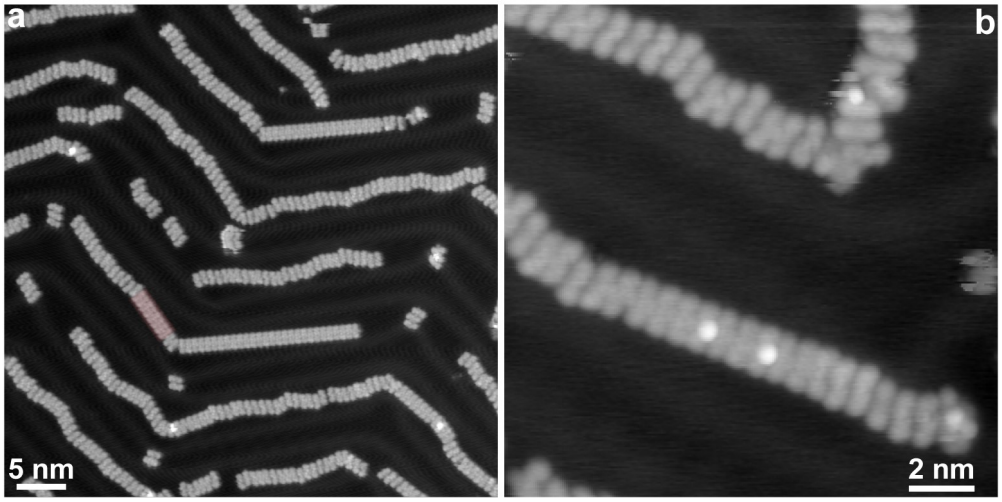

Figure 4.3: CPs on Au(111) forming after annealing indigo with Fe adatoms at 573 K. (a) Overview STM image of CPs. (b) Zoom-in STM image of CPs. Scan parameters: (a) V_s = -300 mV, I_t = 100 pA; (b) V_s = -100 mV, I_t = 10 pA. All STM images were acquired at 4.6 K.

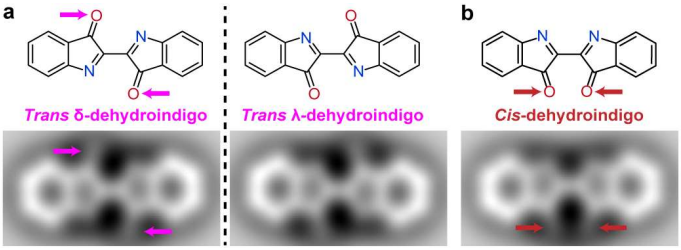

Figure 4.4: Chemical structures and nc-AFM simulation images of *trans*-dehydroindigo and *cis*-dehydroindigo.

To characterize the configuration of each molecule and determine whether dehydroindigo undergoes isomerization on Au(111), similar to the isomerization on Ag(111), we performed nc-AFM experiments using a CO-functionalized tip. The nc-AFM image (Figure 4.6b and its corresponding STM image in Figure 4.6a) reveals two distinct molecular configurations, indicated by the magenta and red brackets, respectively. Two rod-shaped protrusions (indicated by the red arrow) are observed on the same side of a single molecule in the configuration marked by a red bracket. However, in the magenta-marked configuration, the two protrusions are observed on both sides of a single molecule. The nc-AFM simulation results (Figure 4.4) provide insights into the assignment of the C=O group of dehydroindigo as rod-shape protrusion[200] in AFM measurements. It is observed that the protrusions in *trans*-dehydroindigo or *cis*-dehydroindigo are located on both sides or the same side of the single molecule, respectively. Furthermore, the surface chirality of dehydroindigo, induced by the adsorption of the molecule on the surface, which leads to mirror symmetry breaking, can also be identified by the distribution of the protrusion (C=O group) (Figure 4.4a). These observations are consistent with our previous results, allowing us to confidently attribute the observed two different configurations to *trans*- and *cis*-dehydroindigo and propose chemical structure of the Fe-coordination polymer (Figure 4.6c).

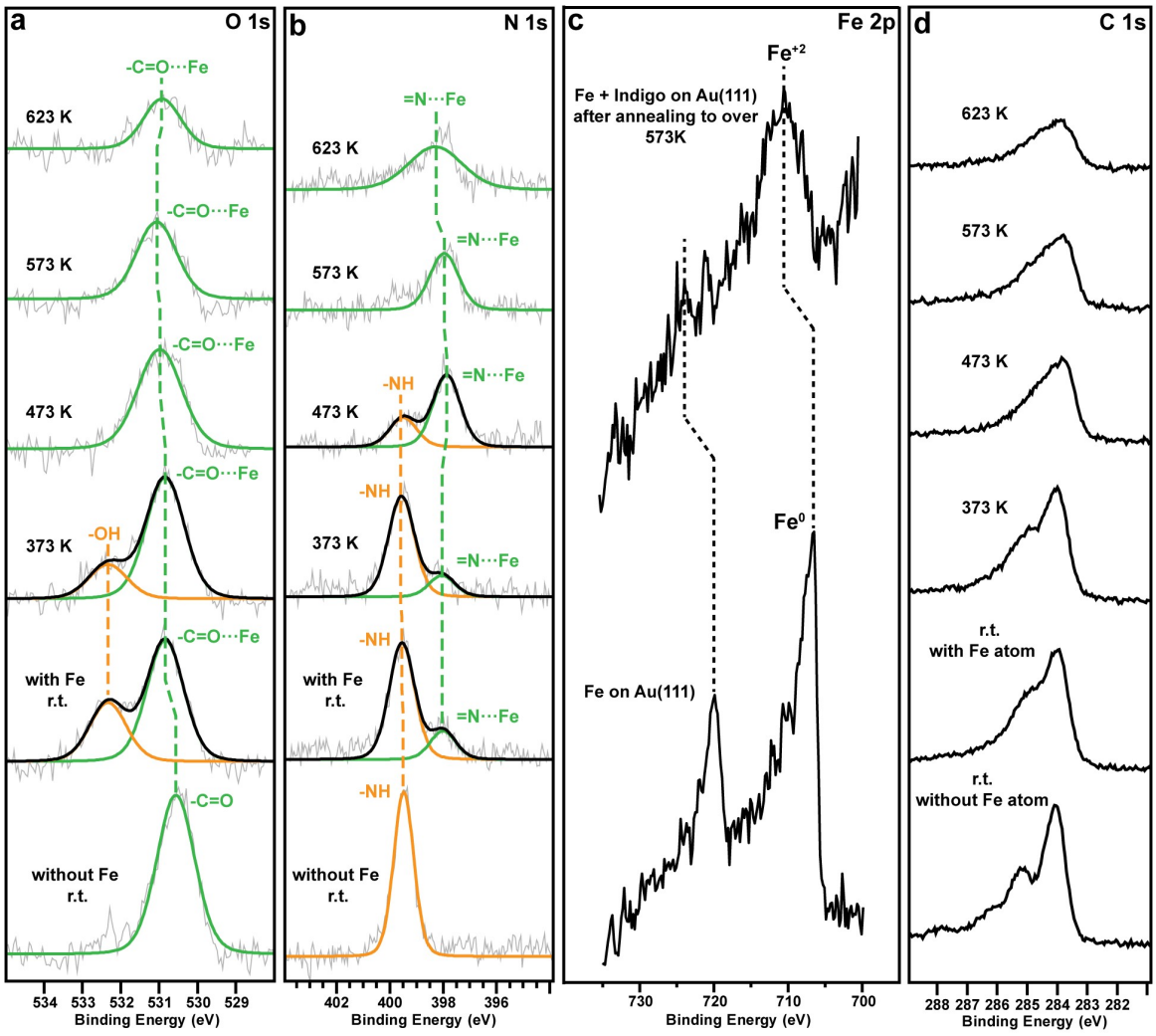

Figure 4.5: Core level spectra of O 1s, N 1s, Fe 2p, and C 1s for the indigo without Fe atoms at r.t. and indigo with Fe atoms at r.t. followed by subsequent annealing to 373 K, 473 K, 573 K, and 623 K, respectively.

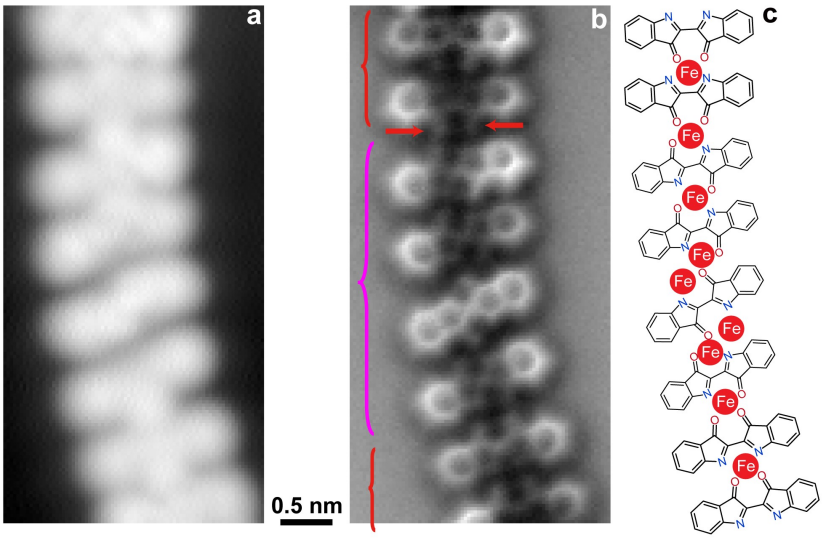

Figure 4.6: Identification of dehydroindigo molecular configurations. (a-b) Constant-current STM and constant-height nc-AFM image of the coordination polymer consisting of *trans*-dehydroindigo and *cis*-dehydroindigo, respectively. (c) Chemical structure for the coordination polymer in (a). Scan parameters:

(a) V_s = -50 mV, I_t = 50 pA; (b) V_s = 0 mV, constant height. All STM and nc-AFM images were acquired at 4.6 K.

Upon annealing the sample to 633 K, new coordination polymers (Figure 4.7a-b and Figure 4.8a) prevailed in the surface. These were composed of rectangular monomers with a bright protrusion at its center, such as the one exemplarily presented in Figure 4.7c or marked by cyan outline in Figure 4.8a. Interestingly, the width of this rectangular structure is larger than that of a single indigo molecule, indicating that it is composed of more than one indigo unit. The nc-AFM images of the rectangular products (Figure 4.7d, Figure 4.8b) reveal that it consists of a macrocycle skeleton formed by two *cis*-dehydroindigo molecules connected by two new C–C bonds, as shown in the proposed molecular structure in Figure 4.7f or 4.8c (new C–C bonds in red). Notably, the central region of the rectangular structure appears as a bright protrusion in STM measurements but as a distorted cross of low contrast in nc-AFM measurements, in line with images of Fe in the coordination environment of a phthalocyanine[201, 202] and in the coordination environment of a porphyrin[203]. We, therefore, attribute these features to Fe atoms within a tetrapyrrole pocket and assign the rectangular product as the **Fe-Por**. We note that the atomic model derived from the nc-AFM can be described by various resonance chemical structures (e.g. Figure 4.7f), however for the purposes of simplicity in the discussion that follows we will adopt the one featuring in Figure 4.7f, with the Fe single atom in a similar coordination environment as in a porphyrin, which is also consistent with the XPS data of the Fe 2p core level.

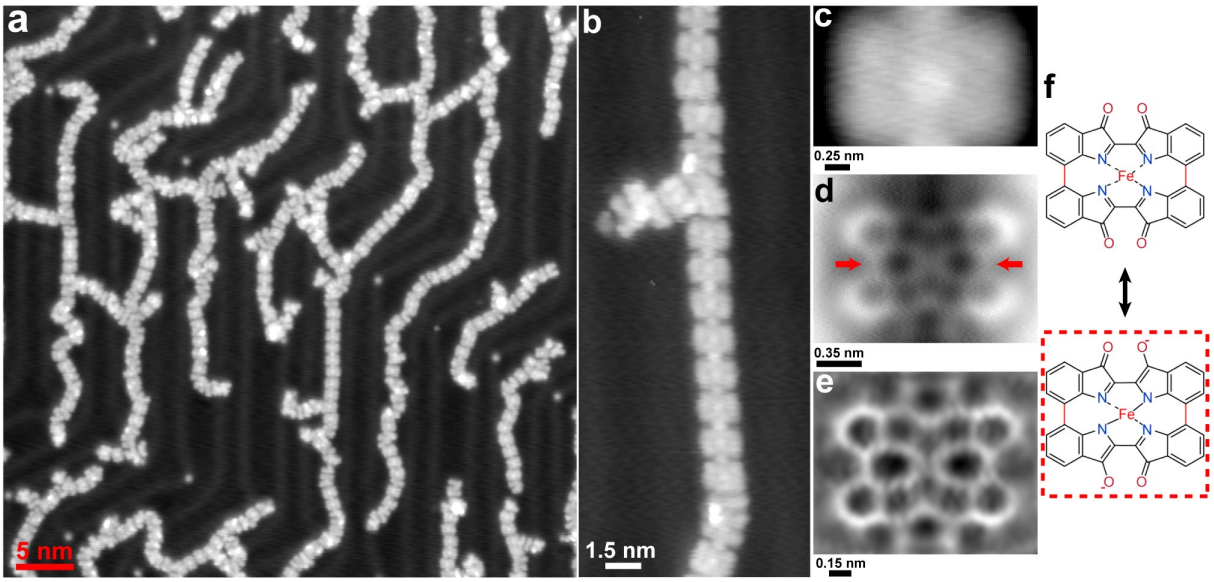

Figure 4.7: (a) Large-scale STM image after annealing indigo with Fe atoms at 633 K. (b) New CP consisting of **Fe-Pors**. (c-e) High-resolution STM, high-resolution nc-AFM image, and Laplace filtered image of the **Fe-Por**, respectively. The red arrows indicate new C–C bonds. (f) Two resonance chemical structures of **Fe-Por**. Scan parameters: (a, c) V_s = -50 mV, I_t = 10 pA; (b) V_s = -100 mV, I_t = 100 pA; (d) Constant height, V_s = -2 mV. All STM and nc-AFM images were acquired at 4.6 K.

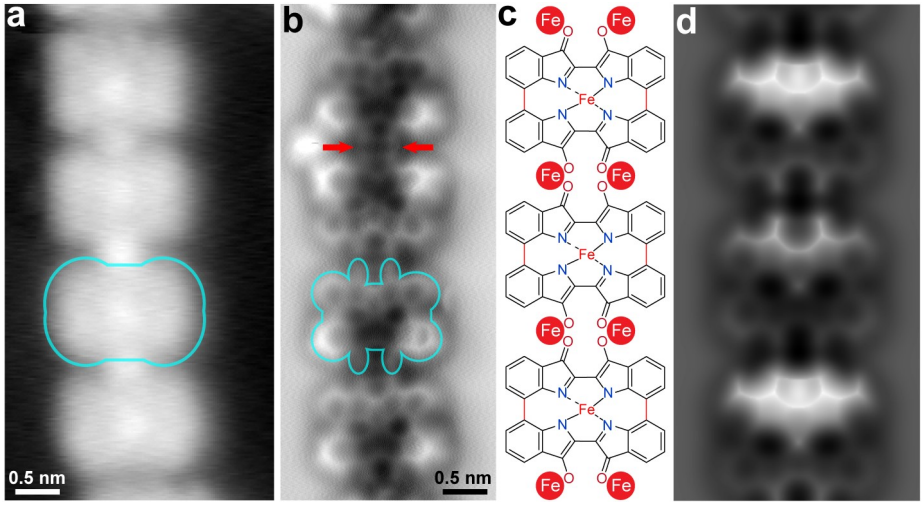

Figure 4.8: On-surface synthesis of **Fe-Pors**. (a) STM image of coordination polymer consisting of **Fe-Pors** after annealing the sample at 633 K. (b) Corresponding constant-height nc-AFM image. (c-d) Chemical structure and nc-AFM simulation of the coordination polymer, respectively. Scan parameters: V_s = -50 mV, I_t = 10 pA (a-b); V_s = -2 mV, constant height (c). All STM and nc-AFM images were acquired at 4.6 K.

The tetrapyrrole core of **Fe-Por** is structurally similar to porphycene (highlighted by red color in Figure 4.1), a porphyrin isomer. Porphycene (Figure 4.1a) possesses 18π electrons in its shortest conjugation pathway and thus is denoted as [18]porphyrin-(2.0.2.0) according to nomenclature. However, the synthesized **Fe-Por** has no aromaticity due to the absence of a complete conjugation pathway. Consequently, its nomenclature is [0]porphyrin-(2.0.2.0). The outer parts of two peripheral benzene moieties located along the longer **Fe-Por** dimension exhibit a brighter appearance, indicating that they tilt out of the surface plane and the **Fe-Por** possesses a part with a concave shape (Figure 4.7d and Figure 4.8b).

The STM images of the metal nodes of these CPs (Figure 4.7b and Figure 4.8a) present a single bright protrusion between two adjacent **Fe-Pors** that resembles the center region of **Fe-Pors**. In the corresponding nc-AFM image (Figure 4.8b), the carbonyl groups between two adjacent **Fe-Pors** are found to be facing each other (indicated by red arrows), instead of a cross feature. A model in which two Fe atoms exist between two adjacent **Pors** (Figure 4.8c) was found to reproduce well the experimental data (Figure 4.8d), unlike a model with a node of a single Fe atom. Defect nodes are also present (Figure 4.9a, b, f and h) and will be discussed below.

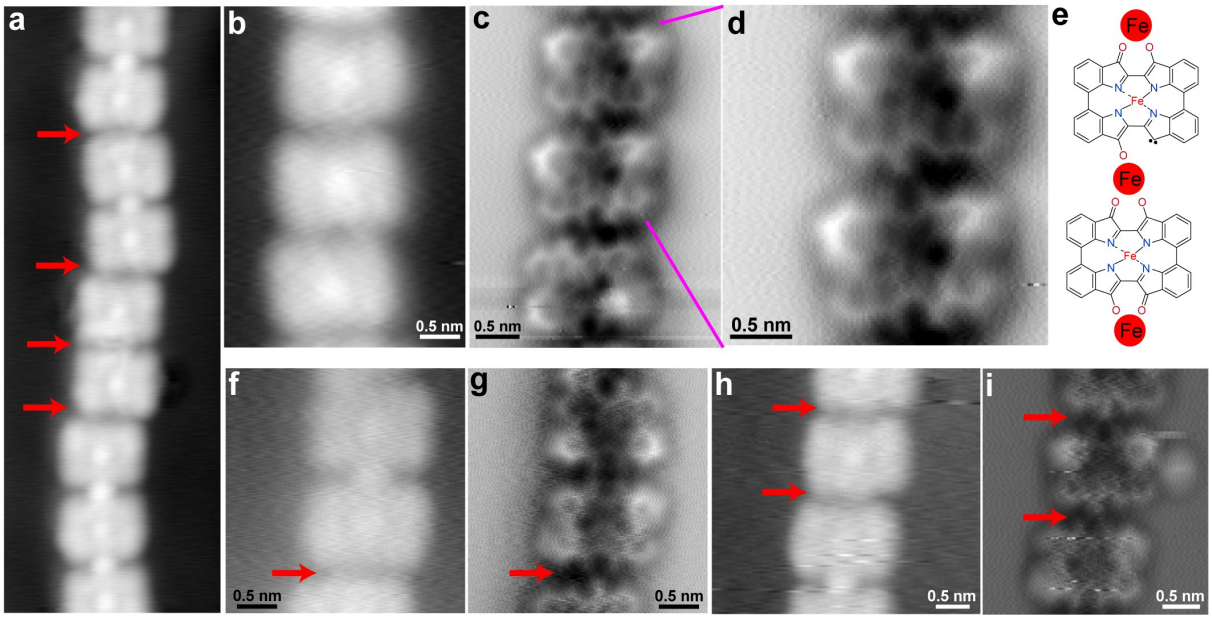

Figure 4.9: (a, b, f, h) High-resolution STM image of the new CPs containing of dark nodes. (c, d, g, i) High-resolution nc-AFM images of the new CPs presented in (b), (b), (g), and (i), respectively. (e) A possible model for the dark node. Scan parameters: (a) V_s = -30 mV, I_t = 10 pA; (b) V_s = -50 mV, I_t = 10 pA (f) V_s = -20 mV, I_t = 10 pA; (h) V_s = -10 mV, I_t = 10 pA; (c, d, g, i) Constant height, V_s = -2 mV. All STM and nc-AFM images were acquired at 4.6 K.

The synthesis of a novel molecular species was apparent in the STM images as a structure with two bright protrusions upon further annealing of the sample to 663 K (Figure 4.10b). We attribute the bright protrusion to the presence of a Fe atom, as discussed for **Fe-Por**. Therefore, this product could be a dimer (**(Fe-Por)$_2$ NT**) resulting from the fusion of two **Fe-Por** molecules. The related experimental nc-AFM images unambiguously prove our assignment (Figure 4.10c). The central part of the **(Fe-Por)$_2$ NT** appears remarkably flat (Figure 4.10c) and exhibits a contracted eight-membered ring (Figure 4.12). Two **Fe-Pors** fuse into a **(Fe-Por)$_2$ NT**, in which the **Fe-Por** segments are connected by quadruple linkages to form two fused six- and one eight-membered rings (Figure 4.10d). Co-existing in the same surface, a longer nanotape, **(Fe-Por)$_3$ NT**, (Figure 4.11) could be identified along with other interesting side reaction products (Figure 4.13). The side products **P3**-**P6** are **Fe-Pors** derivatives. **P3** consists the two **Fe-Pors**, connected by a *trans* δ-dehydroindigo via deoxygenative and dehydrogenative C–C coupling. The **P4** could be an intermediate (or incomplete reaction) product in the formation of **(Fe-Por)$_3$ NT**. The **P5** containing an eight-membered ring is formed by deoxygenative and dehydrogenative C–C coupling between the **Fe-Pors** and a *cis*-dehydroindigo. The **P6** is the **(Fe-Por)$_2$ NT** with a defect of three missing carbon atoms. It is worth noting that these different side products are due to the variety of reactants that include *trans* δ-, λ- and *cis*-dehydroindigo.

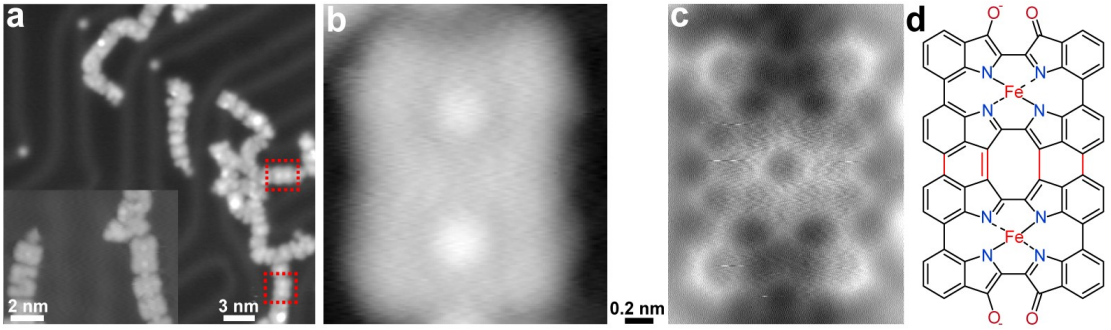

Figure 4.10: On-surface synthesis of **(Fe-Por)$_2$ NT**. (a-d) Large-scale STM, High resolution STM, nc-AFM image, and chemical structure of single **(Fe-Por)$_2$ NT** after annealing the sample at 663 K. can parameters: Measurement parameters: (a) V_s = -100 mV, I_t = 100 pA; (b) V_s = -20 mV, I_t = 10 pA; (c) V_s = -2 mV, constant height. All STM and nc-AFM images were acquired at 4.6 K.

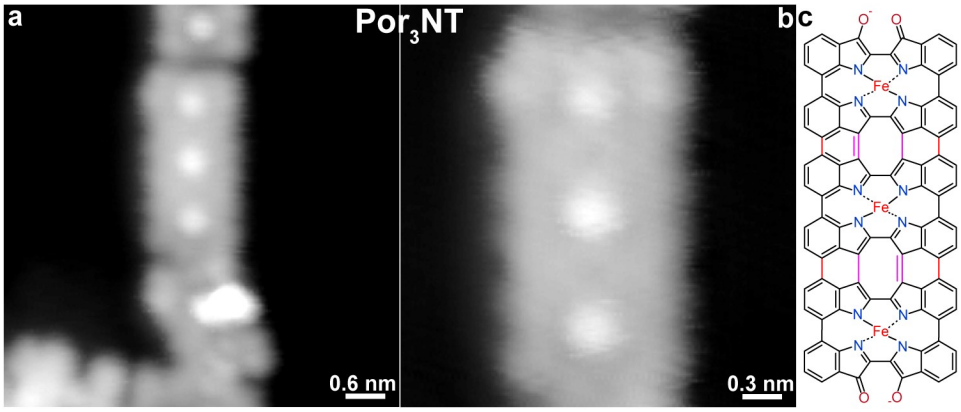

Figure 4.11: (a-b) STM image of **(Fe-Por)$_3$ NT**. (c) Chemical structure of **(Fe-Por)$_3$ NT**. Scan parameters: (a) V_s = -200 mV, I_t = 100 pA (b) V_s = -133 mV, I_t = 100 pA. All STM images were acquired at 4.6 K.

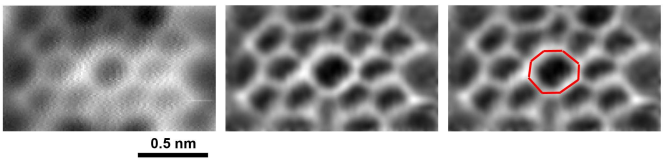

Figure 4.12: High-resolution of nc-AFM image and its Laplace filtered image of center area of **(Fe-Por)$_2$ NT**. Scan parameters: Constant height, V_s = -2 mV. All nc-AFM images were acquired at 4.6 K.

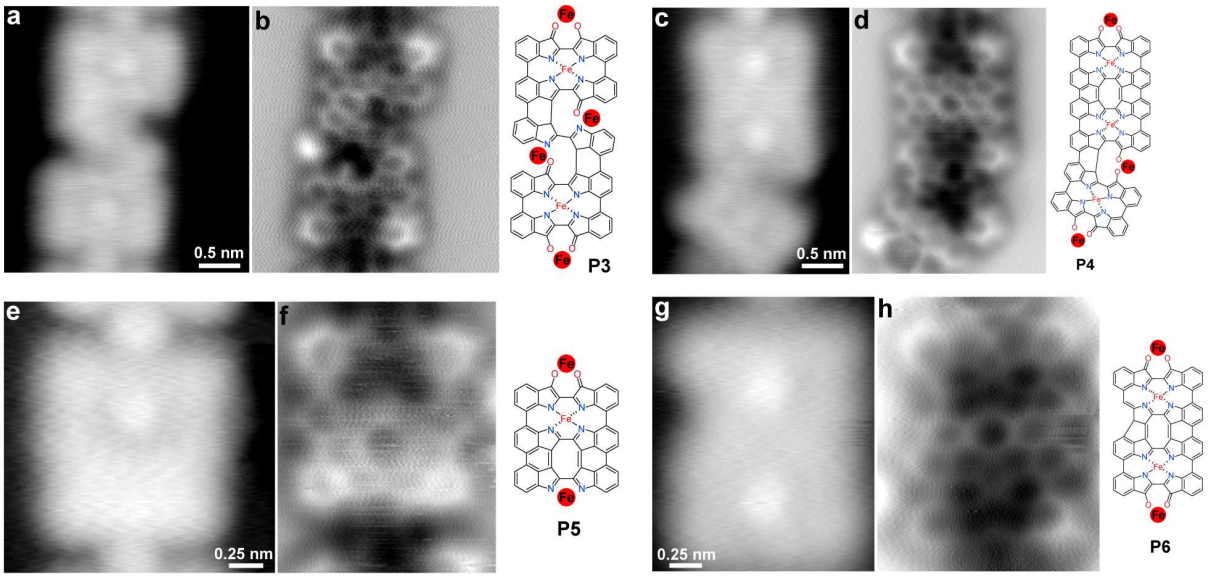

Figure 4.13: STM and nc-AFM images of side products. Scan parameters: (a) V_s = 30 mV, I_t = 10 pA; (c) V_s = -10 mV, I_t = 10 pA (e, g) V_s = -20 mV, I_t = 10 pA; (b, d, f, h) Constant height, V_s = -2 mV. All STM images were acquired at 4.6 K.

Proposed mechanism for Fe-Por and (Fe-Por)$_2$ NT

Based on our experimental observations, the following synthesis scheme of **Fe-Por** is proposed (Figure 4.14). Firstly, the NH groups dehydrogenate due to their coordination with Fe atoms,

resulting in the formation of *trans*-dehydroindigo. Subsequently, *trans*-dehydroindigo thermally isomerizes into *cis*-dehydroindigo. Lastly, dehydrogenative C–C coupling occurs by 7,7′ C–H activation of two opposite *cis*-dehydroindigo molecules, joined by an *N,N-N,N* chelating pocket, leading to the closure of the chelating pocket and the formation of the macrocyclic **Fe-Por**. The *N,N-N,N* chelating pocket has already been shown to provide a pathway of the dehydrogenative on-surface C–C coupling process, albeit demonstrating different regioselectivity.[52] Here it serves as a template that aligns the two *cis*-dehydroindigo molecules in a suitable spatial orientation for 7,7′ C–H activation (adjacent to the *N,N-N,N* chelating pocket) and subsequent C–C coupling, presumably similar to Ni template synthesis in solution chemistry.[50] The C–H activation is expected to be either surface-assisted or mediated by the native Au adatoms of the surface.[52]

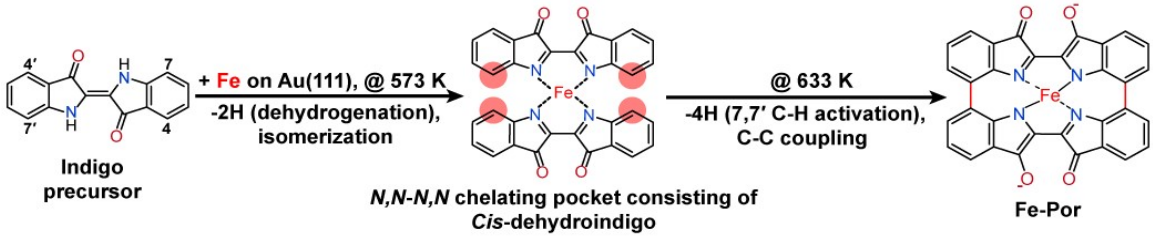

Figure 4.14: Proposed reaction pathway of synthesis of **Fe-Por.**

The synthesis of **(Fe-Por)$_2$ NT** involves both deoxygenative C–C coupling and a dehydrogenative (4,4′ C–H activation) C–C coupling (Figure 4.15). The aforementioned defect nodes of the **Por** coordination nodes are posed to be crucial intermediates for the **(Fe-Por)$_2$ NT** fusion. High-resolution nc-AFM images of these defect nodes (Figure 4.9d, g, and i) consistently reveal only three C=O groups pointing at the same point. Given the **(Fe-Por)$_2$ NT** observed, it is plausible to attribute these nodes to three carbonyl croup with a single Fe atom between them (Figure 4.9e), whereas the missing carbonyl signature would result from a removal of an O atom as part of the deoxygenative C–C coupling. The C–C coupling involving the 4,4′ C–H activation is presumably a surface-assisted intramolecular cyclodehydrogenation, commonly observed in the periphery of porphyrin molecules.[204] We find that the yield of **(Fe-Por)$_2$ NT** is lower than that of **Fe-Por**, and the yield of **(Fe-Por)$_3$ NT** is lower than that of **Por$_2$ NT**. These are attributed to the energetic barrier associated with the dissociation of the C=O double bond which is higher than the energetic barrier associated with the dissociation of the C–H single bond. Notably, the formation of **(Fe-Por)$_2$ NT** with a contracted eight-membered ring requires the dissociation of four C=O double bonds, indicating more demanding reaction conditions. Therefore, we propose that the *O,O-O,O* coordination pocket also acts as a directed template that facilitates both deoxygenation of the C=O group and the 4,4′ C-H activation. Previous work[205] has reported the synthesis of graphene-like nanoribbons consisting of eight-membered rings through the assistance of a gold-organic hybrid intermediate product (*C,C-C,C* chelating pocket). Additionally, the process of 7,7′ C-H activation and C–C coupling occurs at an annealing temperature of 633 K, which is lower than the temperature required for deoxygenative C–C coupling (663 K). This suggests that 7,7′ C-H activation and deoxygenative C–C coupling follow a hierarchical reaction pathway and do not compete with each other.

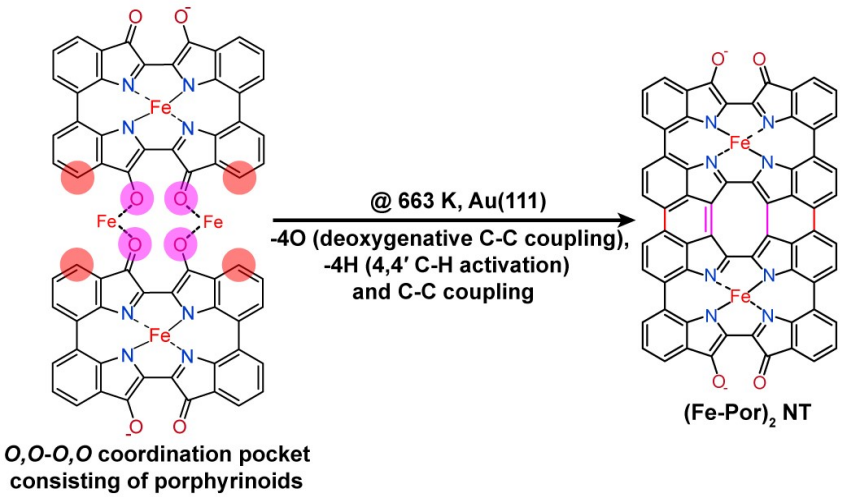

Figure 4.15: Proposed reaction pathway of synthesis of **(Fe-Por)$_2$ NT**.

Finally, it is important to highlight the role of Fe in the synthesis of both **Fe-Pors** and **Fe-Por NTs**. By XPS investigations we find that in the absence of Fe atoms, indigo molecules on Au(111) desorb after annealing at 473 K. However, indigo molecules remain on the surface following annealing temperatures of up to 673 K in the presence of Fe atoms, presumably due to the higher binding energy of the Fe-indigo CPs. This binding is essential in order for the related C–H activation. The Fe atoms also induce the deprotoisomerization of indigo, leading to the formation of *cis*-dehydroindigo, which serves as an essential precursor for the synthesis of **Fe-Pors**. Thirdly, Fe atoms participate in the formation of *N,N-N,N* coordination pockets possessing the directed-template properties. These pockets play a critical role in the spatial orientation of the reactant molecules, facilitating regiospecificity in the reactions. Finally, Fe atoms likely act as catalysts for the deoxygenative C–C coupling, essential steps in the synthesis of **Fe-Por NTs**. Notable, substituting Fe with holmium (Ho) atoms results in substantially different regioselectivity of C–C coupling around the coordination pocket and consequently different reaction products (only *trans*-dehydroindigo CPs) (Figure 4.16). Presumably, the isomerization of *trans*-dehydroindigo into *cis*-dehydroindigo is not favoured in the case of Ho, preventing the subsequent formation of **Por**.

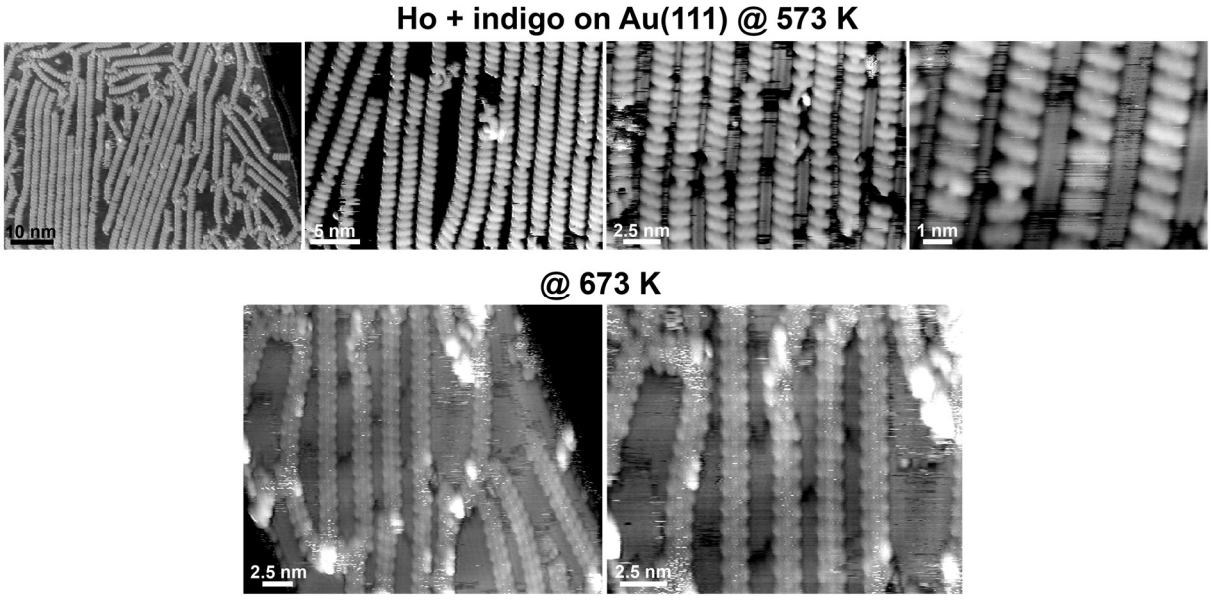

Figure 4.16: STM images of *trans* Ho-CPs. Scan parameters: V_s = -1.2 V, I_t = 60 pA. All STM images were acquired at room temperature.

In summary, Fe plays a multifaceted role in the synthesizing **Fe-Pors** and **Fe-Por NTs**, including stabilizing indigo molecules, inducing important chemical transformations, facilitating directed-template effects, and acting as a catalyst for specific coupling reactions. The reactivity and size of the metal atom are critical factors that influence the success of the synthesis process.

Electronic properties of Por, (Fe-Por)$_2$ NT, and (Fe-Por)$_3$ NT.

We next investigated the electronic structure of the **Por**, **(Fe-Por)$_2$ NT**, and **(Fe-Por)$_3$ NT** through differential conductance (dI/dV) measurements using STS. In Figure 4.17, STS measurements on a single dehydroindigo and **Fe-Por** are presented. The absence of peaks within the bias range from -2 V to 2 V indicates that the highest occupied molecular orbital (HOMO) and lowest unoccupied molecular orbital (LUMO) of single dehydroindigo and **Fe-Por** are outside this range. Figure 4.18a displays characteristic local dI/dV spectra collected at the center (depicted in orange), upper-Fe position (shown in red), and the upper-right position (represented in dark cyan) of the **(Fe-Por)$_2$ NT**, along with the reference spectrum recorded on bare Au(111) (illustrated in bright blue). At all points, peaks below the Fermi level are observed at -1.23 V, -0.38 V, and -0.02 V, labeled as 1-3, respectively. Additionally, two peaks above the Fermi level are observed at 0.3 V and 1.22 V, labeled as 4-5. The dI/dV maps for these biases are presented in Figure 4.18b. The dI/dV maps labeled 1-3 in Figure 4.18b reveal that the two Fe atoms within the **(Fe-Por)$_2$ NT** appear as bright features. It is worth noting that the peak labeled 2 coincides with the surface state of Au(111). The dI/dV map labeled 5 at 1.22 V shows a "H" shape-like feature, possibly indicating the π-conjugated backbone of **(Fe-Por)$_2$ NT**. Notably, the two Fe atoms in **(Fe-Por)$_2$ NT** are invisible at this bias. Interestingly, the dI/dV map labeled 4 at 0.3 V not only displays a feature of the π-conjugated backbone of **(Fe-Por)$_2$ NT** but also of the Fe atom, suggesting that this may be a mixed state. It is important to note that, based on the available data, it is challenging to definitively identify which peaks correspond to the HOMO and LUMO of **(Fe-Por)$_2$ NT**. To gain a clearer understanding of these peaks, further assistance from DFT calculations is required. Figure 4.19a presents characteristic dI/dV spectra collected at the center-Fe position (depicted in red), upper-middle position (shown in orange), and the upper-left position (represented in dark cyan) of the **(Fe-Por)$_3$ NT**, along with the reference spectrum recorded on bare Au(111) (illustrated in bright blue). Two peaks are observed at -0.1 V and 0.79 V, respectively. The corresponding dI/dV maps are shown in Figure 4.19b. The dI/dV maps labeled 1 in Figure 4.19b reveal that the three Fe atoms within the **(Fe-Por)$_3$ NT** also appear as bright features. The dI/dV map at 0.79 V displays a ladder-shaped feature. These two dI/dV maps are consistent with the dI/dV maps of **(Fe-Por)$_3$ NT** located at -0.38 V and 0.3 V. However, it is also challenging to determine definitively whether these correspond to the HOMO or LUMO of **(Fe-Por)$_3$ NT**.

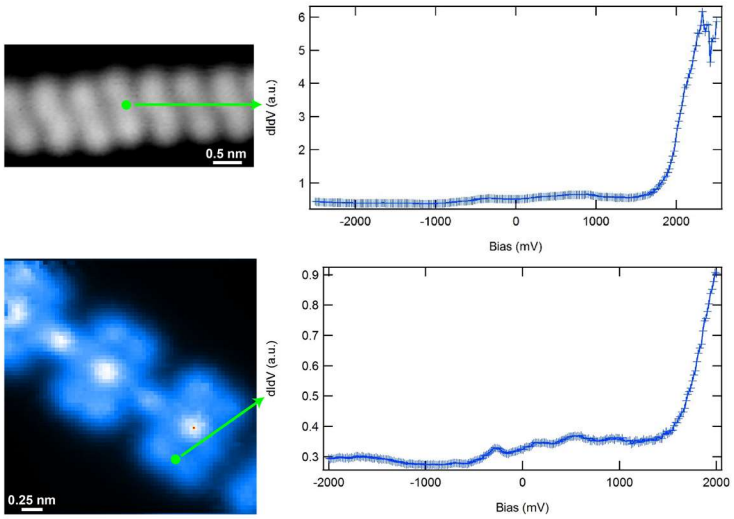

Figure 4.17: Characteristic dI/dV spectra of single dehydroindigo and **Fe-Por** acquired at the positions shown in the inset STM image (colored dots). Scan parameters: V_s = -100 mV, I_t = 100 pA. All STM images were acquired at 4.6 K.

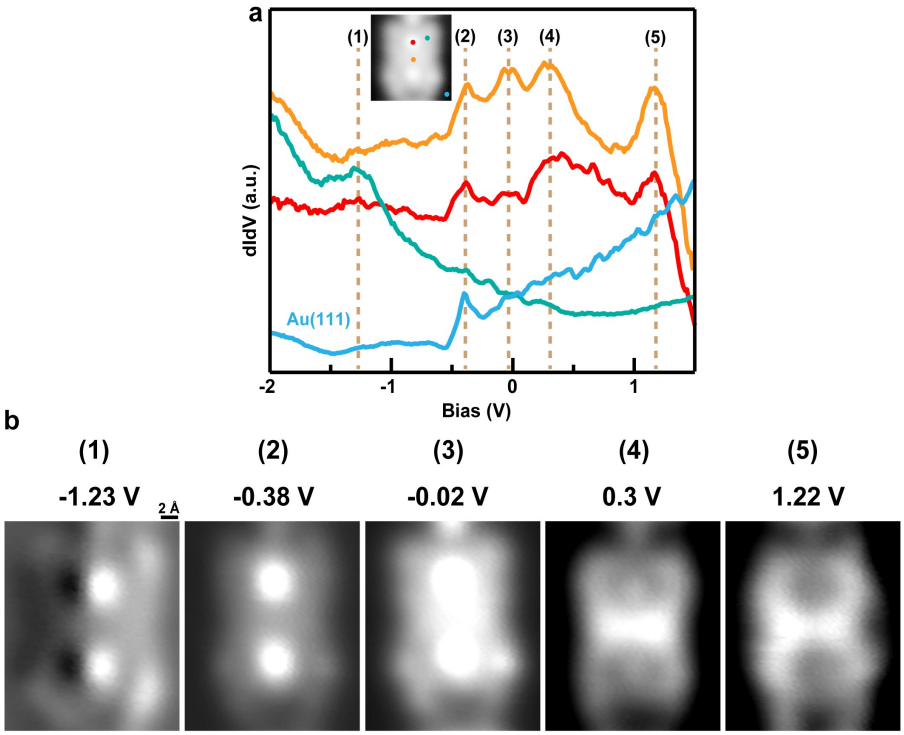

Figure 4.18: Electronic structure of the **(Fe-Por)$_2$ NT**. (a) Characteristic dI/dV spectra acquired at the positions shown in the inset STM image (coloured dots). (b) Experimental dI/dV maps in constant-height mode. Scan parameters: (a) V_s = 100 mV, I_t = 100 pA. All STM images were acquired at 4.6 K.

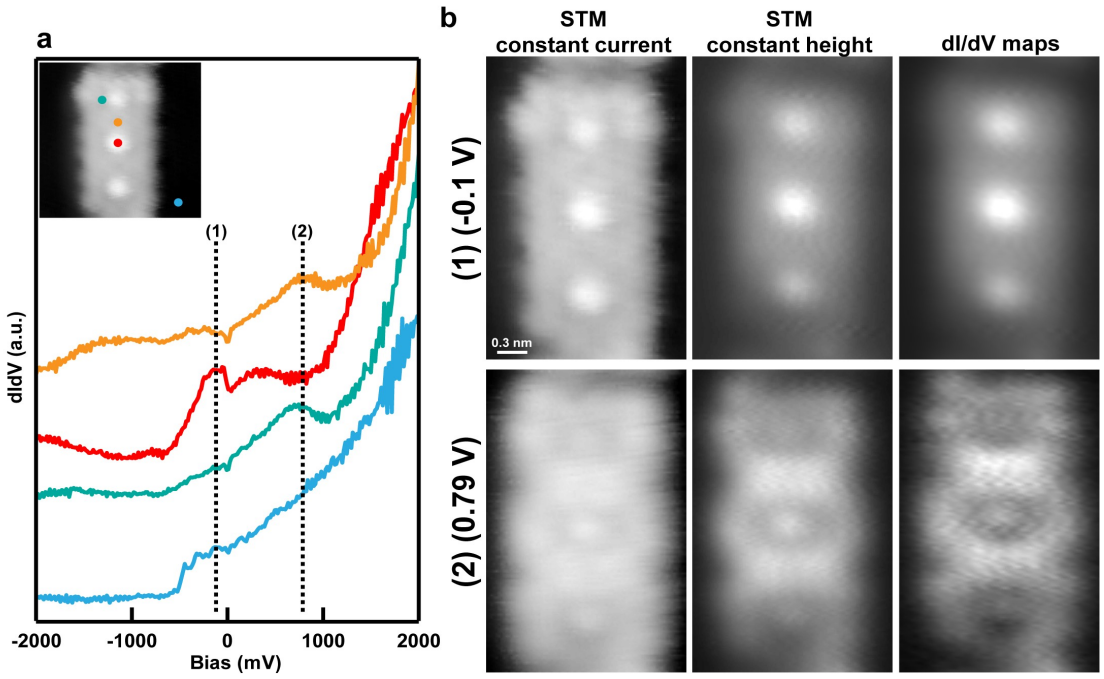

Figure 4.19: Electronic structure of the **(Fe-Por)$_3$ NT**. (a) Characteristic dI/dV spectra acquired at the positions shown in the inset STM image (coloured dots). (b) Experimental dI/dV maps in constant-height mode. (a) V_s = 100 mV, I_t = 100 pA. All STM images were acquired at 4.6 K.

Conclusion

We have achieved the successful on-surface synthesis of novel indigo-based **Fe-Pors** and their quadruply fused nanotapes. The **Fe-Pors**, akin to porphycene derivatives, are synthesized with high yield through a series of thermally activated reaction steps. These steps include isomerization, selective C–H activation facilitated by a coordination pocket template, and more. Subsequently, deoxygenative and dehydrogenative C–C coupling are employed to fuse the **Fe-pors** into **Fe-Por NTs**, specifically **(Fe-Por)$_2$ NT** and **(Fe-Por)$_3$ NT**. These nanotapes feature **Por** segments connected by quadruple linkages, forming two fused six-membered rings and one eight-membered ring. Our research contributes to the advancement of on-surface and solution synthesis methodologies for macrocyclic tetrapyrroles and quadruply fused **Fe-Por NTs**, thereby expanding the available chemistry in this domain. Additionally, these findings open avenues for the fabrication of novel nanostructures with unique properties.

5. Planar π-extended cycloparaphenylenes with an all-armchair inner edge

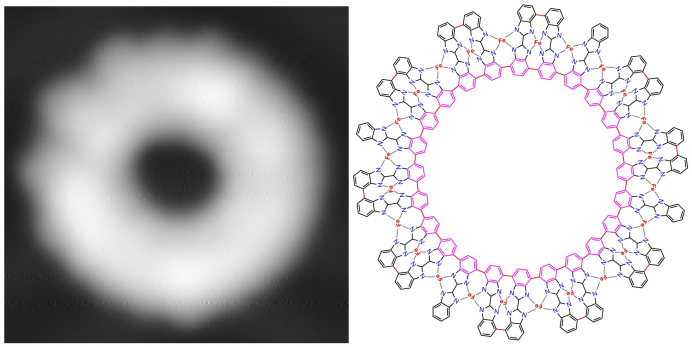

Introduction

Cyclic polymers, not containing end groups, demonstrate a number of unique physical and chemical properties. For instance, the density, refractive index, glass-transition temperature, viscoelasticity, reptation, and surface properties of cyclic polymers exhibit notable distinctions when compared to their more conventional linear counterparts.[206] For example, a recent study found that toroid supramolecular polymers exhibit very different luminescence in comparison to their coil counterparts.[207] Importantly, the unique properties arising from their cyclic topology make ring polymers promising candidates for various emerging applications, such as drug delivery, surface modification, and hierarchical assembly.[208] In the past half-century, polymer chemists have dedicated considerable efforts to the synthesis of cyclic polymers, exploring a variety of effective strategies such as ring-closure,[206] ring-expansion, vernier templating, and self-assembly.[208]

The [*n*]cycloparaphenylenes ([*n*]CPPs) - often referred to as carbon nanohoops - are a distinct type of cyclic polymer, composed of *n* benzene rings linked at the *para* positions end-to-end.[209] Following the pioneering synthesis of a cyclic oligophenylene in 2008 by Jasti and colleagues,[210] there has been a growing surge of interest in molecules of this kind, with the synthesis of many different sizes of CPPs.[211-214] In addition, some π-extended nanohoops have been synthesized.[215-218] To tune the structural or optoelectronic properties of the nanohoops beyond the size-dependent effect known for CPPs, a variety of aromatic rings other than benzene were introduced (eg, tetra-benzothiadiazole-based [12]CPP).[219] Planarized CPP macrocycles are fascinating due to their unique properties such as all-armchair edge topology, exclusive global aromaticity, and ring currents. Furthermore, *para*-connected phenylenes exhibit delocalized π-electrons along the carbon backbone, characterized by highly dispersed bands, a reduced bandgap, and enhanced conductance compared to *meta*-conjugated phenyl rings.[220] However, planar CPP macrocycles are challenging to synthesize using traditional solution chemistry due to the significant strain present in the CPPs. Moreover, it has been demonstrated that the interaction with the surface resulting from the adsorption of CPPs onto a metal surface are insufficient to overcome the planarization energy.[221, 222] Over the past few decades, on-surface synthesis[2, 5] has emerged as an alternative bottom-up approach for constructing atomically well-defined carbon-based nanostructures that cannot be accessed through traditional solution chemistry, such as cyclo[18]carbon,[8] cyclo[16]carbon,[223] triangulene,[224] biphenylene network,[225] disilabenzene-bridged covalent organic framework[226] and planar π-extended [12]CPP.[227] Among them, the planar π-extended [12]CPP with an all-armchair periphery has been first successfully synthesized by Xiang and her colleagues through

tactfully using a meticulously designed precursor that templates the appropriate curvature of the paraphenylene backbone while maintaining the molecular orbitals upon π-extension.[227] However, apart from this case, there have been scarce reports on the synthesis of the planar (or π-extended) CPPs.

In this work, we report on the successful on-surface synthesis of different sized, planarized and π-extended CPPs as well as other types of cyclic polymers using a linear precursor molecule and utilizing on-surface intermolecular dehydrogenative C–C coupling. Specifically, we first fabricated coordination polymers comprising a coordination pocket node (Figure 5.1b) through annealing 1H,1'H-2,2'-bibenzo[d]imidazole (H_2bbim, Figure 5.1a) molecules and iron (Fe) adatoms to 473 K on Au(111). Subsequently, when the sample was annealed to 673 K, intermolecular dehydrogenative C–C coupling facilitated by the coordination pocket template in the coordination polymers led to the formation of planar π-extended [n]CPPs (n= 24, 26, 27, 28 and 31) and other cyclic polymers of varying sizes and shapes. There are two positions for the dehydrogenation C-C coupling between two H_2bbim molecules resulting in three kinds of covalent nodes (2x one side, 1x both sides in Figure 5.1c). The cyclic polymers formed through random combinations of these three covalent nodes, but the planar π-extended CPPs formed by combining node-2 (or node-3) and node-1. Furthermore, the resulting covalent polymers are capable of spanning across steps of Au(111). The investigations were carried out utilizing a combined scanning tunnelling microscopy (STM) and non-contact atomic force microscopy (nc-AFM) in ultrahigh vacuum at T = 5 K. The planarized π-extended CPPs exhibits an exclusive all para-conjugation at their inner edge, leading to delocalized electronic states across the entire ring. The intriguing planar ring topology and unique electronic properties make the planar π-extended CPPs promising quantum materials.

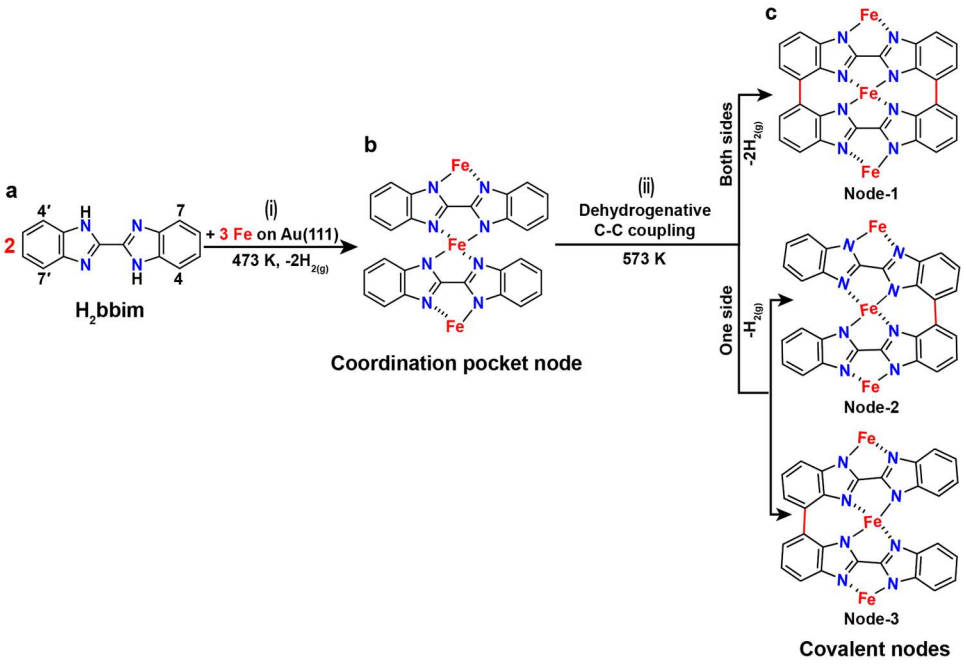

Figure 5.1: Schematic representation of dehydrogenative C–C coupling between two H_2bbim molecules on Au(111). a) Chemical structure of the molecular precursor H_2bbim. b) The coordination pocket node in the coordination polymers (Figure 5.2a-b) formed by step (i). c) The covalent nodes in the covalent polymers (Figure 5.4) formed by step (ii). The as-formed C–C bonds are highlighted in red.

Results and discussion

We deposited sub-monolayer of H_2bbim molecules and Fe atoms onto a clean Au(111) surface kept at room temperature. Subsequent annealing of the sample to 473 K led to the formation of flexible coordination polymers (CPs) that adsorb preferentially in the face-centered cubic domains of the Au(111) surface reconstruction, as illustrated in Figure 5.2a-b. The connecting node of the CPs is a four-fold coordination site, the earlier introduced *N,N-N,N* chelating pocket, as presented in Figure 5.1b. The pocket comprises two =N···Fe and two -N-Fe bonds that form through the dehydrogenation of -NH groups and bond with Fe atoms. Notably, some CPs exhibit bright spots on top of them and a high-resolution STM in Figure 5.2b reveals that these bright spots appear on the end of individual H_2bbim molecules. Although providing an unambiguous explanation for these bright spots is challenging, we speculate that they may correspond to intermediate products involved in the dehydrogenative C–C coupling process. We expect C–H activation to occur at four specific carbon sites (7, 7′, 4, and 4′, Figure 5.1a) in the H_2bbim molecule according to our investigation presented in the previous chapter. Upon annealing the sample to 573 K, dehydrogenative C–C coupling occurs between parts of H_2bbim molecules (Figure 5.2c-d). In Figure 5.2d, two distinct types of dehydrogenative C-C coupling can be observed, indicated by red and white arrows, respectively. The red arrow represents the "both sides" dehydrogenative C–C coupling, where H_2bbim molecules undergo C-H activation at positions 7 and 4' (or 7' and 4), followed by subsequent C–C coupling and formation of two new C-C bonds (Figure 5.1c, node-1). On the other hand, the white arrow corresponds to "one side" dehydrogenative C–C coupling, where only one new C–C bond forms between molecules (Figure 5.1c, node-2 and node-3).

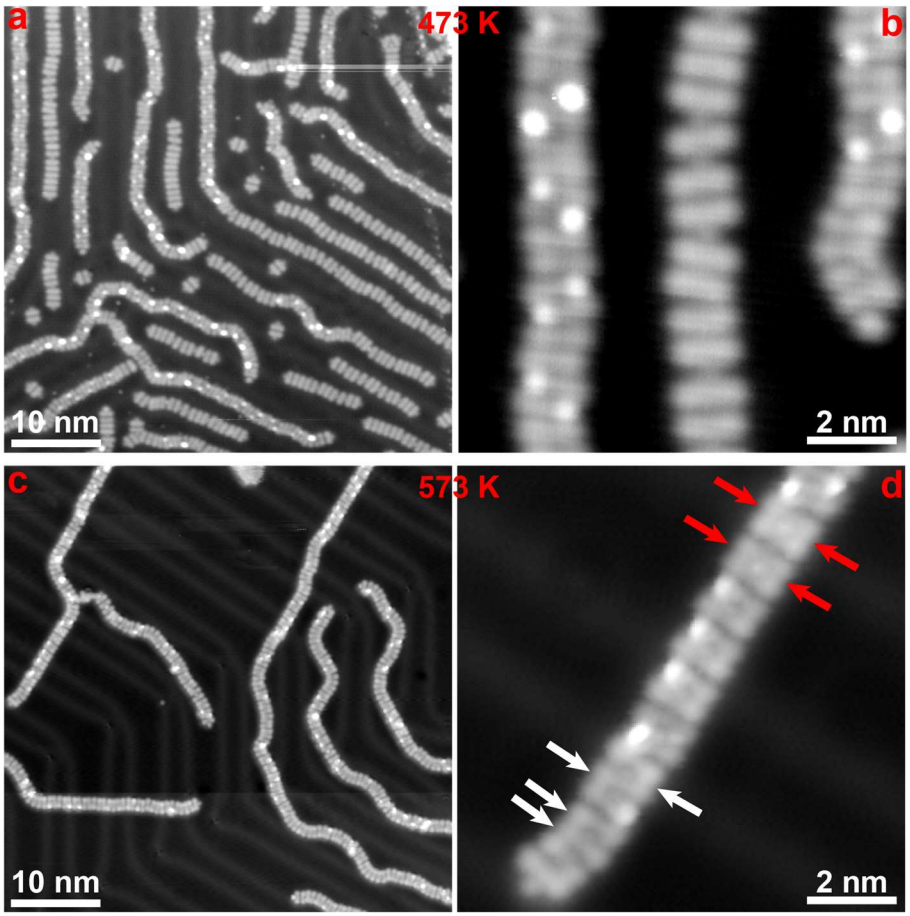

Figure 5.2: (a-b) Coordination-polymers forming after annealing at 473 K. (a) Large-scale STM and (b) zoom-in STM images. (c-d) Chain structure of mixed coordination and covalent polymers following

annealing at 573 K. (c) Large-scale STM and (d) zoom-in STM images. Dehydrogenative C–C coupling occurred between some of the H_2bbim molecules, and the resulting nodes 2/3 and nodes 1 are indicated by red and white arrows, respectively. Scan parameters: (a-b) V_s = 100 mV, I_t = 100 pA; (c-d) V_s = 300 mV, I_t = 100 pA. All STM images were acquired at 4.6 K.

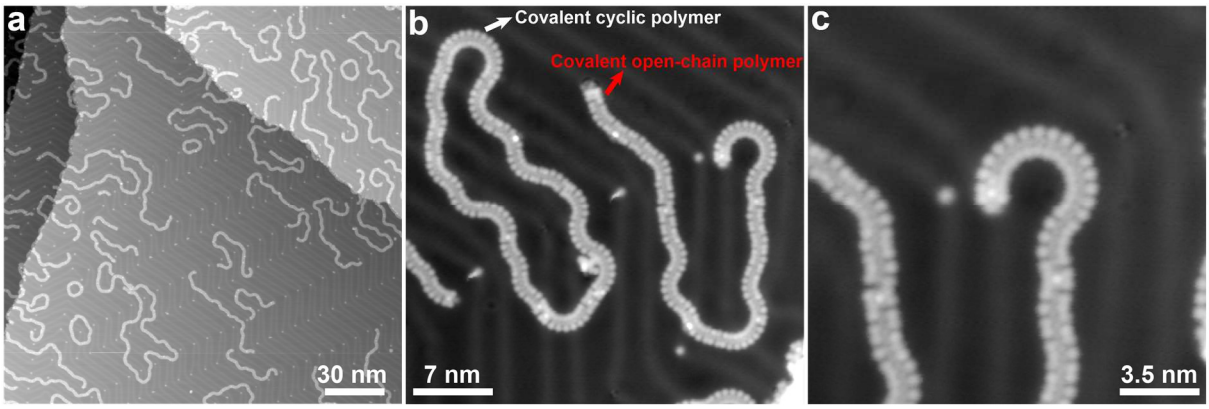

Figure 5.3: (a-c) Overview, large-scale, and zoom-in STM images taken after annealing the sample to 673 K. Scan parameters: (a) V_s = -1 V, I_t = 100 pA; (b-c) V_s = -200 mV, I_t = 100 pA. All STM images were acquired at 4.6 K.

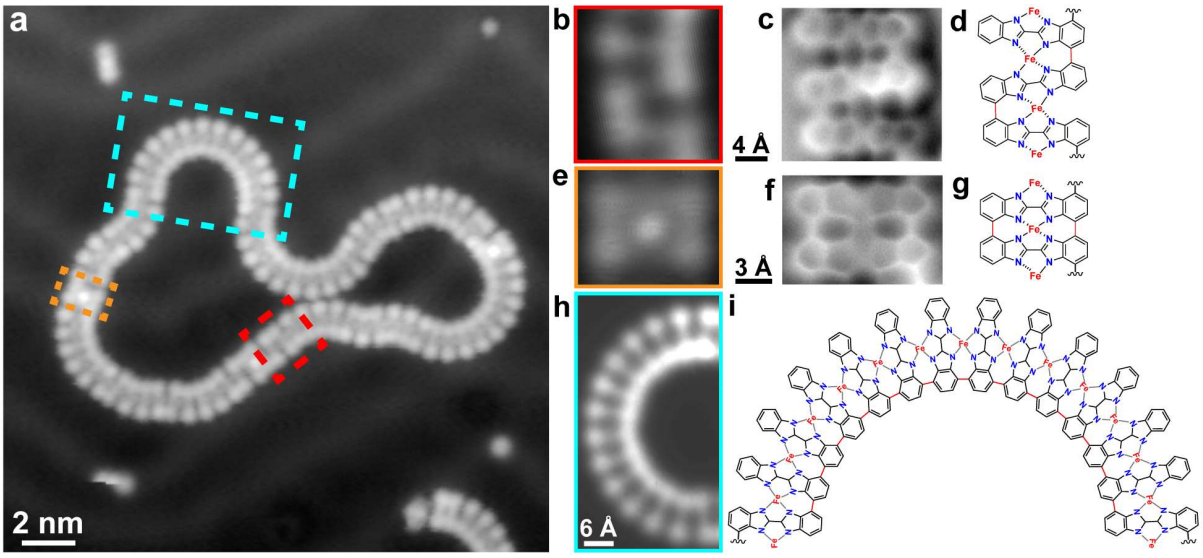

Figure 5.4: On-surface synthesis of the covalent cyclic polymer after annealing the sample to 673 K. (a) STM image of a cyclic polymer on Au(111). Magnified STM (b), nc-AFM (c) images and chemical structure (d) of a zigzag structure framed in red in (a). Zoom-in STM (e), nc-AFM (f) images and chemical structure (g) of a rectangular structure framed in orange in (a). Zoom-in STM image (h) and chemical structure (i) of an arched structure framed in cyan in (a). Scan parameters: (a) V_s = 100 mV, I_t = 100 pA; (b, e, h) Constant height, V_s = 50 mV; (c, f) Constant height, V_s = 0 mV. All STM and nc-AFM images were acquired at 4.6 K.

After annealing at 673 K, dehydrogenative C-C coupling occurred in almost every H_2bbim molecule within the coordination polymers, resulting in the formation of covalent open-chain and cyclic polymers with varying shapes (Figure 5.3). Figures 5.3b and 5.4a depict one large cyclic polymer (consisting of ~125 H_2bbim molecules) and one medium-sized cyclic polymer (consisting of ~90 H_2bbim molecules), respectively (for open-chain polymer please refer to Figure 5.3b-c). We observed that the Fe atoms still remain between H_2bbim molecules within the covalent polymers and show as dot-like features, indicating that high-temperature annealing

process possibly did not cause the removal of Fe atoms from the polymer structure. Notably, the polymers form through random combinations of the three covalent nodes depicted in Figure 5.1c. For example, Figure 5.4b, which is a zoom-in STM image of a red marked area in Figure 5.4a, reveals a zigzag structure composed of node-2 and node-3, with the corresponding chemical structures presented in Figures 5.4d. The nc-AFM image of this structure in Figure 5.4c confirms covalent connection between molecules. Furthermore, Figure 5.4e shows a rectangular structure and its nc-AFM in Figure 5.4f presents a macrocyclic feature. Thus, the rectangular structure is attributed to metalloporphyrinoid comprising of node-1, resembling a structure we previously reported. We do not delve further into its discussion in this chapter but more detailed information on the metalloporphyrinoid and longer H_2bbim-based nanoribbon can be found in Appendix A. Additionally, Figure 5.4h displays an arched structure composed of fourteen H_2bbim molecules connected solely by node-2 or node-3. The inner side of the arched structure forms a [14]poly(p-phenylene) with armchair edge (Figure 5.4i). To further confirm the covalent nature of the structure in Figure 5.4a, we performed a series of tip manipulations on it, as shown in Figure 5.5. The results demonstrate that although the shape of the cyclic polymer changes under tip manipulation, it remains intact, indicating its robustness and flexibility. For comparison, we also performed these manipulations on a non-covalent cyclic structure containing a single coordination node indicated by a white dashed circle in Figure 5.6a. It can be observed that the non-covalent cyclic structure easily disassembles into a covalent open-chain polymer after the tip manipulation (Figure 5.6c). Based on these findings, we can conclude that the structure in Figure 5.4a is covalent and that we can distinguish between covalent and non-covalent structures by analyzing the node motif. Interestingly, we observed that some of the synthesized polymers were able to span across the step edges of the Au(111) surface, probably suggesting that the process of formation of these polymers was not limited by steps, as shown in Figure 5.7. This phenomenon is rarely reported since reaction products typically reside on the same terrace. Additional intriguing covalent polymers, showcasing diverse shapes, feature in Appendix B. These polymers are mobile at r.t. (c.f. Appendix C).

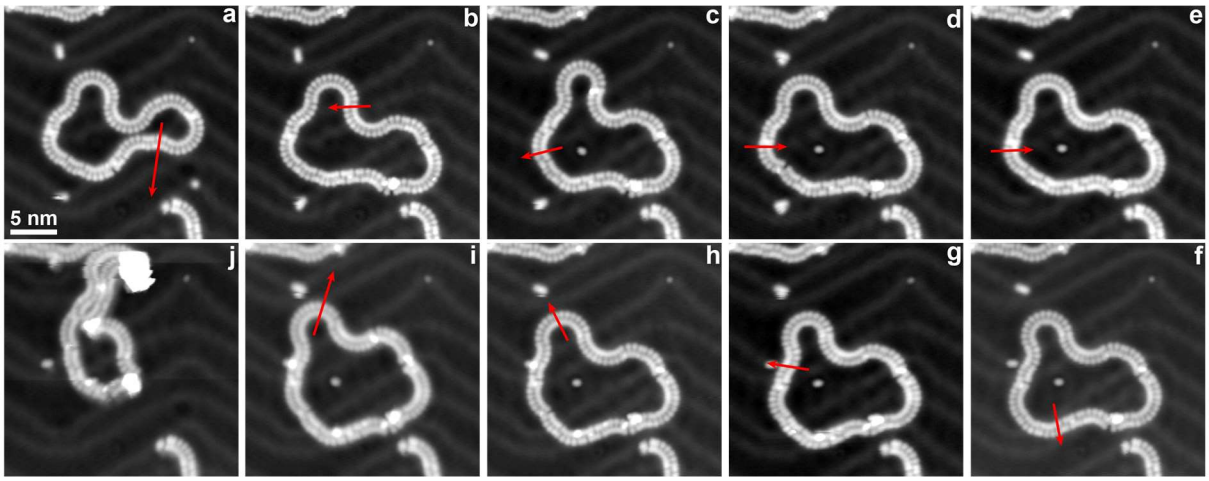

Figure 5.5: (a-j) A series of tip-manipulation operations on a cyclic polymer. Red arrows indicate manipulation trace of the STM tip. Although the shape of the cyclic polymer changes under tip manipulation, it remains intact, indicating its robustness and flexibility. The red arrow indicates the path of tip during manipulation. Tip-sample distance is defined at tunneling condition of I_t = 1 nA, V_s = 3 mV with the tip placed above the polymer; the tip was then moved with a speed of 100 pms^{-1} in the constant height mode. Scan parameters: (a-j) V_s = -100 mV, I_t = 100 pA. All STM images were acquired at 4.6 K.

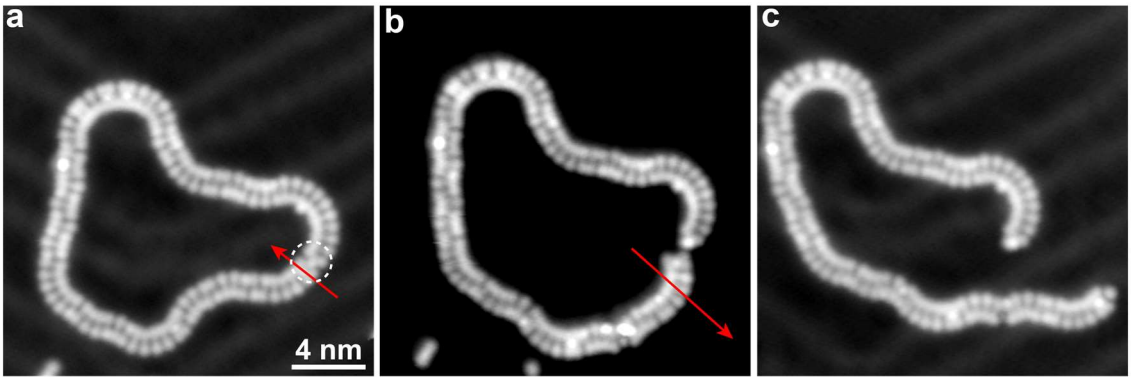

Figure 5.6: (a-c) A series of tip-manipulation operations on a non-covalent cyclic structure containing a single coordination node indicated by a white dashed circle. The red arrow indicates the path of tip during manipulation. Tip-sample distance is defined at tunneling condition of I_t = 1 nA, V_s = 3 mV with the tip placed above the polymer; the tip was then moved with a speed of 100 pms^{-1} in the constant height mode. Scan parameters: (a-c) V_s = -100 mV, I_t = 100 pA. All STM images were acquired at 4.6 K.

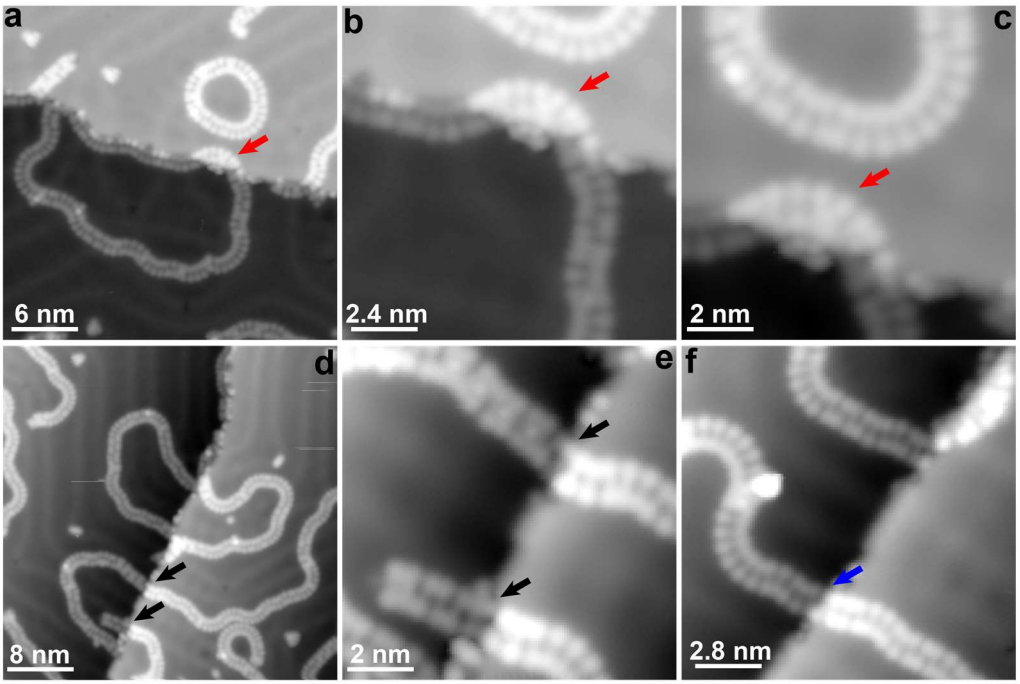

Figure 5.7: Certain synthesized polymers can span across the steps of the Au(111) surface. (a, d) Large-scale STM images of covalent polymers. (b-c, e-f) Zoom-in STM images of the polymers at the edge of the step. The arrows highlight the polymers that can span across the steps. Scan parameters: (a-c) V_s = -80 mV, I_t = 100 pA; (d, f) V_s = -100 mV, I_t = 100 pA; (e) V_s = -50 mV, I_t = 100 pA. All STM images were acquired at 4.6 K.

The synthesis scheme of these polymers appears to be quite versatile. For example, polymers with similar topologies were found when employing Ho atoms instead of Fe atoms, however their presence in the polymers could not be verified by the STM imaging (Appendix D). To probe the role of the metal substrate, the chemistry of H_2bbim and Fe was investigated on Ag(111) (Appendix E) and Ag(100) (Appendix F). Whereas on Ag(111) similar results as on Au(111) were obtained, the Ag(100) clearly favored the formation of distinct Fe-porphyrinoids (node 1) which were incorporated mostly in coordination rather than covalent polymers.

In addition to large and medium cyclic polymers, small cyclic polymers composed of 20 ~ 40 H_2bbim molecules have also been found (Figure 5.8a-d). Interestingly, the small cyclic polymers tend to have a more circular shape than the large and medium ones, and one example is give in Figure 5.9. This round polymer comprises 24 H_2bbim molecules connected by node-1, node-2, and node-3. Notably, the corresponding high-resolution constant-height STM image (Figure 5.9c) reveals that its interior is not a continuous covalent ring (planar cycloparaphenylene) since it contains a defect marked by a red arrow. This defect is most likely caused by the simultaneous presence of node-2 and node-3 in the round polymer, as shown in Figure 5.4b. But also a round polymer was found and is presented in Figure 5.10a, which consists of 24 H_2bbim molecules interconnected through combinations of node-2 (or node-3) and node-1. A constant-height STM image of this polymer (Figure 5.10b) distinctly displays an unbroken ring without any defects along its inner edge. The high-resolution nc-AFM image (Figure 5.10c) and its Laplace-filtered nc-AFM image (Figure 5.10d) confirm that the inner edge of this round polymer is indeed a cycloparaphenylene. Notably, phenylenes have subtle differences in their tilts towards the surface plane; some of them appear as very bright features, indicating that they bent toward the vacuum while others appear as depression, suggesting that they bent toward the substrate. Based on these observations, a plausible chemical structure of this polymer is proposed in Figure 5.10e, and the covalent ring can be identified as an overall planar [24]CPP, indicating that this round polymer is a π-extended [24]CPP. The electronic structure of the planar π-extended [24]CPP on Au(111) was investigated through dI/dV measurements using STS. In Figure 5.11a, characteristic dI/dV spectra collected at the inner side (depicted in red) of the planar π-extended [24]CPP, along with the reference spectrum recorded on bare Au(111) (shown in green), are presented. At the red points, a distinct broad resonance at 1.5 V is observed for the unoccupied levels, presumably associated with the LUMO. The planar π-extended [24]CPP's constant-current dI/dV map (Figure 5.11b) at this bias shows that the inner side of the planar π-extended [24]CPP, cycloparaphenylene, appears as a bright protruding ring, indicating delocalized electronic states along the entire carbon backbone of the cycloparaphenylene. It's noteworthy that the highest occupied molecular orbital (HOMO) is not observed within the bias range from -1 V to 0 V. Apart from the planar π-extended [24]CPP, various sizes of π-extended CPPs, such as [31], [28], [27] and [26], have been found, as shown in Figure 5.12. Nevertheless, it is worth noting that these planar π-extended CPPs show a preference for forming at the edges of steps. Therefore, we hypothesize that the step edge play a crucial role in facilitating the formation of these nanohoops. Moreover, we noted that the yield of small cyclic polymer is not so low, but the yield of the planar π-extended CPPs is not very high. This is primarily because node 2 and node 3 often coexist in a polymer, leading to a discontinuous covalent ring in its interior, as shown in Figure 5.8.

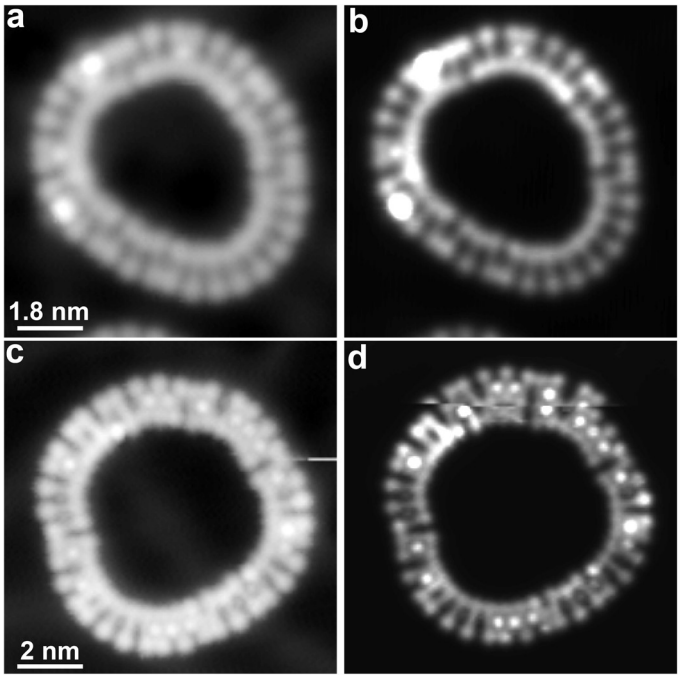

Figure 5.8: Small cyclic polymers composed of 20 ~ 40 H_2bbim molecules. (a, c) Constant-current STM images of two small cyclic polymers, respectively. (b, d) Constant-height STM images of corresponding two small cyclic polymers, respectively. Scan parameters: (a) V_s = -100 mV, I_t = 100 pA; (b) Constant height, V_s = 100 mV; (c) V_s = 50 mV, I_t = 100 pA; (d) V_s = 50 mV, I_t = 100 pA. All STM images were acquired at 4.6 K.

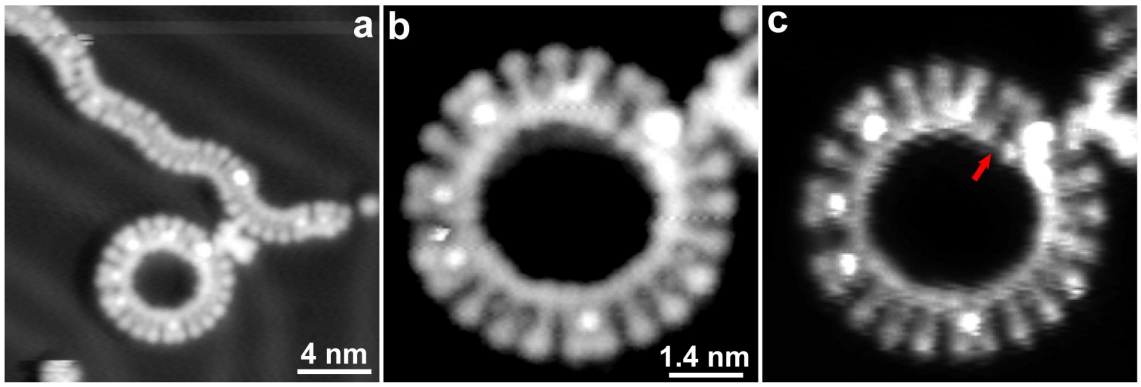

Figure 5.9: A cyclic polymer with a rounded shape. (a-b) Large-scale and magnified constant-current STM images of the cyclic polymer, respectively. (c) Corresponding high-resolution constant-height STM image. The red arrow indicates a defect in its interior. Scan parameters: (a) V_s = -200 mV, I_t = 100 pA; (b) V_s = -20 mV, I_t = 100 pA; (c) Constant height, V_s = 100 mV. All STM images were acquired at 4.6 K.

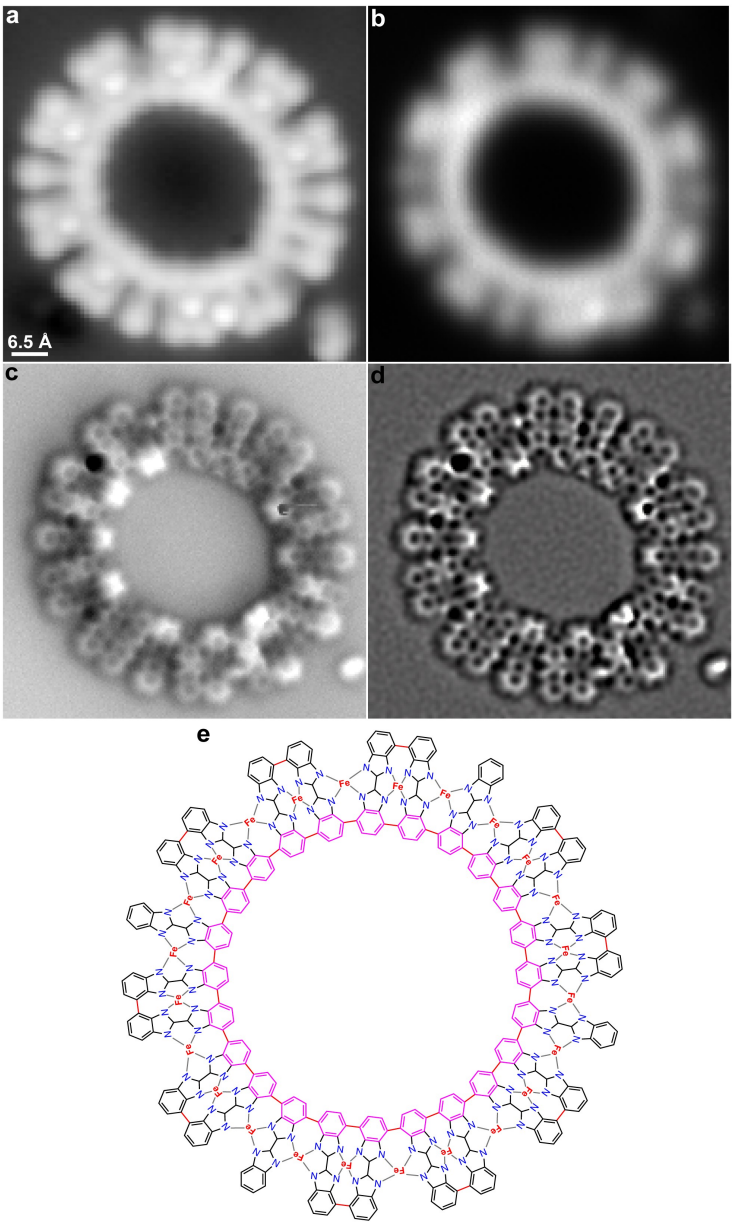

Figure 5.10: On-surface synthesis of planar π-extended [24]CPP. (a) Constant-current STM image, (b) constant-height STM image, (c) nc-AFM image, (d) Laplace-filtered nc-AFM image and (e) structure of the planar π-extended [24]CPP. Scan parameters: (a) V_s = -100 mV, I_t = 10 pA; (b-c) Constant height, V_s = 10 mV and 0 V, respectively.

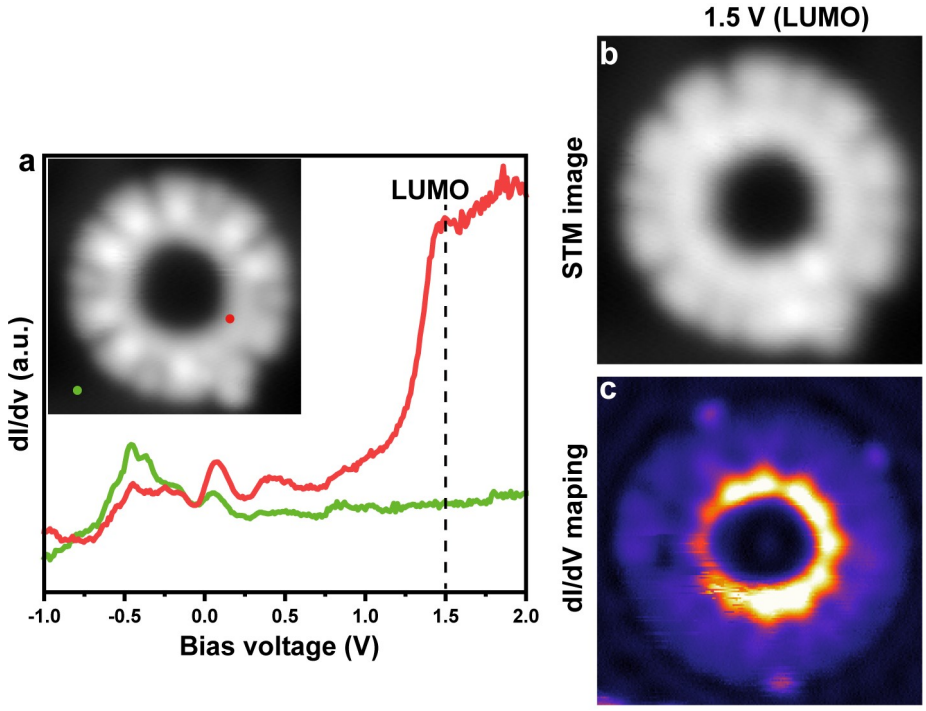

Figure 5.11: Electronic structure of the planar π-extended [24]CPP. (a) Characteristic dI/dV spectra acquired at the positions shown in the inset STM image (colored dots). (b-c) STM image and constant-current dI/dV mapping of the π-extended [24]CPP at 1.5 V (LUMO), respectively. All STM images and dI/dV mapping were acquired at 4.6 K.

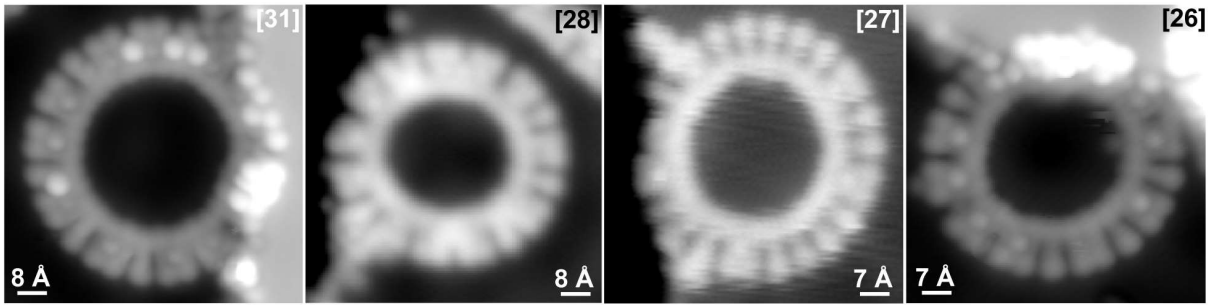

Figure 5.12: Different sizes of planar π-extended CPPs. They are composed of 31, 28, 27 and 26 molecules, respectively, and adsorb at the edge of the step. Scan parameters from left to right side: I_t = 10 pA, V_s = 50 mV; I_t = 10 pA, V_s = 50 mV; I_t = 100 pA, V_s = 50 mV; I_t = 10 pA, V_s = -50 mV. All STM images were acquired at 4.6 K.

Conclusion

We have achieved the successful on-surface synthesis of planar π-extended [n]CPPs (such as n = 24, 26, 27, 28 and 31) through intermolecular dehydrogenative C-C coupling assisted by coordination pocket templates. The planar π-extended CPPs features an all-armchair edge and solely para-connected phenylene units at its inner periphery. The unique para-conjugation at the inner edges produces electronically delocalized states. Our synthetic strategy, intermolecular dehydrogenative C–C coupling facilitated by the coordination pocket template, opens new avenues toward macrocyclic nanostructures and provides a rich playground to investigate fundamental electronic properties of these macrocyclic nanostructures. Additionally, these groundbreaking macrocyclic nanostructures may pave the way for innovative atomically precise quantum materials.

6. Conclusions and outlook

In this thesis, various macrocyclic nanostructures were synthesized through intermolecular deoxygenative and dehydrogenative C–C coupling facilitated by special coordination pocket templates on atomically flat metal surfaces. A comprehensive study of the synthesis's process as well as structural, electronical and chemical properties of the macrocyclic nanostructures was conducted by a combined approach of scanning tunneling microscopy, bond-resolved non-contact atomic force microscopy, X-ray photoelectron spectroscopy and supported by complementary DFT calculations.

Chapter 3 presents the fabrication of high-quality, extended CPs on planar silver surfaces by using two natural dyes (indigo and Tyrian purple). CPs incorporating *trans*-dehydroindigo molecules and Fe adatoms have been successfully realized on Ag(111) and Ag(100). The dehydrogenation induced by iron-coordination transforms the central double bond of the molecule into a single bond, enabling the rotation of the indole moieties on both surfaces. On Ag(111), the difference in the binding of *cis* and *trans* dehydroindigo isomers to the surface mediates an isomerization of the molecular linker within the CP. For this isomerization, both the Fe coordination and the presence of the Ag substrate are crucial: their combination results in an energy gain when the molecular monomer transforms from *trans* to *cis*. These results reveal the realization of interfacial metal-organic nanosystems, where different types of CPs are accessible by the linker isomerization, offering a new pathway to alter the physicochemical properties of the respective CPs. Finally yet importantly, with the presented strategy of employing such natural dyes, biocompatibility and biodegradability may be imparted in such advanced composites.

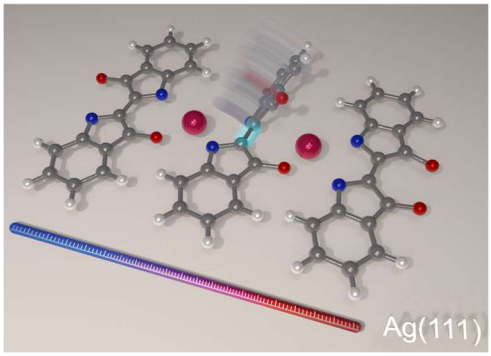

In Chapter 4, we synthesized a novel indigo-based porphyrinoid (**Fe-Por**) and its quadruply fused nanotapes (**Fe-Por NT**s) on Au(111). The **Fe-Por**, akin to porphycene derivatives, with high yield through a series of thermally activated reaction steps. These steps include isomerization and selective C–H activation facilitated by a coordination pocket template. Subsequently, deoxygenative and dehydrogenative C–C coupling lead to fusion of **Fe-Por** molecules into **Fe-Por NT**s, specifically **(Fe-Por)$_2$ NT** and **(Fe-Por)$_3$ NT**. These nanotapes feature **Por** segments connected by quadruple linkages, forming two fused six-membered rings and one eight-membered ring. Our research contributes to the advance of on-surface synthesis methodologies for macrocyclic tetrapyrroles by presenting quadruply fused **Por NT**s, thereby expanding the available chemistry in this domain.

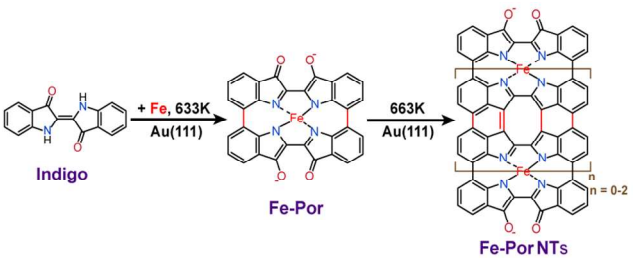

In Chapter 5, building on the findings presented in Chapter 4 (intermolecular highly selective dehydrogenative C–C coupling assisted by the coordination pocket template) we extend this method to H_2bbim: a molecule similar to indigo and it features N atoms in place of the carbonyl

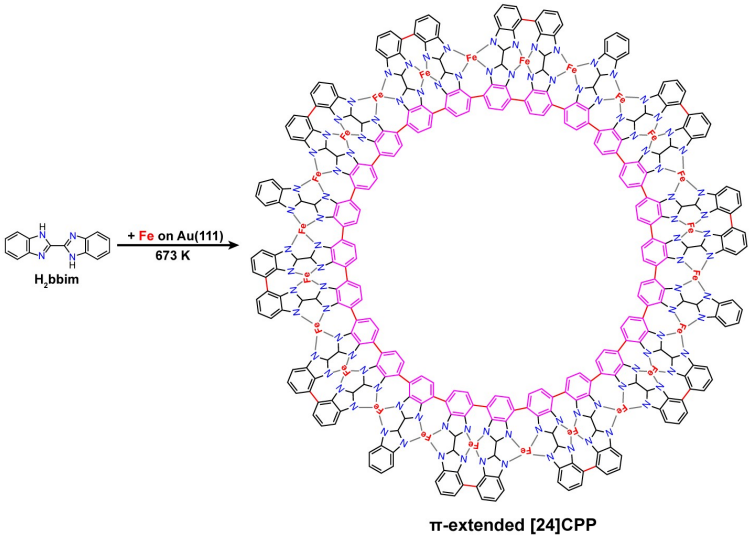

groups. We synthesized planar π-extended [n]CPPs (such as n = 24, 26, 27, 28 and 31) and other types of cyclic polymers through intermolecular dehydrogenative C–C couplings assisted by coordination pocket templates. The planar π-extended CPPs features an all-armchair edge and solely para-connected phenylene units at its inner periphery. The unique para-conjugation at the inner edges produces electronically delocalized states. Our synthetic strategy, intermolecular dehydrogenative C–C coupling facilitated by the coordination pocket template, opens new avenues toward macrocyclic nanostructures and provides a rich playground to investigate fundamental electronic properties of such macrocyclic nanostructures. Additionally, these fascinating macrocyclic nanostructures may pave the way for innovative atomically precise quantum materials.

In addition to the pockets explored in this thesis, we also plan to extend our method to accommodate larger pockets. For instance, the 2,4,6-tris(2-pyridyl)-1,3,5-triazine (TPTZ) molecule has been designed. We foresee that TPTZ molecules will undergo intermolecular cyclization and intermolecular dehydrogenation C–C coupling, assisted by the coordination pocket, to form nitrogen-doped porous graphene nanoribbons or macrocycles. However, specific results require further experimental investigations.

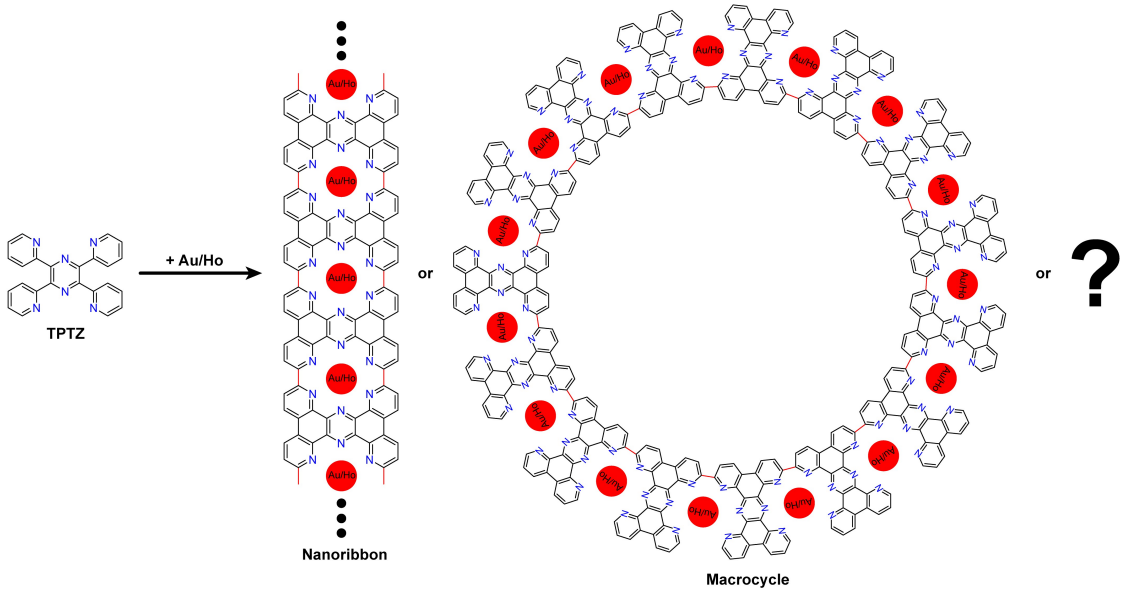

To conclude, this thesis presents systematic studies of novel low dimensional metal-organic materials by coordination pocket templates on noble metal surfaces. Of particular interest are the macrocyclic nanostructures synthesized by intermolecular C–C coupling assisted by the coordination pocket. Especially the novel synthesis method introduced in this comprehensive studies, high selectivity intermolecular C–C coupling assisted by coordination pocket templates,

offers novel insights into fundamental aspects of on-surface synthesis and paves the way for the fabrication of novel macrocyclic nanostructures with unique properties.

A. Appendix – Supplementary data for H_2bbim-based nanoribbon fragments on Au(111)

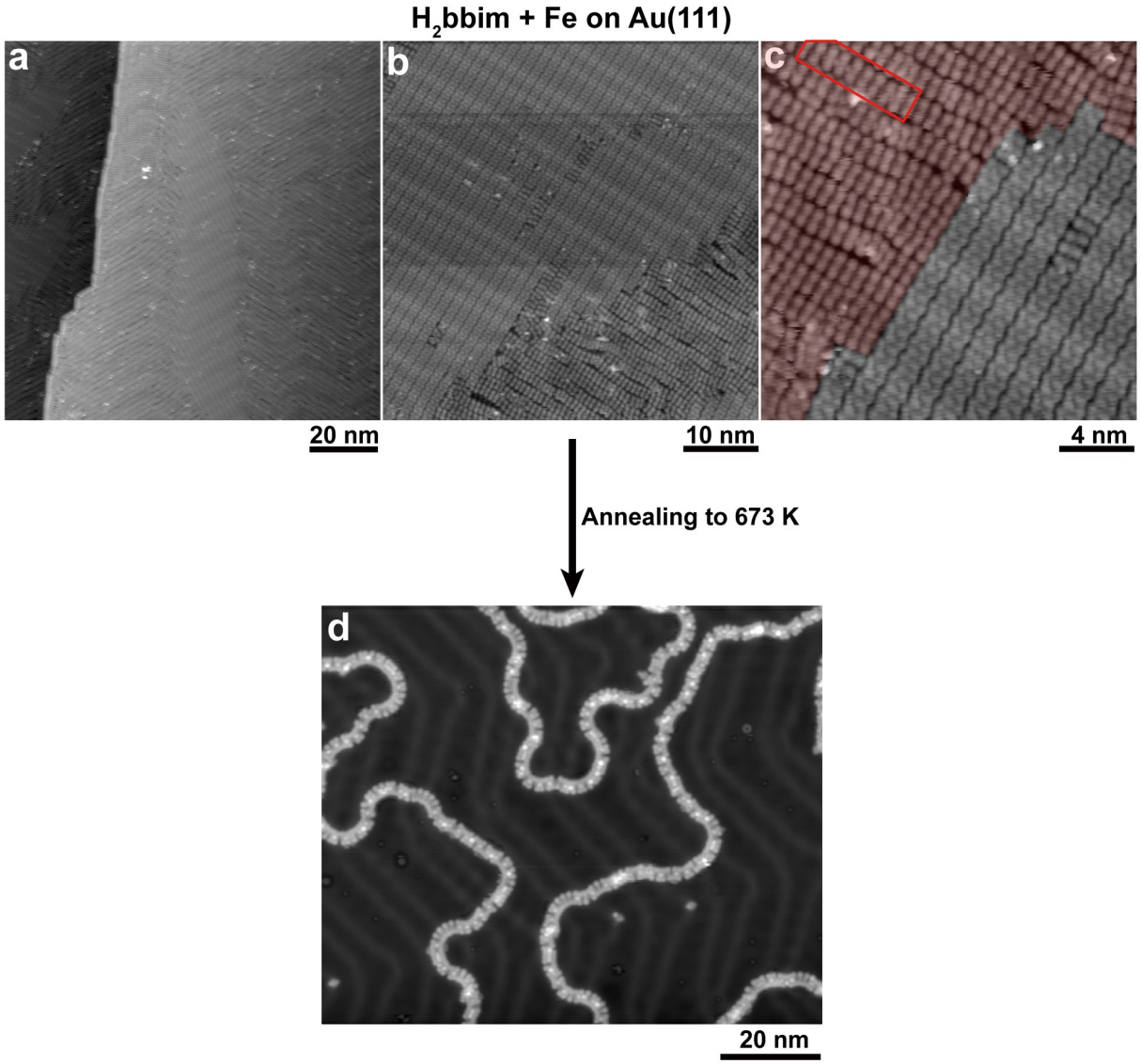

Figure A1: Nearly a full monolayer coverage of H_2bbim molecules and Fe atoms on Au(111), followed by subsequent annealing. (a-c) Overview, large-scale and zoom-in STM images of mixed structure comprising both self-assembly and coordination structures. The region highlighted in red in (c) is a coordination structure, and within a chain marked by a red line, Fe atoms are identifiable as ball features. (d) The result of annealing the sample at 673 K, revealing the formation of covalent polymers. Notably, these polymers encompass longer H_2bbim-based nanoribbon fragments rather than solely dimers (porphyrinoid) compared with the results present in **Chapter 5**. Scan parameters: (a) V_s = -500 mV, I_t = 100 pA; (b-c) V_s = -1 V, I_t = 100 pA; (d) V_s = -100 mV, I_t = 50 pA. All STM images were acquired at 4.6 K.

In **Chapter 5**, we reported that only dimer fragment (that is porphyrinoid synthesized by both sides intermolecular dehydrogenation C–C coupling) could be found after annealing sub-monolayer of H_2bbim molecules and Fe atoms to 673 K. Longer nanoribbons, such as trimers, tetramers, and beyond, could not be obtained. Remarkably, by depositing nearly a full monolayer coverage of H_2bbim molecules and Fe atoms on Au(111) and subsequently annealing the sample to 673K (Figure A1), we observed the formation of longer H_2bbim-based

nanoribbon fragments, including dimers, trimers, tetramers, and even pentamers (Figure A2). Various tip height nc-AFM images and bias-dependent STM images of trimers, tetramers, and pentamers are depicted in Figure A3, A4, and A5, respectively. This contrasts with the previous observation where only dimer fragments were obtained. In the nc-AFM image of trimers, tetramers, and pentamers (Figure A2), a conspicuous bright feature is evident in the corresponding nanoribbon, suggesting that these longer nanoribbons deviate from being entirely planar structures. Specifically, the central part of one H_2bbim (two five-membered rings connected by one single C–C bond) within the nanoribbon protrudes into the vacuum. It means that these longer nanoribbon fragments carry significant stress and may not be kinetically and thermodynamically favored. This could potentially explain why longer nanoribbons, such as decamers, are not obtained in the experimental results.

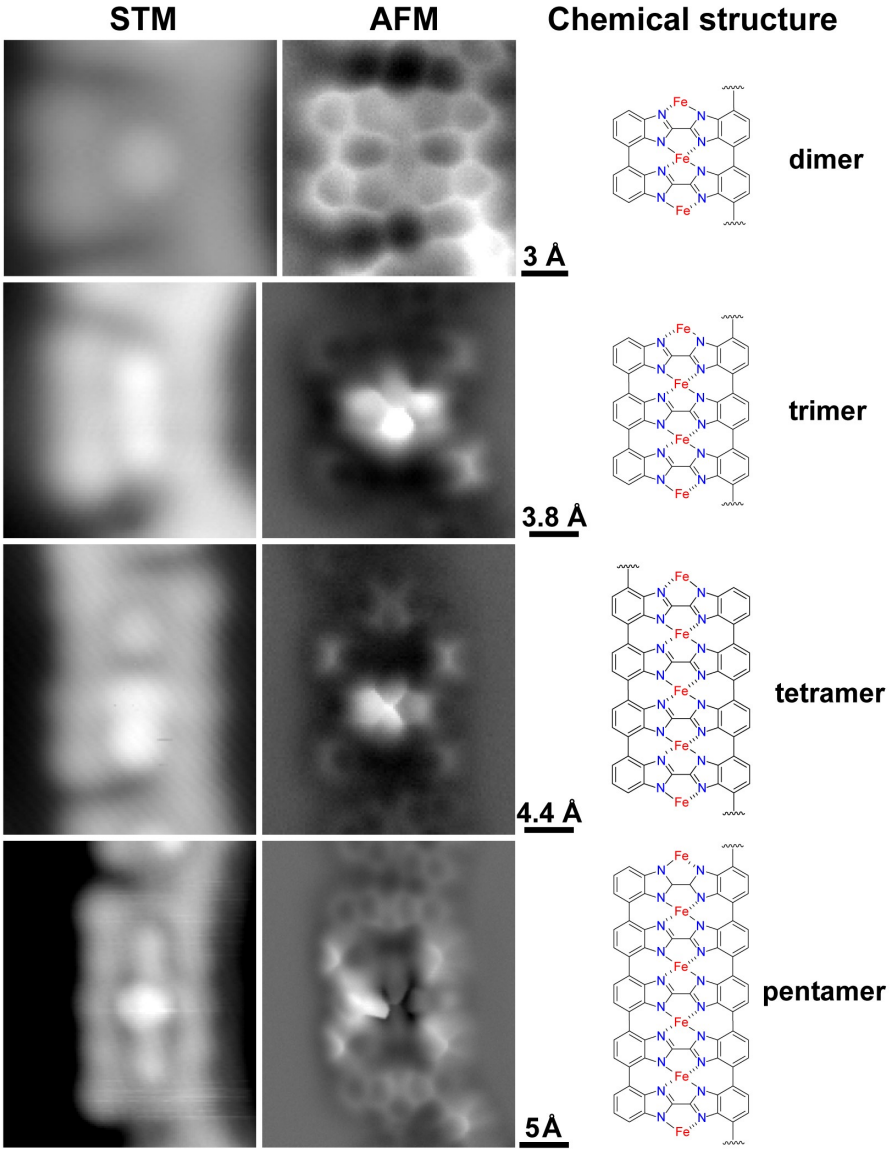

Figure A2: H_2bbim-based nanoribbon fragments on Au(111). Arranged from top to bottom, the structures depicted are a dimer, trimer, tetramer, and pentamer. From left to right are STM images, nc-AFM images, and chemical structures. Scan parameters: V_s = -100 mV, I_t = 10 pA (all STM images); Constant height, V_s = 0 mV (all nc-AFM images). All STM and AFM images were acquired at 4.6 K.

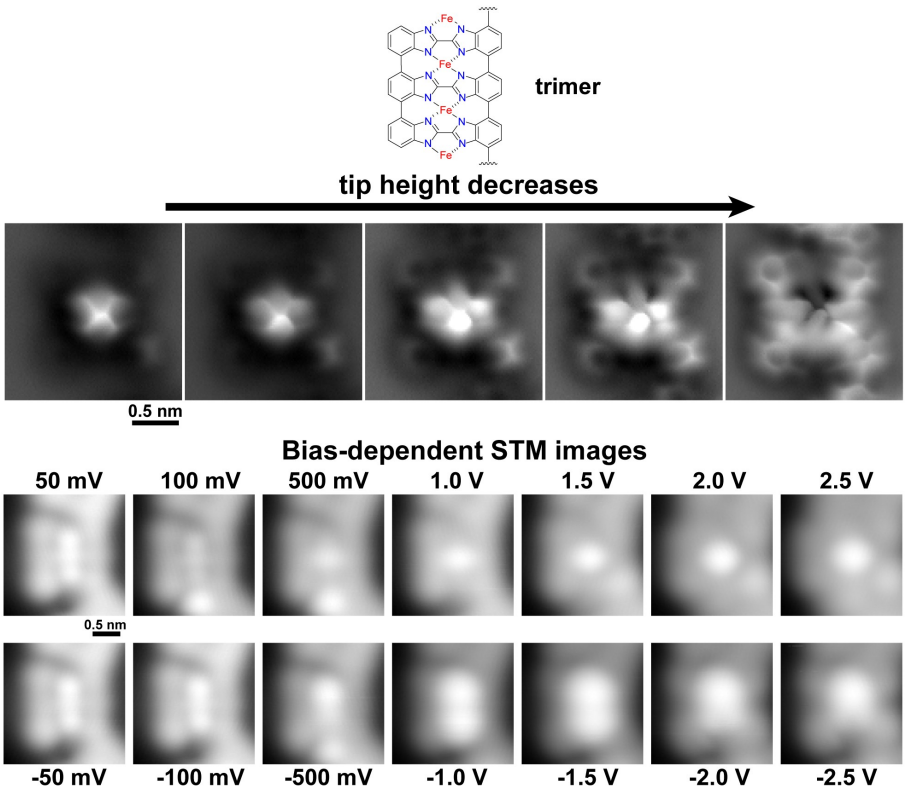

Figure A3: Various tip height nc-AFM images and bias-dependent STM images of the trimer. Scan parameters: $I_t = 10$ pA (all STM images); Constant height, $V_s = 0$ mV (all nc-AFM images). All STM and AFM images were acquired at 4.6 K.

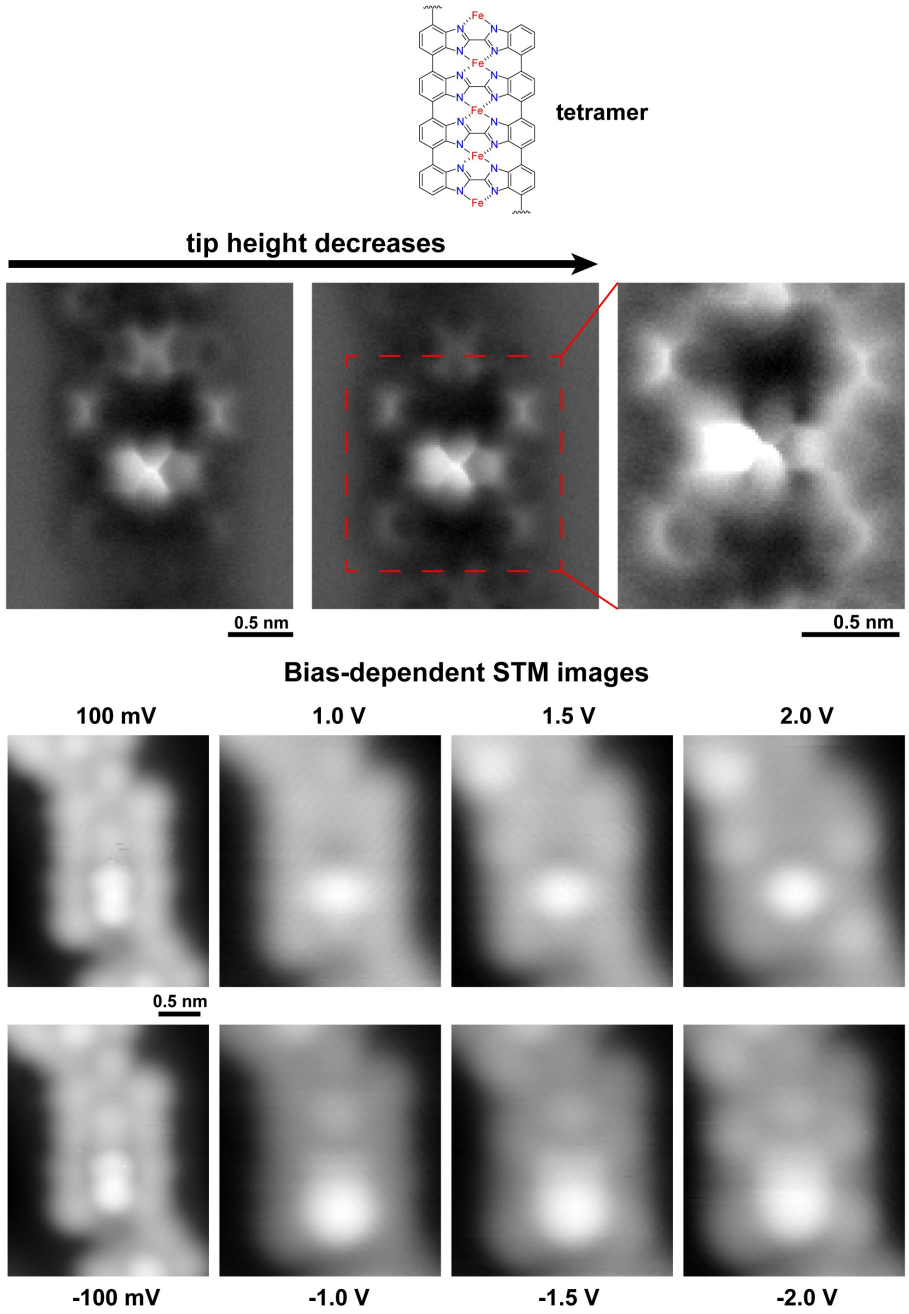

Figure A4: Various tip height nc-AFM images and bias-dependent STM images of the tetramer. Scan parameters: $I_t = 10$ pA (all STM images); Constant height, $V_s = 0$ mV (all nc-AFM images). All STM and AFM images were acquired at 4.6 K.

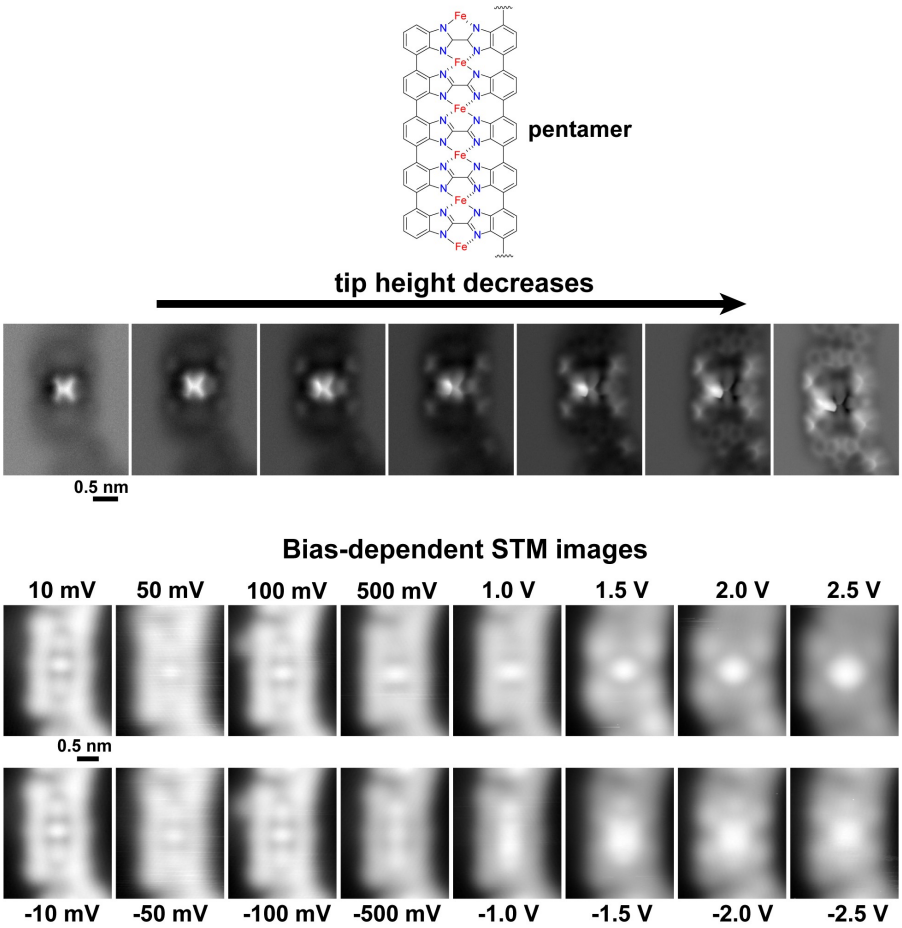

Figure A5: Various tip height nc-AFM images and bias-dependent STM images of the pentamer. Scan parameters: $I_t = 10$ pA (all STM images); Constant height, $V_s = 0$ mV (all nc-AFM images). All STM and AFM images were acquired at 4.6 K.

B. Appendix – Supplementary data for interesting and different shape of covalent polymers on Au(111)

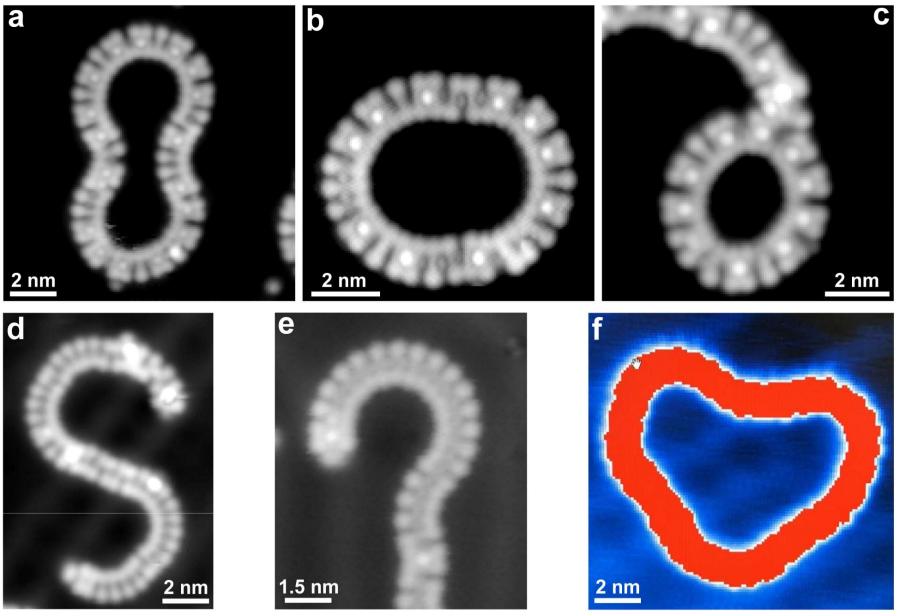

Figure B1. Interesting and different shape of covalent polymers. (a) A cyclic polymer with a shape similar to the number "8". (b) A cyclic polymer with a shape similar to the "circular runway". (c) A cyclic polymer with a shape similar to the "spherical chandelier". (d) A covalent polymer with a shape of "S". (e) A covalent polymer with a shape similar to "question mark". (f) A cyclic polymer with a shape similar to "heart". Scan parameters: (a) V_s = 100 mV, I_t = 10 pA; (b) V_s = -100 mV, I_t = 50 pA; (c) V_s = -100 mV, I_t = 10 pA; (d-f) V_s = 200 mV, I_t = 100 pA. All STM images were acquired at 4.6 K.

It's fascinating that after annealing the sample of H_2bbim molecules and Fe atoms to 673K on Au(111), various covalent polymers with intriguing shapes were also obtained. The cyclic polymers in Figure B1(a-c, f) exhibit forms reminiscent of the number "8", "circular runway", "spherical chandelier", and "heart", respectively. Additionally, the covalent polymers in Figure B1(d-e) take on shapes resembling "S" and "question mark", respectively. This diverse array of shapes adds an interesting dimension to the structural diversity of the synthesized covalent polymers.

C. Appendix – Supplementary data for cyclic and open-chain polymers at room temperature on Au(111)

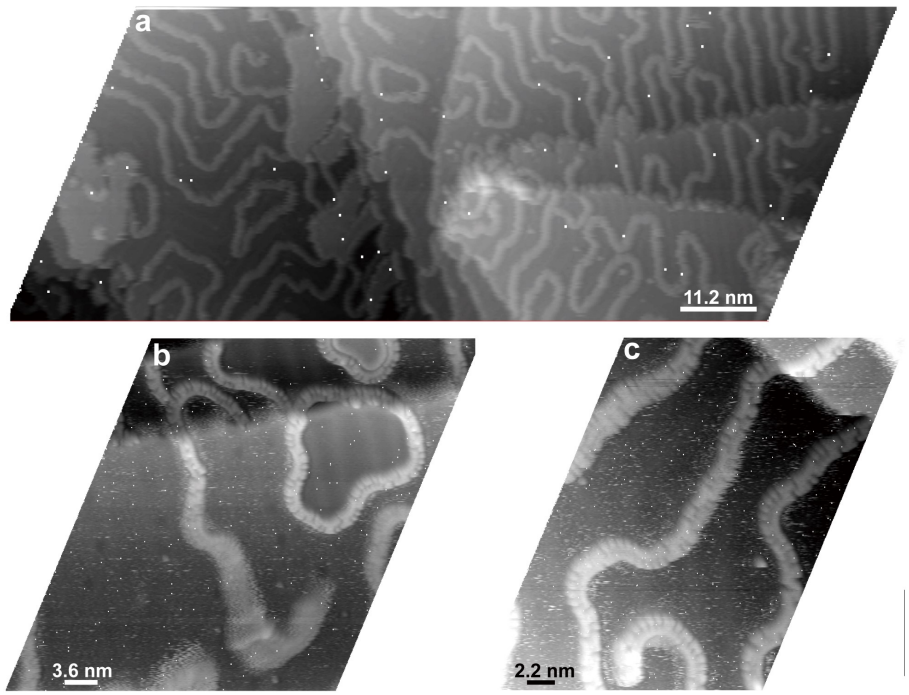

Figure C1: (a-c) Overview, larger-scale, and zoom-in STM images of the polymers at 673 K annealed temperature, respectively. Scan parameters: (a) V_s = -1 V, I_t = 200 pA; (b) V_s = 1.2 V, I_t = 100 pA; (c) V_s = 1.2 V, I_t = 30 pA. All STM images were acquired at room temperature.

To assess the stability and robustness of the synthesized cyclic and open-chain polymers at room temperature, we conducted additional experiments using variable-temperature STM. We deposited a sub-monolayer of H_2bbim molecules and Fe atoms onto Au(111) and annealed the sample to 673 K. Subsequently, the sample was scanned at room temperature. The obtained cyclic and open-chain polymers are illustrated in Figure C1. A closer examination in Figure C1c reveals that the polymers observed are similar to those in **Chapter 5**. However, these polymers exhibit mobility at room temperature, as indicated in Figure C1b, indicating the interaction between these polymers and substrate is weak.

D. Appendix – Supplementary data for H_2bbim + Ho on Au(111) at 673 K annealing temperature

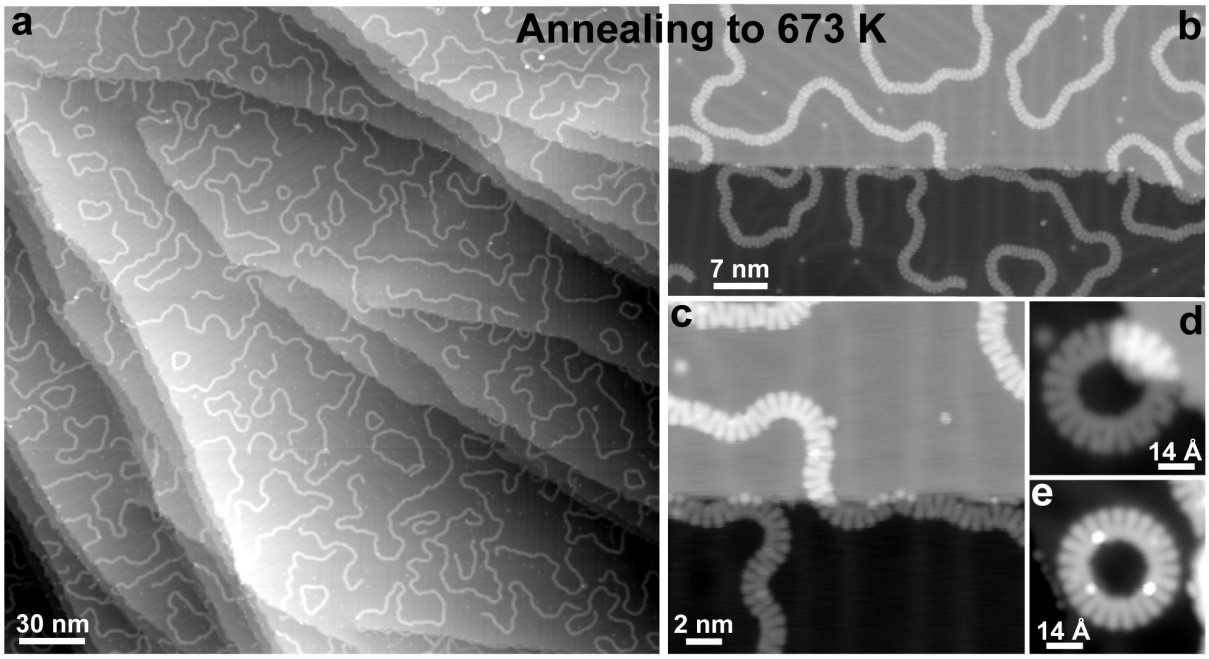

Figure D1: Synthesis of covalent polymers by using H_2bbim and Ho on Au(111). (a-c) Overview, large-scale, and zoom-in STM images of covalent polymers, respectively, after annealing a sample of H_2bbim molecules and Ho atoms to 673 K. (d-e) STM images of nanohoop structures. Scan parameters: (a) V_s = -1 V, I_t = 100 pA; (b-c) V_s = -100 mV, I_t = 100 pA; (d) V_s = -50 mV, I_t = 100 pA; (e) V_s = -20 mV, I_t = 100 pA. All STM images were acquired at 4.6 K.

Out of curiosity regarding the influence of metal size on intermolecular dehydrogenation C–C coupling, we substituted the Fe atom with a larger lanthanide metal, Ho (holmium), and conducted a parallel experiment. Following the same experimental procedure, covalent polymers, including cyclic and open-chain polymers, were obtained upon annealing a sub-monolayer of H_2bbim molecules and Ho atoms on to 673 K Au(111), as depicted in Figure D1. Zoom-in STM images in Figure D1c indicate that Ho atoms are not visible, suggesting that Ho atoms either move away from the polymer or are sandwiched between the polymer and the surface. Two distinct nanohoop structures are presented in Figure D1(d-e) respectively, but both consist of 23 H_2bbim molecules. These results demonstrate the universality of intermolecular dehydrogenation C–C coupling assisted by the coordination pocket, as it remains effective across various metal sizes.

E. Appendix – Supplementary data for H_2bbim + Fe on Ag(111)

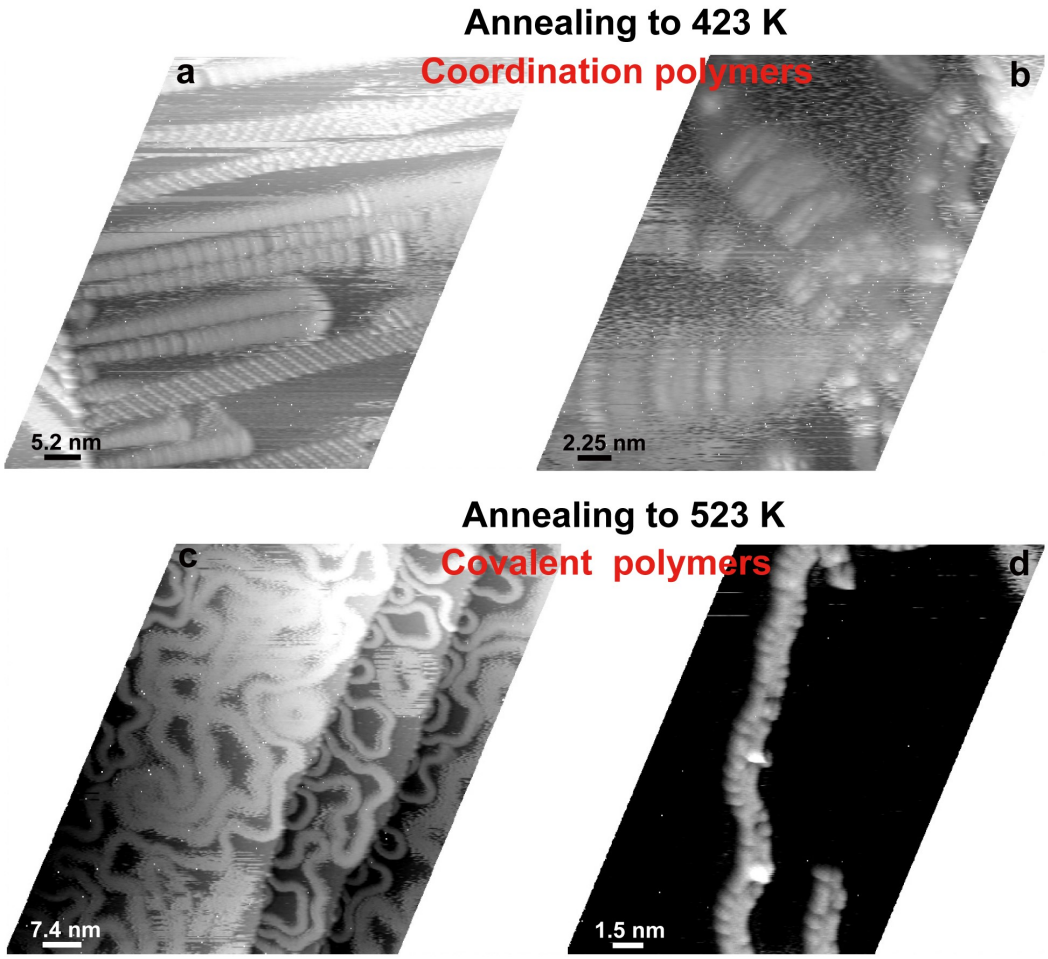

Figure E1: Synthesis of covalent polymers on Ag(111). (a-b) large-scale and zoom-in STM images of coordination polymers consisting of H_2bbim molecules and Fe atoms, respectively, at 423 K annealing temperature. (c-d) Overview and zoom-in STM images of covalent polymers, respectively, at 523 K annealing temperature. Scan parameters: (a) V_s = -1.5 V, I_t = 70 pA; (b) V_s = -1.6 V, I_t = 80 pA; (c) V_s = -1.5 V, I_t = 80 pA; (d) V_s = -1.2 V, I_t = 70 pA. All STM images were acquired at room temperature.

The identical experimental procedures were applied to the Ag(111) surface. Annealing a sub-monolayer of H_2bbim molecules and Fe atoms to 423 K resulted in the formation of coordination polymers, as depicted in Figure E1(a-b). However, STM images of these coordination polymers acquired at room temperature appear fuzzy, suggesting significant mobility of the coordination polymers at room temperature. Covalent polymers are observed after annealing the sample to 523 K, as illustrated in Figure E1d. Overview STM images of the polymers in Figure E1c indicate the same substantial mobility at room temperature, suggesting a weak interaction between the synthesized polymers and the substrate.

F. Appendix – Supplementary data for H_2bbim + Fe on Ag(100): high-yield H_2bbim-based Fe-porphyrinoids

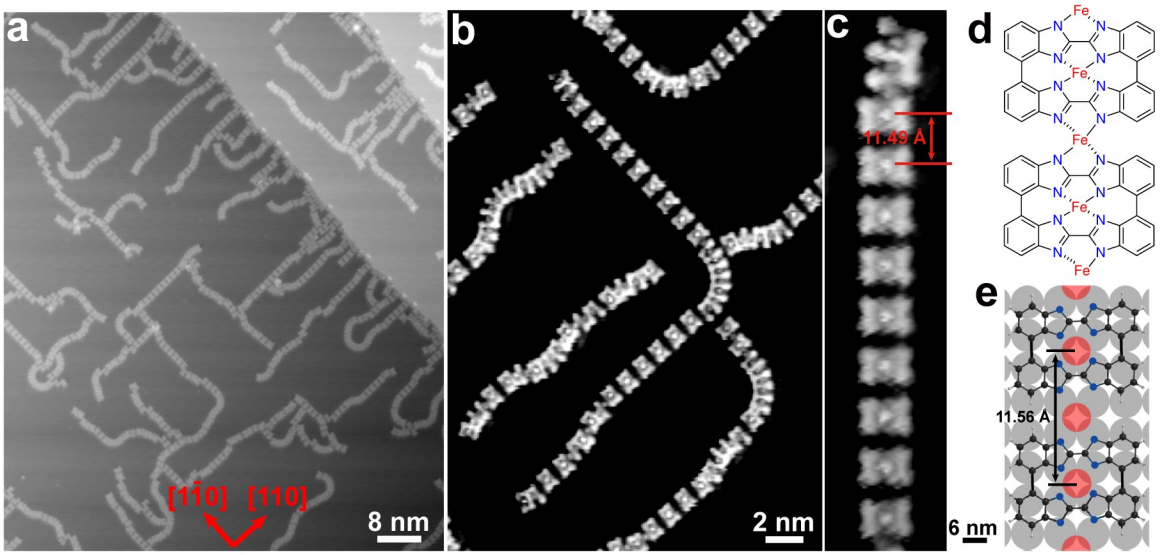

Figure F1: Synthesis of H_2bbim-based Fe-porphyrinoids with high yield at 623 K annealing temperature on Ag(100). (a-c) Overview, zoom-in and zoom-in STM images of coordination polymers consisting of Fe-porphyrinoids, respectively. (d) A rough chemical structure model for two adjacent Fe-porphyrinoids. (e) A possible ball-and-stick model for coordination polymers consisting of Fe-porphyrinoids. C, N, H, Fe and Ag atoms are depicted in black, blue, white, red and silver, respectively. Scan parameters: (a) V_s = -250 mV, I_t = 100 pA; (b-c) V_s = -50 mV, I_t = 100 pA. All STM images were acquired at 4.6 K.

In an effort to understand the influence of epitaxy on intermolecular dehydrogenation C–C coupling assisted by the coordination pocket, the substrate was changed to Ag(100). Employing identical experimental procedures, unexpectedly, annealing a sub-monolayer of H_2bbim molecules and Fe atoms to 623 K led to the formation of coordination polymers consisting of Fe-porphyrinoids with a very high yield, as depicted in Figure F1. It was observed that the distance between two adjacent Fe-porphyrinoids within the coordination polymers is large due to an uncertain factor and the distance between two adjacent centers of Fe-porphyrinoids is 11.49 Å, as shown in Figure F1c. A tentative chemical structure model for two adjacent Fe-porphyrinoids is presented in Figure F1d, indicating the presence of one Fe atom between two adjacent Fe-porphyrinoids. A plausible ball-and-stick model for the coordination polymers consisting of Fe-porphyrinoids is illustrated in Figure F1e. The distance between two adjacent centers of Fe-porphyrinoids in this model is 11.56 Å, matching the experimental measurement value. Notably, in this potential model, all Fe atoms align with the hollow site of the Ag(100) surface.

List of publications

- **On-surface isomerization of indigo within 1D coordination polymers**
  Hongxiang Xu, Ritam Chakraborty, Abhishek Kumar Adak, Arpan Das, Biao Yang, Dennis Meier, Alexander Riss, Joachim Reichert, Shobhana Narasimhan, Johannes V. Barth, and Anthoula C. Papageorgiou
  Angew. Chem. Int. Ed. **2024**, e202319162.
- **From indigo to on-surface synthesis, coordination and fusion of metalated porphyrinoids on a planar gold surface**
  Hongxiang Xu, Ritam Chakraborty, Arpan Das, Biao Yang, Alexander Riss, Joachim Reichert, Shobhana Narasimhan, Johannes V. Barth, and Anthoula C. Papageorgiou
  in preparation.
- **Planar π-extended cycloparaphenylenes with an all-armchair inner edge**
  Hongxiang Xu, Biao Yang, Alexander Riss, Joachim Reichert, Johannes V. Barth, and Anthoula C. Papageorgiou
  in preparation.
- **An analogue of 2D bilayer silica films: bimolecular coordination networks, from crystalline to vitreous phases**
  Hongxiang Xu, Ritam Chakraborty, Biao Yang, Joachim Reichert, Shobhana Narasimhan, Johannes V. Barth, and Anthoula C. Papageorgiou
  in preparation
- **Tuning the selectivity of C-H bond activation: 6,6′ (or 5,5′) vs. 7,7′**
  Hongxiang Xu, Abhishek Kumar Adak, Biao Yang, Dennis Meier, Alexander Riss, Joachim Reichert, Shobhana Narasimhan, Johannes V. Barth, and Anthoula C. Papageorgiou
  in preparation
- **On-surface synthesis distinctive C-Ag-N and C-Cu-N organometallic structures *via* using a multifunctional dye molecule**
  Hongxiang Xu, Ritam Chakraborty, Biao Yang, Joachim Reichert, Shobhana Narasimhan, Johannes V. Barth, and Anthoula C. Papageorgiou
  in preparation
- **Depositing molecular graphene nanoribbons on Ag(111) by electrospray controlled ion beam deposition: Self-assembly and on-surface transformations**
  W. Ran, A. Walz, K. Stoiber, P. Knecht, *H. Xu*, A. C. Papageorgiou, A. Huettig, D. Cortizo-Lacalle, J. P. Mora-Fuentes, A. Mateo-Alonso, H. Schlichting, J. Reichert, and J. V. Barth
  Angew. Chem. Int. Ed. **2022**, 134(14): e202111816.

Bibliography

(1) Shen, Q.; Gao, H. Y.; Fuchs, H. Frontiers of on-surface synthesis: From principles to applications. *Nano Today* **2017**, *13*, 77-96, http://dx.doi.org/10.1016/j.nantod.2017.02.007.

(2) Held, P. A.; Fuchs, H.; Studer, A. Covalent-Bond Formation via On-Surface Chemistry. *Chem-Eur J* **2017**, *23* (25), 5874-5892, http://dx.doi.org/10.1002/chem.201604047.

(3) Grill, L.; Hecht, S. Covalent on-surface polymerization. *Nat Chem* **2020**, *12* (2), 115-130, http://dx.doi.org/10.1038/s41557-019-0392-9.

(4) Han, D.; Zhu, J. F. Surface-assisted fabrication of low-dimensional carbon-based nanoarchitectures. *J Phys-Condens Mat* **2021**, *33* (34), http://dx.doi.org/10.1088/1361-648X/ac0a1b.

(5) Clair, S.; de Oteyza, D. G. Controlling a Chemical Coupling Reaction on a Surface: Tools and Strategies for On-Surface Synthesis. *Chem Rev* **2019**, *119* (7), 4717-4776, http://dx.doi.org/10.1021/acs.chemrev.8b00601.

(6) Grill, L.; Dyer, M.; Lafferentz, L.; Persson, M.; Peters, M. V.; Hecht, S. Nano-architectures by covalent assembly of molecular building blocks. *Nat Nanotechnol* **2007**, *2* (11), 687-691, http://dx.doi.org/10.1038/nnano.2007.346.

(7) Albrecht, F.; Fatayer, S.; Pozo, I.; Tavernelli, I.; Repp, J.; Pena, D.; Gross, L. Selectivity in single-molecule reactions by tip-induced redox chemistry. *Science* **2022**, *377* (6603), 298-301, http://dx.doi.org/10.1126/science.abo6471.

(8) Kaiser, K.; Scriven, L. M.; Schulz, F.; Gawel, P.; Gross, L.; Anderson, H. L. An sp-hybridized molecular carbon allotrope, cyclo[18]carbon. *Science* **2019**, *365* (6459), 1299-+, http://dx.doi.org/10.1126/science.aay1914.

(9) Zhong, Q. G.; Ihle, A.; Ahles, S.; Wegner, H. A.; Schirmeisen, A.; Ebeling, D. Constructing covalent organic nanoarchitectures molecule by molecule via scanning probe manipulation. *Nat Chem* **2021**, *13* (11), 1133-+, http://dx.doi.org/10.1038/s41557-021-00773-4.

(10) Grossmann, L.; King, B. T.; Reichlmaier, S.; Hartmann, N.; Rosen, J.; Heckl, W. M.; Bjork, J.; Lackinger, M. On-surface photopolymerization of two-dimensional polymers ordered on the mesoscale. *Nat Chem* **2021**, *13* (8), 730-+, http://dx.doi.org/10.1038/s41557-021-00709-y.

(11) Gao, H. Y.; Zhong, D. Y.; Moenig, H.; Wagner, H.; Held, P. A.; Timmer, A.; Studer, A.; Fuchs, H. Photochemical Glaser Coupling at Metal Surfaces. *J Phys Chem C* **2014**, *118* (12), 6272-6277, http://dx.doi.org/10.1021/jp411889e.

(12) Lafferentz, L.; Ample, F.; Yu, H.; Hecht, S.; Joachim, C.; Grill, L. Conductance of a Single Conjugated Polymer as a Continuous Function of Its Length. *Science* **2009**, *323* (5918), 1193-1197, http://dx.doi.org/10.1126/science.1168255.

(13) Wang, W. H.; Shi, X. Q.; Wang, S. Y.; Van Hove, M. A.; Lin, N. Single-Molecule Resolution of an Organometallic Intermediate in a Surface-Supported Ullmann Coupling Reaction. *J Am Chem Soc* **2011**, *133* (34), 13264-13267, http://dx.doi.org/10.1021/ja204956b.

(14) Fan, Q. T.; Gottfried, J. M.; Zhu, J. F. Surface-Catalyzed C-C Covalent Coupling Strategies toward the Synthesis of Low-Dimensional Carbon-Based Nanostructures. *Accounts Chem Res* **2015**, *48* (8), 2484-2494, http://dx.doi.org/10.1021/acs.accounts.5b00168.

(15) Cai, J. M.; Ruffieux, P.; Jaafar, R.; Bieri, M.; Braun, T.; Blankenburg, S.; Muoth, M.; Seitsonen, A. P.; Saleh, M.; Feng, X. L.; et al. Atomically precise bottom-up fabrication of graphene nanoribbons. *Nature* **2010**, *466* (7305), 470-473, http://dx.doi.org/10.1038/nature09211.

(16) Zwaneveld, N. A. A.; Pawlak, R.; Abel, M.; Catalin, D.; Gigmes, D.; Bertin, D.; Porte, L. Organized formation of 2D extended covalent organic frameworks at surfaces. *J Am Chem Soc* **2008**, *130* (21), 6678-+, http://dx.doi.org/10.1021/ja800906f.

(17) Liu, X. H.; Guan, C. Z.; Ding, S. Y.; Wang, W.; Yan, H. J.; Wang, D.; Wan, L. J. On-Surface Synthesis of Single-Layered Two-Dimensional Covalent Organic Frameworks via Solid-Vapor Interface Reactions. *J Am Chem Soc* **2013**, *135* (28), 10470-10474, http://dx.doi.org/10.1021/ja403464h.

(18) Dienstmaier, J. F.; Gigler, A. M.; Goetz, A. J.; Knochel, P.; Bein, T.; Lyapin, A.; Reichlmaier, S.; Heckl, W. M.; Lackinger, M. Synthesis of Well-Ordered COF Monolayers: Surface Growth of Nanocrystalline Precursors versus Direct On-Surface Polycondensation. *Acs Nano* **2011**, *5* (12), 9737-9745, http://dx.doi.org/10.1021/nn2032616.

(19) Weigelt, S.; Busse, C.; Bombis, C.; Knudsen, M. M.; Gothelf, K. V.; Laegsgaard, E.; Besenbacher, F.; Linderoth, T. R. Surface synthesis of 2D branched polymer nanostructures. *Angewandte Chemie International Edition* **2008**, *47* (23), 4406-4410, http://dx.doi.org/10.1002/anie.200705079.

(20) Jiang, L.; Papageorgiou, A. C.; Oh, S. C.; Saglam, O.; Reichert, J.; Duncan, D. A.; Zhang, Y. Q.; Klappenberger, F.; Guo, Y. Y.; Allegretti, F.; et al. Synthesis of Pyrene-Fused Pyrazaacenes on Metal Surfaces: Toward One-Dimensional Conjugated Nanostructures. *Acs Nano* **2016**, *10* (1), 1033-1041, http://dx.doi.org/10.1021/acsnano.5b06340.

(21) Weigelt, S.; Busse, C.; Bombis, C.; Knudsen, M. M.; Gothelf, K. V.; Strunskus, T.; Woll, C.; Dahlbom, M.; Hammer, B.; Laegsgaard, E.; et al. Covalent interlinking of an aldehyde and an amine on a Au(111) surface in ultrahigh vacuum. *Angewandte Chemie International Edition* **2007**, *46* (48), 9227-9230, http://dx.doi.org/10.1002/anie.200702859.

(22) de Oteyza, D. G.; Gorman, P.; Chen, Y. C.; Wickenburg, S.; Riss, A.; Mowbray, D. J.; Etkin, G.; Pedramrazi, Z.; Tsai, H. Z.; Rubio, A.; et al. Direct Imaging of Covalent Bond Structure in Single-Molecule Chemical Reactions. *Science* **2013**, *340* (6139), 1434-1437, http://dx.doi.org/10.1126/science.1238187.

(23) Sun, Q.; Zhang, C.; Li, Z. W.; Kong, H. H.; Tan, Q. G.; Hu, A. G.; Xu, W. On-Surface Formation of One-Dimensional Polyphenylene through Bergman Cyclization. *J Am Chem Soc* **2013**, *135* (23), 8448-8451, http://dx.doi.org/10.1021/ja404039t.

(24) Zhang, Y. Q.; Kepcija, N.; Kleinschrodt, M.; Diller, K.; Fischer, S.; Papageorgiou, A. C.; Allegretti, F.; Bjork, J.; Klyatskaya, S.; Klappenberger, F.; et al. Homo-coupling of terminal alkynes on a noble metal surface. *Nat Commun* **2012**, *3*, http://dx.doi.org/10.1038/ncomms2291.

(25) Gao, H. Y.; Wagner, H.; Zhong, D. Y.; Franke, J. H.; Studer, A.; Fuchs, H. Glaser Coupling at Metal Surfaces. *Angewandte Chemie International Edition* **2013**, *52* (14), 4024-4028, http://dx.doi.org/10.1002/anie.201208597.

(26) Cirera, B.; Zhang, Y. Q.; Bjork, J.; Klyatskaya, S.; Chen, Z.; Ruben, M.; Barth, J. V.; Klappenberger, F. Synthesis of Extended Graphdiyne Wires by Vicinal Surface Templating. *Nano Lett* **2014**, *14* (4), 1891-1897, http://dx.doi.org/10.1021/nl4046747.

(27) Zhong, D. Y.; Franke, J. H.; Podiyanachari, S. K.; Blomker, T.; Zhang, H. M.; Kehr, G.; Erker, G.; Fuchs, H.; Chi, L. F. Linear Alkane Polymerization on a Gold Surface. *Science* **2011**, *334* (6053), 213-216, http://dx.doi.org/10.1126/science.1211836.

(28) Wiengarten, A.; Seufert, K.; Auwarter, W.; Ecija, D.; Diller, K.; Allegretti, F.; Bischoff, F.; Fischer, S.; Duncan, D. A.; Papageorgiou, A. C.; et al. Surface-assisted Dehydrogenative Homocoupling of Porphine Molecules. *J Am Chem Soc* **2014**, *136* (26), 9346-9354, http://dx.doi.org/10.1021/ja501680n.

(29) Sun, Q.; Zhang, C.; Kong, H. H.; Tan, Q. G.; Xu, W. On-surface aryl-aryl coupling via selective C-H activation. *Chem Commun* **2014**, *50* (80), 11825-11828, http://dx.doi.org/10.1039/c4cc05482b.

(30) Telychko, M.; Li, G. W.; Mutombo, P.; Soler-Polo, D.; Peng, X. N.; Su, J.; Song, S. T.; Koh, M. J.; Edmonds, M.; Jelinek, P.; et al. Ultrahigh-yield on-surface synthesis and assembly of circumcoronene into a chiral electronic Kagome-honeycomb lattice. *Sci Adv* **2021**, *7* (3), http://dx.doi.org/10.1126/sciadv.abf0269.

(31) Treier, M.; Pignedoli, C. A.; Laino, T.; Rieger, R.; Mullen, K.; Passerone, D.; Fasel, R. Surface-assisted cyclodehydrogenation provides a synthetic route towards easily processable and chemically tailored nanographenes. *Nat Chem* **2011**, *3* (1), 61-67, http://dx.doi.org/10.1038/Nchem.891.

(32) Amsharov, K.; Abdurakhmanova, N.; Stepanow, S.; Rauschenbach, S.; Jansen, M.; Kern, K. Towards the Isomer-Specific Synthesis of Higher Fullerenes and Buckybowls by the Surface-Catalyzed Cyclodehydrogenation of Aromatic Precursors. *Angewandte Chemie International Edition* **2010**, *49* (49), 9392-9396, http://dx.doi.org/10.1002/anie.201005000.

(33) Houtsma, R. S. K.; de la Rie, J.; Stohr, M. Atomically precise graphene nanoribbons: interplay of structural and electronic properties. *Chem Soc Rev* **2021**, *50* (11), 6541-6568, http://dx.doi.org/10.1039/d0cs01541e.

(34) Ruffieux, P.; Wang, S. Y.; Yang, B.; Sanchez-Sanchez, C.; Liu, J.; Dienel, T.; Talirz, L.; Shinde, P.; Pignedoli, C. A.; Passerone, D.; et al. On-surface synthesis of graphene nanoribbons with zigzag edge topology. *Nature* **2016**, *531* (7595), 489-+, http://dx.doi.org/10.1038/nature17151.

(35) Bergman, R. G. C–H activation. *Nature* **2007**, *446* (7134), 391-393, http://dx.doi.org/10.1038/446391a.

(36) Rogge, T.; Kaplaneris, N.; Chatani, N.; Kim, J.; Chang, S.; Punji, B.; Schafer, L. L.; Musaev, D. G.; Wencel-Delord, J.; Roberts, C. A.; et al. C–H activation. *Nature Reviews Methods Primers* **2021**, *1* (1), 43, http://dx.doi.org/10.1038/s43586-021-00041-2.

(37) Segawa, Y.; Maekawa, T.; Itami, K. Synthesis of Extended π-Systems through C–H Activation. *Angewandte Chemie International Edition* **2015**, *54* (1), 66-81, http://dx.doi.org/10.1002/anie.201403729.

(38) Li, Q.; Yang, B.; Lin, H. P.; Aghdassi, N.; Miao, K. J.; Zhang, J. J.; Zhang, H. M.; Li, Y. Y.; Duhm, S.; Fan, J.; et al. Surface-Controlled Mono/Diselective ortho C-H Bond Activation. *J Am Chem Soc* **2016**, *138* (8), 2809-2814, http://dx.doi.org/10.1021/jacs.5b13286.

(39) Alberico, D.; Scott, M. E.; Lautens, M. Aryl-aryl bond formation by transition-metal-catalyzed direct arylation. *Chem Rev* **2007**, *107* (1), 174-238, http://dx.doi.org/10.1021/cr0509760.

(40) Gandeepan, P.; Muller, T.; Zell, D.; Cera, G.; Warratz, S.; Ackermann, L. 3d Transition Metals for C-H Activation. *Chem Rev* **2019**, *119* (4), 2192-2452, http://dx.doi.org/10.1021/acs.chemrev.8b00507.

(41) Colby, D. A.; Bergman, R. G.; Ellman, J. A. Rhodium-Catalyzed C-C Bond Formation via Heteroatom-Directed C-H Bond Activation. *Chem Rev* **2010**, *110* (2), 624-655, http://dx.doi.org/10.1021/cr900005n.

(42) He, J.; Wasa, M.; Chan, K. S. L.; Shao, O.; Yu, J. Q. Palladium-Catalyzed Transformations of Alkyl C-H Bonds. *Chem Rev* **2017**, *117* (13), 8754-8786, http://dx.doi.org/10.1021/acs.chemrev.6b00622.

(43) Shang, R.; Ilies, L.; Nakamura, E. Iron-Catalyzed C-H Bond Activation. *Chem Rev* **2017**, *117* (13), 9086-9139, http://dx.doi.org/10.1021/acs.chemrev.6b00772.

(44) Laudadio, G.; Deng, Y. C.; van der Wal, K.; Ravelli, D.; Nuno, M.; Fagnoni, M.; Guthrie, D.; Sun, Y. H.; Noel, T. C(sp(3))-H functionalizations of light hydrocarbons using decatungstate photocatalysis in flow. *Science* **2020**, *369* (6499), 92-+, http://dx.doi.org/10.1126/science.abb4688.

(45) Schultz, D. M.; Levesque, F.; DiRocco, D. A.; Reibarkh, M.; Ji, Y. N.; Joyce, L. A.; Dropinski, J. F.; Sheng, H. M.; Sherry, B. D.; Davies, I. W. Oxyfunctionalization of the Remote C-H Bonds of Aliphatic Amines by Decatungstate Photocatalysis. *Angewandte Chemie International Edition* **2017**, *56* (48), 15274-15278, http://dx.doi.org/10.1002/anie.201707537.

(46) Laudadio, G.; Govaerts, S.; Wang, Y.; Ravelli, D.; Koolman, H. F.; Fagnoni, M.; Djuric, S. W.; Noel, T. Selective C(sp(3))-H Aerobic Oxidation Enabled by Decatungstate Photocatalysis in Flow. *Angewandte Chemie International Edition* **2018**, *57* (15), 4078-4082, http://dx.doi.org/10.1002/anie.201800818.

(47) Arndtsen, B. A.; Bergman, R. G.; Mobley, T. A.; Peterson, T. H. Selective Intermolecular Carbon-Hydrogen Bond Activation by Synthetic Metal-Complexes in Homogeneous Solution. *Accounts Chem Res* **1995**, *28* (3), 154-162, http://dx.doi.org/10.1021/ar00051a009.

(48) Yin, L. X.; Liebscher, J. Carbon-carbon coupling reactions catalyzed by heterogeneous palladium catalysts. *Chem Rev* **2007**, *107* (1), 133-173, http://dx.doi.org/10.1021/cr0505674.

(49) Li, Q.; Yang, B.; Bjork, J.; Zhong, Q. G.; Ju, H. X.; Zhang, J. J.; Cao, N.; Shi, Z. L.; Zhang, H. M.; Ebeling, D.; et al. Hierarchical Dehydrogenation Reactions on a Copper Surface. *J Am Chem Soc* **2018**, *140* (19), 6076-6082, http://dx.doi.org/10.1021/jacs.7b12278.

(50) Gill, H. S.; Finger, I.; Bozidarevic, I.; Szydlo, F.; Scott, M. J. Preparation of alpha,beta-unsubstituted meso-arylbidipyrrins via metal-templated, oxidative coupling of dipyrrins. *New J Chem* **2005**, *29* (1), 68-71, http://dx.doi.org/10.1039/b412620c.

(51) Fan, Q. T.; Luy, J. N.; Liebold, M.; Greulich, K.; Zugermeier, M.; Sundermeyer, J.; Tonner, R.; Gottfried, J. M. Template-controlled on-surface synthesis of a lanthanide supernaphthalocyanine and its open-chain polycyanine counterpart. *Nat Commun* **2019**, *10*, http://dx.doi.org/10.1038/s41467-019-13030-7.

(52) Liu, X. S.; Matej, A.; Kratky, T.; Mendieta-Moreno, J. I.; Gunther, S.; Mutombo, P.; Decurtins, S.; Aschauer, U.; Repp, J.; Jelinek, P.; et al. Exploiting Cooperative Catalysis for the On-Surface Synthesis of Linear Heteroaromatic Polymers via Selective C-H Activation. *Angewandte Chemie International Edition* **2022**, *61* (5), http://dx.doi.org/10.1002/anie.202112798.

(53) Gerbeleu, N. V.; Arion, V. B.; Burgess, J. P. *Template synthesis of macrocyclic compounds*; John Wiley & Sons, 2008.

(54) Liu, Y.; Goebl, J.; Yin, Y. Templated synthesis of nanostructured materials. *Chem Soc Rev* **2013**, *42* (7), 2610-2653, http://dx.doi.org/10.1039/c2cs35369e.

(55) Martin, C. R. Template synthesis of electronically conductive polymer nanostructures. *Accounts Chem Res* **1995**, *28* (2), 61-68,

(56) Thompson, M. C.; Busch, D. H. Reactions of coordinated ligands. VI. Metal ion control in the synthesis of planar nickel (II) complexes of α-diketo-bis-mercaptoimines. *J Am Chem Soc* **1964**, *86* (2), 213-217,

(57) Sprafke, J. K.; Kondratuk, D. V.; Wykes, M.; Thompson, A. L.; Hoffmann, M.; Drevinskas, R.; Chen, W.-H.; Yong, C. K.; Kärnbratt, J.; Bullock, J. E.; et al. Belt-Shaped π-Systems: Relating Geometry to Electronic Structure in a Six-Porphyrin Nanoring. *J Am Chem Soc* **2011**, *133* (43), 17262-17273, http://dx.doi.org/10.1021/ja2045919.

(58) Binning, G.; Rohrer, H.; Gerber, C.; Weibel, E. Surface Studies by Scanning Tunneling Microscopy. *Phys Rev Lett* **1982**, *49* (1), 57-61, http://dx.doi.org/10.1103/PhysRevLett.49.57.

(59) Bardeen, J. Tunnelling from a Many-Particle Point of View. *Phys Rev Lett* **1961**, *6* (2), 57-&, http://dx.doi.org/10.1103/PhysRevLett.6.57.

(60) Tersoff, J.; Hamann, D. R. Theory of the Scanning Tunneling Microscope. *Phys Rev B* **1985**, *31* (2), 805-813, http://dx.doi.org/10.1103/PhysRevB.31.805.

(61) Selloni, A.; Carnevali, P.; Tosatti, E.; Chen, C. D. Voltage-Dependent Scanning-Tunneling Microscopy of a Crystal-Surface - Graphite. *Phys Rev B* **1985**, *31* (4), 2602-2605, http://dx.doi.org/10.1103/PhysRevB.31.2602.

(62) Hamers, R. J. Atomic-Resolution Surface Spectroscopy with the Scanning Tunneling Microscope. *Annu Rev Phys Chem* **1989**, *40*, 531-559, http://dx.doi.org/10.1146/annurev.pc.40.100189.002531.

(63) Binnig, G.; Quate, C. F.; Gerber, C. Atomic Force Microscope. *Phys Rev Lett* **1986**, *56* (9), 930-933, http://dx.doi.org/10.1103/PhysRevLett.56.930.

(64) Giessibl, F. J. Advances in atomic force microscopy. *Rev Mod Phys* **2003**, *75* (3), 949-983, http://dx.doi.org/10.1103/RevModPhys.75.949.

(65) Hamaker, H. C. The London—van der Waals attraction between spherical particles. *physica* **1937**, *4* (10), 1058-1072, http://dx.doi.org/10.1016/S0031-8914(37)80203-7.

(66) Jones, J. E. On the determination of molecular fields.—II. From the equation of state of a gas. *Proceedings of the Royal Society of London. Series A, Containing Papers of a Mathematical and Physical Character* **1924**, *106* (738), 463-477, http://dx.doi.org/10.1098/rspa.1924.0082.

(67) Pavliček, N. Scanning probe methods applied to molecular electronics. 2013.

(68) Cao, N. On-Surface Synthesis of Covalent-Bonded Molecular Nanostructures: Reaction Strategies and Refined Control. Technische Universität München, 2022.

(69) Martin, Y.; Williams, C. C.; Wickramasinghe, H. K. Atomic Force Microscope Force Mapping and Profiling on a Sub 100-a Scale. *J Appl Phys* **1987**, *61* (10), 4723-4729, http://dx.doi.org/10.1063/1.338807.

(70) Albrecht, T. R.; Grütter, P.; Horne, D.; Rugar, D. Frequency modulation detection using high-Q cantilevers for enhanced force microscope sensitivity. *J Appl Phys* **1991**, *69* (2), 668-673, http://dx.doi.org/10.1063/1.347347.

(71) Morita, S.; Giessibl, F. J.; Meyer, E.; Wiesendanger, R. *Noncontact Atomic Force Microscopy: Volume 3*; Springer, 2015.

(72) Giessibl, F. J. Atomic-Resolution of the Silicon (111)-(7x7) Surface by Atomic-Force Microscopy. *Science* **1995**, *267* (5194), 68-71, http://dx.doi.org/10.1126/science.267.5194.68.

(73) Giessibl, F. J. High-speed force sensor for force microscopy and profilometry utilizing a quartz tuning fork (vol 73, pg 3956, 1998). *Appl Phys Lett* **1999**, *74* (26), 4070-4070, http://dx.doi.org/10.1063/1.123265.

(74) Giessibl, F. J. Forces and frequency shifts in atomic-resolution dynamic-force microscopy. *Phys Rev B* **1997**, *56* (24), 16010, http://dx.doi.org/10.1103/PhysRevB.56.16010.

(75) Rieder, K. H.; Meyer, G.; Hla, S. W.; Moresco, F.; Braun, K. F.; Morgenstern, K.; Repp, J.; Foelsch, S.; Bartels, L. The scanning tunnelling microscope as an operative tool: doing physics and chemistry with single atoms and molecules. *Philos T R Soc A* **2004**, *362* (1819), 1207-1216, http://dx.doi.org/10.1098/rsta.2004.1373.

(76) Hembacher, S.; Giessibl, F. J.; Mannhart, J. Evaluation of a force sensor based on a quartz tuning fork for operation at low temperatures and ultrahigh vacuum. *Appl Surf Sci* **2002**, *188* (3-4), 445-449, http://dx.doi.org/10.1016/S0169-4332(01)00976-X.

(77) Rychen, J.; Ihn, T.; Studerus, P.; Herrmann, A.; Ensslin, K. A low-temperature dynamic mode scanning force microscope operating in high magnetic fields. *Rev Sci Instrum* **1999**, *70* (6), 2765-2768, http://dx.doi.org/10.1063/1.1149842.

(78) Gross, L.; Mohn, F.; Moll, N.; Liljeroth, P.; Meyer, G. The Chemical Structure of a Molecule Resolved by Atomic Force Microscopy. *Science* **2009**, *325* (5944), 1110-1114, http://dx.doi.org/10.1126/science.1176210.

(79) Moll, N.; Gross, L.; Mohn, F.; Curioni, A.; Meyer, G. The mechanisms underlying the enhanced resolution of atomic force microscopy with functionalized tips. *New J Phys* **2010**, *12*, http://dx.doi.org/10.1088/1367-2630/12/12/125020.

(80) Schuler, B.; Liu, W.; Tkatchenko, A.; Moll, N.; Meyer, G.; Mistry, A.; Fox, D.; Gross, L. Adsorption Geometry Determination of Single Molecules by Atomic Force Microscopy. *Phys Rev Lett* **2013**, *111* (10), http://dx.doi.org/10.1103/PhysRevLett.111.106103.

(81) Mohn, F.; Schuler, B.; Gross, L.; Meyer, G. Different tips for high-resolution atomic force microscopy and scanning tunneling microscopy of single molecules. *Appl Phys Lett* **2013**, *102* (7), http://dx.doi.org/10.1063/1.4793200.

(82) Bartels, L.; Meyer, G.; Rieder, K. H. Controlled vertical manipulation of single CO molecules with the scanning tunneling microscope: A route to chemical contrast. *Appl Phys Lett* **1997**, *71* (2), 213-215, http://dx.doi.org/10.1063/1.119503.

(83) Hertz, H. Ueber einen Einfluss des ultravioletten Lichtes auf die electrische Entladung. *Annalen der Physik* **1887**, *267* (8), 983-1000,

(84) Einstein, A. Über einen die Erzeugung und Verwandlung des Lichtes betreffenden heuristischen Gesichtspunkt. Albert Einstein-Gesellschaft: 1905.

(85) Alford, T. L.; Feldman, L. C.; Mayer, J. W. *Fundamentals of nanoscale film analysis*; Springer Science & Business Media, 2007.

(86) Carlson, T. Basic assumptions and recent developments in quantitative XPS. *Surface and Interface analysis* **1982**, *4* (4), 125-134,

(87) Jiang, L. Chemistry on noble metal surfaces: Towards covalently linked nanoarchitectures. Technische Universität München, 2017.

(88) Pörtner, M. Adsorption of phthalocyanine-complexes on hexagonal boron nitride templates. **2020**,

(89) Giessibl, F. J. High-speed force sensor for force microscopy and profilometry utilizing a quartz tuning fork. *Appl Phys Lett* **1998**, *73* (26), 3956-3958, http://dx.doi.org/10.1063/1.122948.

(90) Hellwig, R. *Alkyne-Based Nanostructures on Silver Substrates*; Springer, 2018.

(91) Giessibl, F. J. The qPlus sensor, a powerful core for the atomic force microscope. *Rev Sci Instrum* **2019**, *90* (1), http://dx.doi.org/10.1063/1.5052264.

(92) Horcas, I.; Fernandez, R.; Gomez-Rodriguez, J. M.; Colchero, J.; Gomez-Herrero, J.; Baro, A. M. WSXM: A software for scanning probe microscopy and a tool for nanotechnology. *Rev Sci Instrum* **2007**, *78* (1), http://dx.doi.org/10.1063/1.2432410.

(93) Riss, A. SpmImage Tycoon: Organize and analyze scanning probe microscopy data. *Journal of Open Source Software* **2022**, *7* (77), 4644, http://dx.doi.org/10.21105/joss.04644.

(94) Fairley, N.; Fernandez, V.; Richard-Plouet, M.; Guillot-Deudon, C.; Walton, J.; Smith, E.; Flahaut, D.; Greiner, M.; Biesinger, M.; Tougaard, S. Systematic and collaborative approach to problem solving using X-ray photoelectron spectroscopy. *Applied Surface Science Advances* **2021**, *5*, 100112, http://dx.doi.org/10.1016/j.apsadv.2021.100112.

(95) Guyard, N.; Skaltousnis, L.; Eisenbrand, G. *Indirubin, the red shade of indigo*; Life in Progress Edition, 2006.

(96) Konarev, D. V.; Khasanov, S. S.; Kuzmin, A. V.; Shestakov, A. F.; Otsuka, A.; Yamochi, H.; Saito, G.; Lyubovskaya, R. N. *cis*-Conformation of indigo in the coordination complex (indigo-*O,O*)(Cp*(Cr^{II})Cl). *Dalton T* **2016**, *45* (43), 17095-17099, http://dx.doi.org/10.1039/c6dt03545k.

(97) Guo, F. S.; Layfield, R. A. Strong direct exchange coupling and single-molecule magnetism in indigo-bridged lanthanide dimers. *Chem Commun* **2017**, *53* (21), 3130-3133, http://dx.doi.org/10.1039/c7cc01046j.

(98) Konarev, D. V.; Zorina, L. V.; Khasanov, S. S.; Shestakov, A. F.; Fatalov, A. M.; Otsuka, A.; Yamochi, H.; Kitagawa, H.; Lyubovskaya, R. N. Interligand Charge Transfer in a Complex of Deprotonated *cis*-Indigo Dianions and Tin(II) Phthalocyanine Radical Anions with Cp*Ir^{III}. *Inorg Chem* **2018**, *57* (2), 583-589, http://dx.doi.org/10.1021/acs.inorgchem.7b02351.

(99) Mondal, P.; Das, A.; Lahiri, G. K. The Electron-Rich {$Ru(acac)_2$} Directed Varying Configuration of the Deprotonated Indigo and Evidence for Its Bidirectional Noninnocence. *Inorg Chem* **2016**, *55* (3), 1208-1218, http://dx.doi.org/10.1021/acs.inorgchem.5b02409.

(100) Konarev, D. V.; Khasanov, S. S.; Shestakov, A. F.; Fatalov, A. M.; Batov, M. S.; Otsuka, A.; Yamochi, H.; Kitagawa, H.; Lyubovskaya, R. N. *cis*-Thioindigo (TI) – a new ligand with accessible radical anion and dianion states. Strong magnetic coupling in the {[TI-(μ_2-*O*),(μ-*O*)]Cp*Cr}$_2$ dimers. *Dalton T* **2017**, *46* (41), 14365-14372, http://dx.doi.org/10.1039/c7dt02878d.

(101) Chatterjee, M.; Ghosh, P.; Beyer, K.; Paretzki, A.; Fiedler, J.; Kaim, W.; Lahiri, G. K. Isomeric Diruthenium Complexes Bridged by Deprotonated Indigo in *cis* and *trans* Configuration. *Chem-Asian J* **2018**, *13* (1), 118-125, http://dx.doi.org/10.1002/asia.201701562.

(102) Beck, W.; Sunkel, K. Metal Complexes of Indigo and of Some Related Ligands. *Z Anorg Allg Chem* **2020**, *646* (4), 248-255, http://dx.doi.org/10.1002/zaac.201900363.

(103) Vorobyeva, E.; Lissel, F.; Salanne, M.; Lukatskaya, M. R. Bottom-Up Design of Configurable Oligomer-Derived Conducting Metallopolymers for High-Power Electrochemical Energy Storage. *Acs Nano* **2021**, *15* (10), 15422-15428, http://dx.doi.org/10.1021/acsnano.1c07339.

(104) Kaim, W.; Lahiri, G. K. The coordination potential of indigo, anthraquinone and related redox-active dyes. *Coordin Chem Rev* **2019**, *393*, 1-8, http://dx.doi.org/10.1016/j.ccr.2019.05.002.

(105) Glowacki, E. D.; Voss, G.; Sariciftci, N. S. 25th Anniversary Article: Progress in Chemistry and Applications of Functional Indigos for Organic Electronics. *Adv Mater* **2013**, *25* (47), 6783-6799, http://dx.doi.org/10.1002/adma.201302652.

(106) Honda, A.; Noda, K.; Tamaki, Y.; Miyamura, K. Surface Structures Formed by a Copper(II) Complex of Alkyl-Derivatized Indigo. *Materials* **2016**, *9* (10), 837, http://dx.doi.org/10.3390/ma9100837.

(107) Elsabawy, K. M.; Fallatah, A. M. Microwave assisted synthesis and molecular structure visualization of ultrahigh surface area Ni-6,6 '-dibromo-indigo coordinated polymeric MOFs stabilized via hydrogen bonding. *Inorg Chem Commun* **2018**, *92*, 78-83, http://dx.doi.org/10.1016/j.inoche.2018.04.011.

(108) Zhang, S. F.; Xiong, F.; He, Z.; Liang, Y.; Xue, J. R.; Jing, L. H.; Qin, D. B. Syntheses, structures, luminescent and gas adsorption properties of five new interpenetrated, 2D and 3D metal−organic frameworks based on a semi-rigid bis(imidazole)-carbazole ligand. *Polyhedron* **2015**, *102*, 401-409, http://dx.doi.org/10.1016/j.poly.2015.08.040.

(109) Wang, F. Q.; Wang, C. M.; Yu, Z. C.; Xu, K. H.; Li, X. Y.; Fu, Y. Y. Two multifunctional Mn(II) metal-organic frameworks: Synthesis, structures and applications as photocatalysis and luminescent sensor. *Polyhedron* **2016**, *105*, 49-55, http://dx.doi.org/10.1016/j.poly.2015.11.043.

(110) Yan, Z. H.; Li, X. Y.; Liu, L. W.; Yu, S. Q.; Wang, X. P.; Sun, D. Single-Crystal to Single-Crystal Phase Transition and Segmented Thermochromic Luminescence in a Dynamic 3D Interpenetrated Ag^{I} Coordination Network. *Inorg Chem* **2016**, *55* (3), 1096-1101, http://dx.doi.org/10.1021/acs.inorgchem.5b02200.

(111) Talham, D. R.; Meisel, M. W. Thin films of coordination polymer magnets. *Chem Soc Rev* **2011**, *40* (6), 3356-3365, 10.1039/C1CS15015D http://dx.doi.org/10.1039/C1CS15015D.

(112) Heim, D.; Écija, D.; Seufert, K.; Auwärter, W.; Aurisicchio, C.; Fabbro, C.; Bonifazi, D.; Barth, J. V. Self-Assembly of Flexible One-Dimensional Coordination Polymers on Metal Surfaces. *J Am Chem Soc* **2010**, *132* (19), 6783-6790, http://dx.doi.org/10.1021/ja1010527.

(113) Pham, T. A.; Song, F.; Alberti, M. N.; Nguyen, M.-T.; Trapp, N.; Thilgen, C.; Diederich, F.; Stöhr, M. Heat-induced formation of one-dimensional coordination polymers on Au(111): an STM study. *Chem Commun* **2015**, *51* (77), 14473-14476, 10.1039/C5CC04940G http://dx.doi.org/10.1039/C5CC04940G.

(114) Knor, M.; Gao, H.-Y.; Amirjalayer, S.; Studer, A.; Gao, H.; Du, S.; Fuchs, H. Stereoselective formation of coordination polymers with 1,4-diaminonaphthalene on various Cu substrates. *Chem Commun* **2015**, *51* (54), 10854-10857, 10.1039/C5CC03130C http://dx.doi.org/10.1039/C5CC03130C.

(115) Papageorgiou, A. C.; Li, J.; Oh, S. C.; Zhang, B.; Sağlam, Ö.; Guo, Y.; Reichert, J.; Marco, A. B.; Cortizo-Lacalle, D.; Mateo-Alonso, A.; et al. Tuning the ease of formation of On-Surface metal-adatom coordination polymers featuring diketones. *Nanoscale* **2018**, *10* (20), 9561-9568, 10.1039/C8NR02537A http://dx.doi.org/10.1039/C8NR02537A.

(116) Liu, J.; Abel, M.; Lin, N. On-Surface Synthesis: A New Route Realizing Single-Layer Conjugated Metal–Organic Structures. *The Journal of Physical Chemistry Letters* **2022**, *13* (5), 1356-1365, http://dx.doi.org/10.1021/acs.jpclett.1c04134.

(117) Yu, X.; Sun, Q.; Liu, M.; Du, W.; Liu, Y.; Cai, L.; Zha, Z.; Pan, J.; Kang, F.; Gao, W.; et al. Lattice-Directed Selective Synthesis of Acetylenic and Diacetylenic Organometallic

Polyynes. *Chemistry of Materials* **2022**, *34* (4), 1770-1777, http://dx.doi.org/10.1021/acs.chemmater.1c04015.

(118) Song, L.; Yang, B.; Liu, F.; Niu, K.; Han, Y.; Wang, J.; Zheng, Y.; Zhang, H.; Li, Q.; Chi, L. Synthesis of Two-Dimensional Metal–Organic Frameworks via Dehydrogenation Reactions on a Cu(111) Surface. *The Journal of Physical Chemistry C* **2020**, *124* (23), 12390-12396, http://dx.doi.org/10.1021/acs.jpcc.0c00931.

(119) Santhini, V. M.; Wäckerlin, C.; Cahlík, A.; Ondráček, M.; Pascal, S.; Matěj, A.; Stetsovych, O.; Mutombo, P.; Lazar, P.; Siri, O.; et al. 1D Coordination π–d Conjugated Polymers with Distinct Structures Defined by the Choice of the Transition Metal: Towards a New Class of Antiaromatic Macrocycles. *Angewandte Chemie International Edition* **2021**, *60* (1), 439-445, http://dx.doi.org/10.1002/anie.202011462.

(120) Frezza, F.; Schiller, F.; Cahlík, A.; Ortega, J. E.; Barth, J. V.; Arnau, A.; Blanco-Rey, M.; Jelínek, P.; Corso, M.; Piquero-Zulaica, I. Electronic band structure of 1D π–d hybridized narrow-gap metal–organic polymers. *Nanoscale* **2023**, *15* (5), 2285-2291, 10.1039/D2NR05828F http://dx.doi.org/10.1039/D2NR05828F.

(121) Liu, J.; Gao, Y.; Wang, T.; Xue, Q.; Hua, M.; Wang, Y.; Huang, L.; Lin, N. Collective Spin Manipulation in Antiferroelastic Spin-Crossover Metallo-Supramolecular Chains. *Acs Nano* **2020**, *14* (9), 11283-11293, http://dx.doi.org/10.1021/acsnano.0c03163.

(122) Mallada, B.; Błoński, P.; Langer, R.; Jelínek, P.; Otyepka, M.; de la Torre, B. On-Surface Synthesis of One-Dimensional Coordination Polymers with Tailored Magnetic Anisotropy. *ACS Applied Materials & Interfaces* **2021**, *13* (27), 32393-32401, http://dx.doi.org/10.1021/acsami.1c04693.

(123) Wäckerlin, C.; Cahlík, A.; Goikoetxea, J.; Stetsovych, O.; Medvedeva, D.; Redondo, J.; Švec, M.; Delley, B.; Ondráček, M.; Pinar, A.; et al. Role of the Magnetic Anisotropy in Atomic-Spin Sensing of 1D Molecular Chains. *Acs Nano* **2022**, *16* (10), 16402-16413, http://dx.doi.org/10.1021/acsnano.2c05609.

(124) Miliani, C.; Romani, A.; Favaro, G. A spectrophotometric and fluorimetric study of some anthraquinoid and indigoid colorants used in artistic paintings. *Spectrochim Acta A* **1998**, *54* (4), 581-588, http://dx.doi.org/10.1016/S1386-1425(97)00240-0.

(125) Yamazaki, S.; Sobolewski, A. L.; Domcke, W. Molecular mechanisms of the photostability of indigo. *Phys Chem Chem Phys* **2011**, *13* (4), 1618-1628, http://dx.doi.org/10.1039/c0cp01901a.

(126) Weinstein, J.; Wyman, G. M. Spectroscopic Studies on Dyes .2. The Structure of *N,N'*-Dimethylindigo. *J Am Chem Soc* **1956**, *78* (16), 4007-4010, http://dx.doi.org/10.1021/ja01597a038.

(127) de Melo, J. S. S.; Rondao, R.; Burrows, H. D.; Melo, M. J.; Navaratnam, S.; Edge, R.; Voss, G. Spectral and photophysical studies of substituted indigo derivatives in their keto forms. *Chemphyschem* **2006**, *7* (11), 2303-2311, http://dx.doi.org/10.1002/cphc.200600203.

(128) Wyman, G. M. The *cis-trans* Isomerization of Conjugated Compounds. *Chem Rev* **1955**, *55* (4), 625-657, http://dx.doi.org/10.1021/cr50004a001.

(129) Giuliano, C. R.; Hess, L. D.; Margerum, J. D. *cis-trans* Isomerization and Pulsed Laser Studies of Substituted Indigo Dyes. *J Am Chem Soc* **1968**, *90* (3), 587-&, http://dx.doi.org/10.1021/ja01005a600.

(130) Brode, W. R.; Pearson, E. G.; Wyman, G. M. The Relation between the Absorption Spectra and the Chemical Constitution of Dyes. XXVI. *cis-trans* Isomerism and Hydrogen Bonding in Indigo Dyes. *J Am Chem Soc* **1954**, *76* (4), 1034-1036, http://dx.doi.org/10.1021/ja01633a033.

(131) Moreno, M.; Ortiz-Sanchez, J. M.; Gelabert, R.; Lluch, J. M. A theoretical study of the photochemistry of indigo in its neutral and dianionic (leucoindigo) forms. *Phys Chem Chem Phys* **2013**, *15* (46), 20236-20246, http://dx.doi.org/10.1039/c3cp52763h.

(132) Haggmark, M. R.; Gate, G.; Boldissar, S.; Berenbeim, J.; Sobolewski, A. L.; de Vries, M. S. Evidence for competing proton-transfer and hydrogen-transfer reactions in the S_1 state of indigo. *Chem Phys* **2018**, *515*, 535-542, http://dx.doi.org/10.1016/j.chemphys.2018.09.027.

(133) Pina, J.; Sarmento, D.; Accoto, M.; Gentili, P. L.; Vaccaro, L.; Galvao, A.; de Melo, J. S. S. Excited-State Proton Transfer in Indigo. *J Phys Chem B* **2017**, *121* (10), 2308-2318, http://dx.doi.org/10.1021/acs.jpcb.6b11020.

(134) Nobre, D. C.; Cunha, C.; Porciello, A.; Valentini, F.; Marrocchi, A.; Vaccaro, L.; Galvao, A. M.; de Melo, J. S. S. Photoresponsive *N,N′*-disubstituted indigo derivatives. *Dyes Pigments* **2020**, *176*, http://dx.doi.org/10.1016/j.dyepig.2020.108197.

(135) Budzak, S.; Jovaisaite, J.; Huang, C. Y.; Baronas, P.; Tulaite, K.; Jursenas, S.; Jacquemin, D.; Hecht, S. Mechanistic Insights into the Photoisomerization of *N,N′*-Disubstituted Indigos. *Chem-Eur J* **2022**, *28* (26), http://dx.doi.org/10.1002/chem.202200496.

(136) Setsune, J.; Wakemoto, H.; Matsukawa, K.; Ishihara, S.; Yamamoto, R.; Kitao, T. Synthesis and *cis*-to-*trans* Isomerization of *N,N′*-Diacyl Derivatives of Indigotin. *J Chem Soc Chem Comm* **1982**, (17), 1022-1023, http://dx.doi.org/10.1039/c39820001022.

(137) Sueishi, Y.; Ohtani, K.; Nishimura, N. The Thermal *cis*-to-*trans* Isomerization of *N,N′*-Diacylindigos - Kinetic Pressure, Solvent, and Substituent Effects. *B Chem Soc Jpn* **1985**, *58* (3), 810-814, http://dx.doi.org/10.1246/bcsj.58.810.

(138) Miehe, G.; Susse, P.; Kupcik, V.; Egert, E.; Nieger, M.; Kunz, G.; Gerke, R.; Knieriem, B.; Niemeyer, M.; Luttke, W. Light-Absorption as Well as Crystal and Molecular-Structure of *N,N′*-Dimethylindigo: An Example of the Use of Synchrotron Radiation. *Angewandte Chemie International Edition* **1991**, *30* (8), 964-967, http://dx.doi.org/10.1002/anie.199109641.

(139) Farka, D.; Scharber, M.; Glowacki, E. D.; Sariciftci, N. S. Reversible Photochemical Isomerization of *N,N′*-Di(t-butoxycarbonyl)indigos. *J Phys Chem A* **2015**, *119* (15), 3563-3568, http://dx.doi.org/10.1021/jp512346z.

(140) Huang, C. Y.; Bonasera, A.; Hristov, L.; Garmshausen, Y.; Schmidt, B. M.; Jacquemin, D.; Hecht, S. *N,N′*-Disubstituted Indigos as Readily Available Red-Light Photoswitches with Tunable Thermal Half-Lives. *J Am Chem Soc* **2017**, *139* (42), 15205-15211, http://dx.doi.org/10.1021/jacs.7b08726.

(141) Petermayer, C.; Dube, H. Indigoid Photoswitches: Visible Light Responsive Molecular Tools. *Accounts Chem Res* **2018**, *51* (5), 1153-1163, http://dx.doi.org/10.1021/acs.accounts.7b00638.

(142) Haucke, G.; Graness, G. Thermal-Isomerization of Indigo. *Angewandte Chemie International Edition* **1995**, *34* (1), 67-68, http://dx.doi.org/10.1002/anie.199500671.

(143) Munshi, M. U.; Martens, J.; Berden, G.; Oomens, J. Protoisomerization of Indigo and Isoindigo Dyes Confirmed by Gas-Phase Infrared Ion Spectroscopy. *J Phys Chem A* **2019**, *123* (38), 8226-8233, http://dx.doi.org/10.1021/acs.jpca.9b06858.

(144) El-Mansy, M. A. M.; Yahia, I. S.; Alfaify, S. Conformational and Vibrational Properties of Indigo Dye: DFT Approach. *Org. Opto-Elect.* **2015**, *1*, 39–45,

(145) Klappenberger, F.; Zhang, Y. Q.; Bjork, J.; Klyatskaya, S.; Ruben, M.; Barth, J. V. On-Surface Synthesis of Carbon-Based Scaffolds and Nanomaterials Using Terminal Alkynes. *Accounts Chem Res* **2015**, *48* (7), 2140-2150, http://dx.doi.org/10.1021/acs.accounts.5b00174.

(146) Barth, J. V.; Costantini, G.; Kern, K. Engineering atomic and molecular nanostructures at surfaces. *Nature* **2005**, *437* (7059), 671-679, http://dx.doi.org/10.1038/nature04166.

(147) Skomski, D.; Tempas, C. D.; Bukowski, G. S.; Smith, K. A.; Tait, S. L. Redox-active On-Surface polymerization of single-site divalent cations from pure metals by a ketone-functionalized phenanthroline. *J Chem Phys* **2015**, *142* (10), http://dx.doi.org/10.1063/1.4906894.

(148) Koudia, M.; Nardi, E.; Siri, O.; Abel, M. On-Surface synthesis of covalent coordination polymers on micrometer scale. *Nano Res* **2017**, *10* (3), 933-940, http://dx.doi.org/10.1007/s12274-016-1352-y.

(149) Lin, N.; Stepanow, S.; Ruben, M.; Barth, J. V. Surface-Confined Supramolecular Coordination Chemistry. *Top Curr Chem* **2009**, *287*, 1-44, http://dx.doi.org/10.1007/128_2008_150.

(150) Barth, J. V. Fresh perspectives for surface coordination chemistry. *Surf Sci* **2009**, *603* (10-12), 1533-1541, http://dx.doi.org/10.1016/j.susc.2008.09.049.

(151) Stepanow, S.; Lin, N.; Barth, J. V. Modular assembly of low-dimensional coordination architectures on metal surfaces. *J Phys-Condens Mat* **2008**, *20* (18), http://dx.doi.org/10.1088/0953-8984/20/18/184002.

(152) Dong, L.; Gao, Z. A.; Lin, N. Self-assembly of metal-organic coordination structures on surfaces. *Prog Surf Sci* **2016**, *91* (3), 101-135, http://dx.doi.org/10.1016/j.progsurf.2016.08.001.

(153) Villagómez, C. J.; Buendía, F.; Paz-Borbón, L. O.; Fuentes, B.; Zambelli, T.; Bouju, X. Surface Vacancy Generation by STM Tunneling Electrons in the Presence of Indigo Molecules on Cu(111). *The Journal of Physical Chemistry C* **2022**, *126* (33), 14103-14115, http://dx.doi.org/10.1021/acs.jpcc.2c01686.

(154) Villagomez, C. J.; Guillermet, O.; Goudeau, S.; Ample, F.; Xu, H.; Coudret, C.; Bouju, X.; Zambelli, T.; Gauthier, S. Self-assembly of enantiopure domains: The case of indigo on

Cu(111). *The Journal of Chemical Physics* **2010**, *132* (7), 074705, http://dx.doi.org/10.1063/1.3314725.

(155) Jiang, L.; Papageorgiou, A. C.; Oh, S. C.; Sağlam, Ö.; Reichert, J.; Duncan, D. A.; Zhang, Y.-Q.; Klappenberger, F.; Guo, Y.; Allegretti, F.; et al. Synthesis of Pyrene-Fused Pyrazaacenes on Metal Surfaces: Toward One-Dimensional Conjugated Nanostructures. *Acs Nano* **2016**, *10* (1), 1033-1041, http://dx.doi.org/10.1021/acsnano.5b06340.

(156) Papageorgiou, A. C.; Diller, K.; Fischer, S.; Allegretti, F.; Klappenberger, F.; Oh, S. C.; Sağlam, Ö.; Reichert, J.; Wiengarten, A.; Seufert, K.; et al. In Vacuo Porphyrin Metalation on Ag(111) via Chemical Vapor Deposition of $Ru_3(CO)_{12}$: Mechanistic Insights. *The Journal of Physical Chemistry C* **2016**, *120* (16), 8751-8758, http://dx.doi.org/10.1021/acs.jpcc.6b01457.

(157) Li, Q.; Yang, B.; Björk, J.; Zhong, Q.; Ju, H.; Zhang, J.; Cao, N.; Shi, Z.; Zhang, H.; Ebeling, D.; et al. Hierarchical Dehydrogenation Reactions on a Copper Surface. *J Am Chem Soc* **2018**, *140* (19), 6076-6082, http://dx.doi.org/10.1021/jacs.7b12278.

(158) Wang, T.; Lv, H. F.; Feng, L.; Tao, Z. J.; Huang, J. M.; Fan, Q. T.; Wu, X. J.; Zhu, J. F. Unravelling the Mechanism of Glaser Coupling Reaction on Ag(111) and Cu(111) Surfaces: a Case for Halogen Substituted Terminal Alkyne. *J Phys Chem C* **2018**, *122* (26), 14537-14545, http://dx.doi.org/10.1021/acs.jpcc.8b02893.

(159) Sánchez-Grande, A.; Urgel, J. I.; Cahlík, A.; Santos, J.; Edalatmanesh, S.; Rodríguez-Sánchez, E.; Lauwaet, K.; Mutombo, P.; Nachtigallová, D.; Nieman, R.; et al. Diradical Organic One-Dimensional Polymers Synthesized on a Metallic Surface. *Angewandte Chemie International Edition* **2020**, *59* (40), 17594-17599, 10.1002/anie.202006276 http://dx.doi.org/https://doi.org/10.1002/anie.202006276.

(160) Liu, J.; Chen, Q.; He, Q.; Zhang, Y.; Fu, X.; Wang, Y.; Zhao, D.; Chen, W.; Xu, G. Q.; Wu, K. Bromine adatom promoted C–H bond activation in terminal alkynes at room temperature on Ag(111). *Phys Chem Chem Phys* **2018**, *20* (16), 11081-11088, 10.1039/C7CP07972A http://dx.doi.org/10.1039/C7CP07972A.

(161) Lu, J.; Bao, D.-L.; Dong, H.; Qian, K.; Zhang, S.; Liu, J.; Zhang, Y.; Lin, X.; Du, S.-X.; Hu, W.; et al. Construction of Two-Dimensional Chiral Networks through Atomic Bromine on Surfaces. *The Journal of Physical Chemistry Letters* **2017**, *8* (2), 326-331, http://dx.doi.org/10.1021/acs.jpclett.6b02680.

(162) Tait, S. L.; Wang, Y.; Costantini, G.; Lin, N.; Baraldi, A.; Esch, F.; Petaccia, L.; Lizzit, S.; Kern, K. Metal−Organic Coordination Interactions in Fe−Terephthalic Acid Networks on Cu(100). *J Am Chem Soc* **2008**, *130* (6), 2108-2113, http://dx.doi.org/10.1021/ja0778186.

(163) Gottfried, J. M.; Flechtner, K.; Kretschmann, A.; Lukasczyk, T.; Steinruck, H. P. Direct synthesis of a metalloporphyrin complex on a surface. *J Am Chem Soc* **2006**, *128* (17), 5644-5645, http://dx.doi.org/10.1021/ja0610333.

(164) Hapala, P.; Kichin, G.; Wagner, C.; Tautz, F. S.; Temirov, R.; Jelínek, P. Mechanism of high-resolution STM/AFM imaging with functionalized tips. *Phys Rev B* **2014**, *90* (8), 085421, http://dx.doi.org/10.1103/PhysRevB.90.085421.

(165) Hapala, P.; Temirov, R.; Tautz, F. S.; Jelínek, P. Origin of High-Resolution IETS-STM Images of Organic Molecules with Functionalized Tips. *Phys Rev Lett* **2014**, *113* (22), 226101, http://dx.doi.org/10.1103/PhysRevLett.113.226101.

(166) Auwarter, W.; Ecija, D.; Klappenberger, F.; Barth, J. V. Porphyrins at interfaces. *Nat Chem* **2015**, *7* (2), 105-120, http://dx.doi.org/10.1038/nchem.2159.

(167) Ricchelli, F. Photophysical Properties of Porphyrins in Biological-Membranes. *J Photoch Photobio B* **1995**, *29* (2-3), 109-118, http://dx.doi.org/10.1016/1011-1344(95)07155-U.

(168) Furhop, J. H.; Kadish, K. M.; Davis, D. G. Redox behavior of metallo oxtaethylporhyrins. *J Am Chem Soc* **1973**, *95* (16), 5140-5147,

(169) Diller, K.; Papageorgiou, A. C.; Klappenberger, F.; Allegretti, F.; Barth, J. V.; Auwarter, W. In vacuo interfacial tetrapyrrole metallation. *Chem Soc Rev* **2016**, *45* (6), 1629-1656, http://dx.doi.org/10.1039/c5cs00207a.

(170) Xu, W.; Nagata, Y.; Kumagai, N. TEtraQuinolines: A Missing Link in the Family of Porphyrinoid Macrocycles. *J Am Chem Soc* **2023**, http://dx.doi.org/10.1021/jacs.2c12582.

(171) Szyszko, B.; Bialek, M. J.; Pacholska-Dudziak, E.; Latos-Grazynski, L. Flexible Porphyrinoids. *Chem Rev* **2017**, *117* (4), 2839-2909, http://dx.doi.org/10.1021/acs.chemrev.6b00423.

(172) Kim, J.; Oh, J.; Osuka, A.; Kim, D. Porphyrinoids, a unique platform for exploring excited-state aromaticity. *Chem Soc Rev* **2022**, *51* (1), 268-292, http://dx.doi.org/10.1039/d1cs00742d.

(173) Senge, M. O.; Sergeeva, N. N.; Hale, K. J. Classic highlights in porphyrin and porphyrinoid total synthesis and biosynthesis. *Chem Soc Rev* **2021**, *50* (7), 4730-4789, http://dx.doi.org/10.1039/c7cs00719a.

(174) Vogel, E.; Kocher, M.; Schmickler, H.; Lex, J. Porphycene - a Novel Porphin Isomer. *Angewandte Chemie International Edition* **1986**, *25* (3), 257-259, http://dx.doi.org/10.1002/anie.198602571.

(175) Anguera, G.; Sanchez-Garcia, D. Porphycenes and Related Isomers: Synthetic Aspects. *Chem Rev* **2017**, *117* (4), 2481-2516, http://dx.doi.org/10.1021/acs.chemrev.6b00345.

(176) Tsuda, A.; Osuka, A. Fully conjugated porphyrin tapes with electronic absorption bands that reach into infrared. *Science* **2001**, *293* (5527), 79-82, http://dx.doi.org/10.1126/science.1059552.

(177) Cho, H. S.; Jeong, D. H.; Cho, S.; Kim, D.; Matsuzaki, Y.; Tanaka, K.; Tsuda, A.; Osuka, A. Photophysical properties of porphyrin tapes. *J Am Chem Soc* **2002**, *124* (49), 14642-14654, http://dx.doi.org/10.1021/ja020826w.

(178) McEwan, K. J.; Fleitz, P. A.; Rogers, J. E.; Slagle, J. E.; McLean, D. G.; Akdas, H.; Katterle, M.; Blake, I. M.; Anderson, H. L. Reverse saturable absorption in the near-infrared by fused porphyrin dimers. *Adv Mater* **2004**, *16* (21), 1933-+, http://dx.doi.org/10.1002/adma.200400492.

(179) Sedghi, G.; Esdaile, L. J.; Anderson, H. L.; Martin, S.; Bethell, D.; Higgins, S. J.; Nichols, R. J. Comparison of the Conductance of Three Types of Porphyrin-Based Molecular Wires: beta,meso,beta-Fused Tapes, meso-Butadiyne-Linked and Twisted meso-meso Linked Oligomers. *Adv Mater* **2012**, *24* (5), 653-+, http://dx.doi.org/10.1002/adma.201103109.

(180) Tanaka, T.; Osuka, A. Triply Linked Porphyrinoids. *Chem-Eur J* **2018**, *24* (65), 17188-17200, http://dx.doi.org/10.1002/chem.201802810.

(181) Hiroto, S.; Furukawa, K.; Shinokubo, H.; Osuka, A. Synthesis and biradicaloid character of doubly linked corrole dimers. *J Am Chem Soc* **2006**, *128* (38), 12380-12381, http://dx.doi.org/10.1021/ja062654z.

(182) Barata, J. F. B.; Silva, A. M. G.; Neves, M. G. P. M. S.; Tome, A. C.; Silva, A. M. S.; Cavaleiro, J. A. S. beta,beta '-Corrole dimers. *Tetrahedron Lett* **2006**, *47* (46), 8171-8174, http://dx.doi.org/10.1016/j.tetlet.2006.09.026.

(183) Bhowmik, S.; Kosa, M.; Mizrahi, A.; Fridman, N.; Saphier, M.; Stanger, A.; Gross, Z. The Planar Cyclooctatetraene Bridge in Bis-Metallic Macrocycles: Isolating or Conjugating? *Inorg Chem* **2017**, *56* (4), 2287-2296, http://dx.doi.org/10.1021/acs.inorgchem.6b02944.

(184) Ooi, S.; Tanaka, T.; Ikeue, T.; Yamasumi, K.; Ueta, K.; Shimizu, D.; Ishida, M.; Furuta, H.; Osuka, A. Bis-copper(II) Complex of Triply-linked Corrole Dimer and Its Dication. *Chem-Asian J* **2019**, *14* (10), 1771-1776, http://dx.doi.org/10.1002/asia.201801467.

(185) Mizrahi, A.; Bhowmik, S.; Manna, A. K.; Sinha, W.; Kumar, A.; Saphier, M.; Mahammed, A.; Patra, M.; Fridman, N.; Zilbermann, I.; et al. Electronic Coupling and Electrocatalysis in Redox Active Fused Iron Corroles. *Inorg Chem* **2022**, *61* (51), 20725-20733, http://dx.doi.org/10.1021/acs.inorgchem.2c01389.

(186) Okuda, Y.; Fukui, N.; Kim, J.; Kim, T.; Jiang, H. W.; Copley, G.; Kitano, M.; Kim, D.; Osuka, A. A meso-meso - - Triply Linked Subporphyrin Dimer. *Angewandte Chemie International Edition* **2017**, *56* (40), 12317-12321, http://dx.doi.org/10.1002/anie.201707123.

(187) Tanaka, T.; Aratani, N.; Lim, J. M.; Kim, K. S.; Kim, D.; Osuka, A. Porphyrin-hexaphyrin hybrid tapes. *Chem Sci* **2011**, *2* (7), 1414-1418, http://dx.doi.org/10.1039/c1sc00228g.

(188) Mori, H.; Tanaka, T.; Lee, S.; Lim, J. M.; Kim, D.; Osuka, A. meso-meso Linked Porphyrin-[26]Hexaphyrin-Porphyrin Hybrid Arrays and Their Triply Linked Tapes Exhibiting Strong Absorption Bands in the NIR Region. *J Am Chem Soc* **2015**, *137* (5), 2097-2106, http://dx.doi.org/10.1021/ja5130034.

(189) Mateo, L. M.; Sun, Q.; Liu, S. X.; Bergkamp, J. J.; Eimre, K.; Pignedoli, C. A.; Ruffieux, P.; Decurtins, S.; Bottari, G.; Fasel, R.; et al. On-Surface Synthesis and Characterization of Triply Fused Porphyrin-Graphene Nanoribbon Hybrids. *Angewandte Chemie International Edition* **2020**, *59* (3), 1334-1339, http://dx.doi.org/10.1002/anie.201913024.

(190) Mateo, L. M.; Sun, Q.; Eimre, K.; Pignedoli, C. A.; Torres, T.; Fasel, R.; Bottari, G. On-surface synthesis of singly and doubly porphyrin-capped graphene nanoribbon segments. *Chem Sci* **2021**, *12* (1), 247-252, http://dx.doi.org/10.1039/d0sc04316h.

(191) Chen, Q.; Brambilla, L.; Daukiya, L.; Mali, K. S.; De Feyter, S.; Tommasini, M.; Mullen, K.; Narita, A. Synthesis of Triply Fused Porphyrin-Nanographene Conjugates. *Angewandte*

Chemie International Edition **2018**, *57* (35), 11233-11237, http://dx.doi.org/10.1002/anie.201805063.

(192) Piantek, M.; Serrate, D.; Moro-Lagares, M.; Algarabel, P.; Pascual, J. I.; Ibarra, M. R. Manganese Phthalocyanine Derivatives Synthesized by On-Surface Cyclotetramerization. *J Phys Chem C* **2014**, *118* (31), 17895-17899, http://dx.doi.org/10.1021/jp506652j.

(193) Dominguez-Celorrio, A.; Garcia-Fernandez, C.; Quiroga, S.; Koval, P.; Langlais, V.; Pena, D.; Sanchez-Portal, D.; Serrate, D.; Lobo-Checa, J. On-surface synthesis of Mn-phthalocyanines with optically active ligands. *Nanoscale* **2022**, *14* (22), 8069-8077, http://dx.doi.org/10.1039/d2nr00721e.

(194) Koudia, M.; Abel, M. Step-by-step on-surface synthesis: from manganese phthalocyanines to their polymeric form. *Chem Commun* **2014**, *50* (62), 8565-8567, http://dx.doi.org/10.1039/c4cc02792b.

(195) Zhao, Y.; Yuan, B. K.; Li, C.; Zhang, P. F.; Mai, Y. Y.; Guan, D. D.; Li, Y. Y.; Zheng, H.; Liu, C. H.; Wang, S. Y.; et al. On-Surface Synthesis of Iron Phthalocyanine Using Metal-Organic Coordination Templates. *Chemphyschem* **2019**, *20* (18), 2394-2397, http://dx.doi.org/10.1002/cphc.201900238.

(196) Abel, M.; Clair, S.; Ourdjini, O.; Mossoyan, M.; Porte, L. Single Layer of Polymeric Fe-Phthalocyanine: An Organometallic Sheet on Metal and Thin Insulating Film. *J Am Chem Soc* **2011**, *133* (5), 1203-1205, http://dx.doi.org/10.1021/ja108628r.

(197) Sun, Q.; Mateo, L. M.; Robles, R.; Lorente, N.; Ruffieux, P.; Bottari, G.; Torres, T.; Fasel, R. Bottom-up Fabrication and Atomic-Scale Characterization of Triply Linked, Laterally pi-Extended Porphyrin Nanotapes**. *Angewandte Chemie International Edition* **2021**, *60* (29), 16208-16214, http://dx.doi.org/10.1002/anie.202105350.

(198) Hawn, D. D.; Dekoven, B. M. Deconvolution as a Correction for Photoelectron Inelastic Energy-Losses in the Core Level Xps Spectra of Iron-Oxides. *Surface and Interface Analysis* **1987**, *10* (2-3), 63-74, http://dx.doi.org/10.1002/sia.740100203.

(199) Hua, M. Q.; Xia, B. W.; Wang, M.; Li, E.; Liu, J.; Wu, T. H.; Wang, Y. F.; Li, R. N.; Ding, H. H.; Hu, J.; et al. Highly Degenerate Ground States in a Frustrated Antiferromagnetic Kagome Lattice in a Two-Dimensional Metal-Organic Framework. *J Phys Chem Lett* **2021**, *12* (15), 3733-3739, http://dx.doi.org/10.1021/acs.jpclett.1c00598.

(200) Lawrence, J.; Berdonces-Layunta, A.; Edalatmanesh, S.; Castro-Esteban, J.; Wang, T.; Jimenez-Martin, A.; de la Torre, B.; Castrillo-Bodero, R.; Angulo-Portugal, P.; Mohammed, M. S. G.; et al. Circumventing the stability problems of graphene nanoribbon zigzag edges. *Nat Chem* **2022**, *14* (12), 1451-+, http://dx.doi.org/10.1038/s41557-022-01042-8.

(201) Chen, P.; Fan, D.; Selloni, A.; Carter, E. A.; Arnold, C. B.; Zhang, Y.; Gross, A. S.; Chelikowsky, J. R.; Yao, N. Observation of electron orbital signatures of single atoms within metal-phthalocyanines using atomic force microscopy. *Nat Commun* **2023**, *14* (1), 1460, http://dx.doi.org/10.1038/s41467-023-37023-9.

(202) Blyholder, G. Molecular Orbital View of Chemisorbed Carbon Monoxide. *The Journal of Physical Chemistry* **1964**, *68* (10), 2772-2777, http://dx.doi.org/10.1021/j100792a006.

(203) Sun, Q.; Mateo, L. M.; Robles, R.; Ruffieux, P.; Bottari, G.; Torres, T.; Fasel, R.; Lorente, N. Magnetic Interplay between pi-Electrons of Open-Shell Porphyrins and d-Electrons of Their Central Transition Metal Ions. *Adv Sci* **2022**, *9* (19), http://dx.doi.org/10.1002/advs.202105906.

(204) Wiengarten, A.; Lloyd, J. A.; Seufert, K.; Reichert, J.; Auwärter, W.; Han, R.; Duncan, D. A.; Allegretti, F.; Fischer, S.; Oh, S. C.; et al. Surface-Assisted Cyclodehydrogenation; Break the Symmetry, Enhance the Selectivity. *Chemistry - A European Journal* **2015**, *21* (35), 12285-12290, http://dx.doi.org/10.1002/chem.201502001.

(205) Liu, M. Z.; Liu, M. X.; She, L. M.; Zha, Z. Q.; Pan, J. L.; Li, S. C.; Li, T.; He, Y. Y.; Cai, Z. Y.; Wang, J. B.; et al. Graphene-like nanoribbons periodically embedded with four- and eight-membered rings. *Nat Commun* **2017**, *8*, http://dx.doi.org/10.1038/ncomms14924.

(206) Roland, C. D.; Li, H.; Abboud, K. A.; Wagener, K. B.; Veige, A. S. Cyclic polymers from alkynes. *Nat Chem* **2016**, *8* (8), 791-796, http://dx.doi.org/10.1038/nchem.2516.

(207) Takahashi, S.; Matsumoto, T.; Hollamby, M. J.; Miyasaka, H.; Vacha, M.; Sotome, H.; Yagai, S. Impact of Ring-Closing on the Photophysical Properties of One-Dimensional π-Conjugated Molecular Aggregate. *J Am Chem Soc* **2024**, http://dx.doi.org/10.1021/jacs.3c11407.

(208) Chen, C. J.; Weil, T. Cyclic polymers: synthesis, characteristics, and emerging applications. *Nanoscale Horiz* **2022**, *7* (10), 1121-1135, http://dx.doi.org/10.1039/d2nh00242f.

(209) Golder, M. R.; Jasti, R. Syntheses of the Smallest Carbon Nanohoops and the Emergence of Unique Physical Phenomena. *Accounts Chem Res* **2015**, *48* (3), 557-566, http://dx.doi.org/10.1021/ar5004253.

(210) Jasti, R.; Bhattacharjee, J.; Neaton, J. B.; Bertozzi, C. R. Synthesis, Characterization, and Theory of [9]-, [12]-, and [18]Cycloparaphenylene: Carbon Nanohoop Structures. *J Am Chem Soc* **2008**, *130* (52), 17646-+, http://dx.doi.org/10.1021/ja807126u.

(211) Li, Y.; Kono, H.; Maekawa, T.; Segawa, Y.; Yagi, A.; Itami, K. Chemical synthesis of carbon nanorings and nanobelts. *Accounts of Materials Research* **2021**, *2* (8), 681-691, http://dx.doi.org/10.1021/accountsmr.1c00105.

(212) Ishii, Y.; Nakanishi, Y.; Omachi, H.; Matsuura, S.; Matsui, K.; Shinohara, H.; Segawa, Y.; Itami, K. Size-selective synthesis of [9]-[11] and [13]cycloparaphenylenes. *Chem Sci* **2012**, *3* (7), 2340-2345, http://dx.doi.org/10.1039/c2sc20343j.

(213) Lewis, S. E. Cycloparaphenylenes and related nanohoops. *Chem Soc Rev* **2015**, *44* (8), 2221-2304, http://dx.doi.org/10.1039/c4cs00366g.

(214) Wu, D.; Cheng, W.; Ban, X. T.; Xia, J. L. Cycloparaphenylenes (CPPs): An Overview of Synthesis, Properties, and Potential Applications. *Asian J Org Chem* **2018**, *7* (11), 2161-2181, http://dx.doi.org/10.1002/ajoc.201800397.

(215) Hermann, M.; Wassy, D.; Esser, B. Conjugated nanohoops incorporating donor, acceptor, hetero - or polycyclic aromatics. *Angewandte Chemie International Edition* **2021**, *60* (29), 15743-15766, http://dx.doi.org/10.1002/anie.202007024.

(216) Lovell, T. C.; Garrison, Z. R.; Jasti, R. Synthesis, Characterization, and Computational Investigation of Bright Orange-Emitting Benzothiadiazole [10]Cycloparaphenylene. *Angewandte Chemie International Edition* **2020**, *59* (34), 14363-14367, http://dx.doi.org/10.1002/anie.202006350.

(217) Okada, K.; Yagi, A.; Segawa, Y.; Itami, K. Synthesis and properties of [8]-, [10]-, [12]-, and [16] cyclo-1,4-naphthylenes. *Chem Sci* **2017**, *8* (1), 661-667, http://dx.doi.org/10.1039/c6sc04048a.

(218) Yagi, A.; Venkataramana, G.; Segawa, Y.; Itami, K. Synthesis and properties of cycloparaphenylene-2,7-pyrenylene: a pyrene-containing carbon nanoring. *Chem Commun* **2014**, *50* (8), 957-959, http://dx.doi.org/10.1039/c3cc48198k.

(219) Qiu, Z. L.; Tang, C.; Wang, X. R.; Ju, Y. Y.; Chu, K. S.; Deng, Z. Y.; Hou, H.; Liu, Y. M.; Tan, Y. Z. Tetra-benzothiadiazole-based [12]Cycloparaphenylene with Bright Emission and Its Supramolecular Assembly. *Angewandte Chemie International Edition* **2020**, *59* (47), 20868-20872, http://dx.doi.org/10.1002/anie.202008505.

(220) Piquero-Zulaica, I.; Garcia-Lekue, A.; Colazzo, L.; Krug, C. K.; Mohammed, M. S. G.; Abd El-Fattah, Z. M.; Gottfried, J. M.; de Oteyza, D. G.; Ortega, J. E.; Lobo-Checa, J. Electronic Structure Tunability by Periodic meta-Ligand Spacing in One-Dimensional Organic Semiconductors. *Acs Nano* **2018**, *12* (10), 10537-10544, http://dx.doi.org/10.1021/acsnano.8b06536.

(221) Taber, B. N.; Gervasi, C. F.; Mills, J. M.; Kislitsyn, D. A.; Darzi, E. R.; Crowley, W. G.; Jasti, R.; Nazin, G. V. Quantum Confinement of Surface Electrons by Molecular Nanohoop Corrals. *J Phys Chem Lett* **2016**, *7* (16), 3073-3077, http://dx.doi.org/10.1021/acs.jpclett.6b01279.

(222) Li, H.; Zhang, Y. F.; Zhang, X. B.; Farrukh, A.; Zhang, Y.; Zhang, Y.; Dong, Z. C. Probing the deformation of [12]cycloparaphenylene molecular nanohoops adsorbed on metal surfaces by tip-enhanced Raman spectroscopy. *J Chem Phys* **2020**, *153* (24), http://dx.doi.org/10.1063/5.0033383.

(223) Gao, Y.; Albrecht, F.; Rončević, I.; Ettedgui, I.; Kumar, P.; Scriven, L.; Christensen, K.; Mishra, S.; Righetti, L.; Rossmannek, M. On-Surface Synthesis of a Doubly Anti-Aromatic Carbon Allotrope: Cyclo [16] carbon. **2023**, http://dx.doi.org/10.26434/chemrxiv-2023-w124b.

(224) Pavlicek, N.; Mistry, A.; Majzik, Z.; Moll, N.; Meyer, G.; Fox, D. J.; Gross, L. Synthesis and characterization of triangulene. *Nat Nanotechnol* **2017**, *12* (4), 308-311, http://dx.doi.org/10.1038/Nnano.2016.305.

(225) Fan, Q. T.; Yan, L. H.; Tripp, M. W.; Krejci, O.; Dimosthenous, S.; Kachel, S. R.; Chen, M. Y.; Foster, A. S.; Koert, U.; Liljeroth, P.; et al. Biphenylene network: A nonbenzenoid carbon allotrope. *Science* **2021**, *372* (6544), 852-+, http://dx.doi.org/10.1126/science.abg4509.

(226) Sun, K. W.; Silveira, O. J.; Ma, Y. J.; Hasegawa, Y.; Matsumoto, M.; Kera, S.; Krejci, O.; Foster, A. S.; Kawai, S. On-surface synthesis of disilabenzene-bridged covalent organic frameworks. *Nat Chem* **2023**, *15* (1), 136-+, http://dx.doi.org/10.1038/s41557-022-01071-3.

(227) Xiang, F. F.; Maisel, S.; Beniwal, S.; Akhmetov, V.; Ruppenstein, C.; Devarajulu, M.; Dorr, A.; Papaianina, O.; Gorling, A.; Amsharov, K. Y.; et al. Planar pi-extended

cycloparaphenylenes featuring an all-armchair edge topology. *Nat Chem* **2022**, *14* (8), 871-+, http://dx.doi.org/10.1038/s41557-022-00968-3.

Acknowledgment

I would like to express my heartfelt gratitude to everyone who contributed to this work in one way or another.

First of all, I would like to thank my supervisor Prof. Johannes Barth for providing me with the invaluable opportunity to study at E20. His support and guidance have been instrumental in my academic journey, and I am truly grateful for his mentorship and continuous support. I would like to thank Dr. Joachim Reichert and Dr. Anthoula C. Papageorgiou who supervised me in the VT-STM lab, and gave valuable guidance and meaningful discussion on the projects.

A big thank you goes out to my lab colleagues: Dr. Wei Ran, who patiently taught me how to use VT-STM when I first joined our group; Dr. Peter Knecht for his assistance with VT-STM images scanning; Dr. Nan Cao for teaching me through XPS techniques; Dennis Meier for his continuous support during my slots in the VT-STM and XPS lab; especially Dr. Biao Yang for his guidance and instruction on using JT-STM and nc-STM, and for his many helpful discussions and assistance in the lab.

I also would like to thank Karl Eberle and Reinhold Schneider for technical support and repairing and maintaining a lot of lab equipment, especially thank Karl Eberle for his assistance when I worked in the ESCA lab. Many thanks to Dr. Knud Seufert for his help in computer and software and thank Prof. Peter Feulner for his assistance in repairing metal (Ho) evaporator.

I especially want to thank our secretary Viktoria Blaschek for her help and support in many aspects during my time in E20 and thank you to all the other E20 members for the easygoing communication and the pleasant memories of whether lunchtime or parties. Your friendly interactions and positive energy have made our time together enjoyable and memorable.

Special thanks goes to Prof. Shobhana Narasimhan, Dr. Abhishek Kumar Adak, and Ritam Chakraborty who have not only provided all theoretical calculations but also greatly contributed to the understanding of the results.

Moreover, I am very grateful to our lunch group, Wei Ran, Nan Cao, Yang Bao, Biao Yang, Wenchao Zhao, Shengming Zhang, Zhongliu Liu, Kongchao Shen, Longfeng Huang and Pengfei Zhao. I want to thank my friends who I met in Munich like Kang Wang, Jianpeng Chen, Yu Fan and so on. Thank you for your company during my stay in Munich.

Last but not least, I am deeply grateful to my family for supporting and understanding me throughout my study.